UNIVERSITATEA DE MEDICINĂ ŞI FARMACIE “IULIU HAŢIEGANU”CLUJ-NAPOCA

ŞCOALA DOCTORALĂ

CLUJ-NAPOCA 2021

DOCTORAL THESIS

The development of sensitive and selective electrochemical methods for the detection of antibiotics

PhD student **Adrian - Marian Blidar**

PhD supervisors **Prof. Dr. Cecilia Cristea**
Prof. Dr. Karolien De Wael

Universiteit
Antwerpen

UMF
UNIVERSITATEA DE
MEDICINĂ ŞI FARMACIE
IULIU HAŢIEGANU
CLUJ-NAPOCA

Acknowledgements

I would like to express my profound appreciation to Professor Cecilia Cristea and Professor Karolien De Wael, my PhD supervisors, for their support not only with the research work but also with the additional problems that came along with my PhD studies, administrative matters and demoralization. I owe them special thanks for offering me the opportunity to make part of their prestigious research teams. Also, perhaps more important, they offered me two models of accomplished, hard-working and ambitious persons, that truly love what they are doing.

A special mention goes to Dr. Bogdan Feier, the person with whom I started working in research and with whom I also had carried out most of my work. He has been very patient and always tried to educate me and give me advices, both for my professional and personal life.

Another two special mentions go to Dr. Mihaela Tertiș and Dr. Stanislav Trashin, two excellent researchers, armed with vast knowledge and patience that had helped me tremendously in my work. They were always there to answer my questions, regardless of how pointless they were.

I would like to thank the research group from Cluj for their feedback, cooperation and of course friendship. I am grateful to all, both the more experienced members: Dr. Oana Hosu, Dr. Ioan Neaga, Dr. Anca Florea, Dr. Bogdan Iacob, Dr. Andreea Cernat, Prof. Dr. Robert Săndulescu, Prof. Dr. Ede Bodoki, Prof. Dr. Radu Oprean, and to the younger collegues: Adrian, Laura, George, Iulia, Ana-Maria. Similarly, I would like to thank to all the members from the AXES group, from Antwerp, for all their help and support during my research stays.

As experimental work requiers funding, I am greatful for all the financial support I benefit during my PhD: the scholarships from UMPh, Erasmus, PCD and POCU, the BOF scholarship from University of Antwerp and the support from the Plasmon Electrolight project.

LIST OF PUBLICATIONS

Published articles in extenso as a result of the PhD thesis

Published as first author

1. **A. Blidar**, B. Feier, M. Tertis, R. Galatus, and C. Cristea, “Electrochemical surface plasmon resonance (EC-SPR) aptasensor for ampicillin detection,” Anal. Bioanal. Chem., vol. 411, no. 5, 2019, doi: 10.1007/s00216-018-1533-5. ISI, IF=3.637 **(*State of the art* - Chapter II)**;
2. **A. Blidar***, B. Feier*, A. Pusta, A.-M. Drăgan, and C. Cristea, “Graphene–Gold Nanostructures Hybrid Composites Screen-Printed Electrode for the Sensitive Electrochemical Detection of Vancomycin,” Coatings, vol. 9, no. 10, p. 652, 2019, doi: 10.3390/coatings9100652; ISI, IF=2.436 **(*Personal contributions* - Chapter I)**;
3. **A. Blidar**, S. Trashin, E. N. Carrión, S. M. Gorun, C. Cristea, and K. De Wael, “Enhanced Photoelectrochemical Detection of an Analyte Triggered by Its Concentration by a Singlet Oxygen-Generating Fluoro Photosensitizer,” ACS Sensors, 2020, doi: 10.1021/acssensors.0c01609; ISI, IF=7.711 **(*Personal contributions* - Chapter III)**;
4. **A. Blidar***, O. Hosu*, B. Feier, G. Ștefan, D. Bogdan, C. Cristea, “Gold-based nanostructured platforms for oxytetracycline detection from food and wastewaters by a ”signal-on” aptasensing approach” Food Chemistry, 2021, doi: 10.1016/j.foodchem.2021.131127, ISI, IF= 7.514 **(*Personal contributions* - Chapter II)**;

*Published as co-author with equal contributions**

5. B. Feier*, **A. Blidar***, A. Pusta, P. Carciuc, and C. Cristea, “Electrochemical sensor based on molecularly imprinted polymer for the detection of cefalexin,” Biosensors, vol. 9, no. 1, 2019, doi: 10.3390/bios9010031; ISI, IF=3.240 **(*Personal contributions* - Chapter II)**;
6. B. Feier*, **A. Blidar***, L. Vlase, and C. Cristea, “The complex fingerprint of vancomycin using electrochemical methods and mass spectrometry,” Electrochem. Commun., vol. 104, no. June, p. 106474, 2019, doi: 10.1016/j.elecom.2019.05.023; ISI, IF=4.333 **(*Personal contributions* - Chapter I)**;

TABLE OF CONTENTS

PERSONAL CONTRIBUTION

ABBREVIATIONS

AA	Ascorbic acid
AFM	Atomic force microscopy
AgNPs	Silver nanoparticles
AMP	Ampicillin
AMX	Amoxicillin
APAP	Acetaminophen
APT	Aptamer
AuE	Gold electrode
Au-SPE	Gold-based screen-printed electrode
AuNPs	Gold nanoparticles
AuNPs-SPE	Carbon-based modified with gold nanoparticles screen-printed electrode (commercial)
AuNSs	Gold nanostructures
AuNSs-C-SPE	Carbon-based modified with gold nanostructures screen-printed electrode
AuNSs-G-SPE	Carbon-based modified with graphene and gold nanostructures screen-printed electrode
BSA	Bovine serum albumine
CA	Chronoamperometry
CFX	Cefalexin
CFD	Cefadroxil
CFC	Cefaclor
CFOX	Cefuroxime
CFTX	Cefotaxime
CFTXO	Ceftriaxone
CFTZ	Ceftazidime
CNF-SPE	Carbon-based modified with carbon nanofibers screen-printed electrode
CNT	Carbon nanotubes
CNT-SPE	Carbon nanotube modified screen-printed electrode
CP	Chronopotentiometry

C-SPE	Carbon-based screen-printed electrode
C-SPE$\vert$F$_{64}$PcZn$\cup$TiO$_2$	Carbon-based screen-printed electrode modified with perfluoroisopropyl-substituted zinc phthalocyanine deposited on TiO$_2$
CTH	Catechol
CV	Cyclic voltammetry
DNA	Deoxyribonucleic acid
DPV	Differential pulse voltammetry
DXC	Doxycycline
EIS	Electrochemical impedance spectroscopy
ELISA	Enzyme-linked immunosorbent assay
F$_{64}$PcZn	Perfluoroisopropyl-substituted zinc phthalocyanine
F$_{64}$PcZn$\cup$TiO$_2$	Perfluoroisopropyl-substituted zinc phthalocyanine deposited on TiO$_2$
GCE	Glassy carbon electrode
GEN	Gentamicin
GO	Graphene oxide
GOX	Glucose oxidase
G-SPE	Carbon-based modified with graphene screen-printed electrode
HPLC	High performance liquid chromatography
HRP	horseradish peroxidase
HQ	Hydroquinone
I3AA	Indole-3-acetic acid
ITOE	Indium tin oxide electrode
K$_D$	Dissociation constant
LOD	Limit of detection
LOQ	Limit of quantification
LDR	Linear dynamic range
MIP	Molecularly imprinted polymer
MPA	Multipulse amperometry
MRSA	Methicillin-resistant *Staphylococcus aureus*
MS	Mass spectrometry
MWCNT	Multi-walled carbon nanotubes
NIP	Non-molecularly imprinted polymer
OXA	Oxacillin
OXT	Oxytetracycline
PBS	Phosphate buffer saline solution
PCR	Polymerase chain reaction
PEN V	Penicillin V
PEN G	Penicillin G

PtE	Platinum electrode
Pt-SPE	Platinum-based screen-printed electrode
RIF	Rifampicin
RIF-Q	Rifampicin quinone
RNA	Ribonucleic acid
RP-HPLC	Reverse phase high performance liquid chromatography
RSD	Relative standard deviation
RT-PCR	Reverse transcription polymerase chain reaction
SELEX	Systematic Evolution of Ligands by EXponential Enrichment
SEM	Scanning electron microscopy
SPE	Screen-printed electrode
SPR	Surface plasmon resonance
SWCNT	Single-walled carbon nanotubes
SWV	Square wave voltammetry
UHPLC	Ultra high performance liquid chromatography
UV-Vis	Ultraviolet – Visible
VAN	Vancomycin
XPS	X-ray photoelectron spectroscopy

INTRODUCTION

The discovery of antibiotics represented one of the greatest breakthroughs in medicine. Their introduction offered a viable option for the treatment of bacterial infections. Based on the discovery of numerous families of antibiotics, with several successful molecules, their use saw an accelerated expansion. This success combined with an increasing intensive use is apparently bound to be also their undoing.

This is due to the development of acquired antibiotic resistance, something that, although predicted from the beginning, developed sooner and with greater consequences as expected. Antibiotic resistance, which represents the acquirement by the bacteria of resistance to the action of one or several antibiotics, can lead to inefficient antibiotherapy, greater difficulties in the treatment of relative less harmful infections and even to the impossibility of treatment and death.

The antibiotic resistance is also correlated with a lack of newly discovered antibiotics, capable to substitute the molecules against which the pathogens developed resistance. This is partially due to the focus of drug discovery to other therapeutic classes, with a larger applicability.

The development and spread of antibiotic resistance are fueled by the widespread presence of trace levels of antibiotics residue, in various media, from environment to aliments. The issue is with the concentration of antibiotics present in these media. The low and very low concentration of antibiotics in these media are affecting only the part of the bacteria population without resistance, acting like a selective factor, and further helping in the evolution and growth of antibiotic-resistant bacteria. Similarly, these problems can be found regarding the levels of antibiotics during antibiotherapy. Here, the question is about the value of the concentrations of antibiotics in biological fluids, typically blood. On one hand, subtherapeutic concentrations, those too low for an efficient treatment can only lead to antibiotic resistance, similar to the antibiotics traces in the environment. On the other hand, concentrations too high can lead to an increase in the incidence of adverse effects. These problems are related to the concept of therapeutic drug monitoring which consists in the precise measurement of antimicrobial agents in the blood of patients, undergoing therapy, in order to proper establish the individual pharmacokinetics for each individual patient. By employing therapeutic drug monitoring, it can be verified that the minimum inhibitory concentration coresponding to a certain antibiotic-bacteria is achieved, minimizing the risc of antibiotic resistance. Also, through the use of therapeutic drug monitoring, toxic concentrations of antibiotics can be avoided.

It can be observed that a major contributing factor in the problem of antibiotic resistance is the almost ubiquitous presence of antibiotics in the surrounding media in often unknown or even dangerous concentrations. A solution to this is the rigorous monitoring of the levels of antibiotics, which in term requires an almost constant development of new, more sensitive, more selective and more accessible analytical methods. There is especially a strong need of screening methods, with relatively simple instrumentation, capable of decentralized analysis. In this direction, electrochemical methods represent a very viable alternative.

The electrochemical detection of antibiotics is a subject of great interest, the electrochemical methods being less used for the quantification of antibiotics. Additionally, the fields of electroanalysis and of biosensoristics have also gained a continuously increasing interest in recent years, due to the introduction of new, innovative strategies and due to an increase in the miniaturization of the instrumentation required.

In this context, the main objective of this doctoral research was the development of various electrochemical methods for the detection of antibiotics, from a wide variety of matrices, using different strategies.

The use of biomimetic elements, like molecularly imprinted polymers and aptamers, allows for an easy and versatile functionalization of the electrodes, resulting in a new direction in the development of electrochemical sensors for antibiotics. These strategies are aimed more at indirect detection, but there are also new emerging approaches for direct detection, like electrochemical fingerprinting. Electrochemical fingerprinting allows the identification of the specific, characteristic electrochemical signal of a certain molecule, in specific conditions. Another recent, innovative strategy is the use of photosensitizers, compounds capable of generating singlet oxygen that oxidizes specifically phenolic compounds, coupled with the electrochemical detection of the resulting products.

All the approaches mentioned above were tested and employed, throughout the work presented in this thesis, for the development of new electrochemical strategies for the detection of several antibiotics, belonging to different antibiotic groups. In this endeavor, new protocols were optimized and used, and new electroanalytical platforms were obtained through the modification of electrodes with various nanomaterials and biomimetic elements.

The work resulted in the creation of several sensitive and selective electrochemical methods which were successfully applied for the detection of antibiotics in various matrices, like environmental samples, pharmaceutical formulations, and biological fluids.

STATE OF THE ART

Chapter I. Antibiotics and antibiotics resistance

1.1. Antibiotics

The discovery and introduction of antibiotics was probably one of the greatest breakthroughs in medicine of the 20th century. In addition to treating infectious diseases, antibiotics made many modern medical procedures possible, including cancer treatment, organ transplants and open-heart surgery[1].

An antibiotic is a substance that can inhibit or to kill microorganisms. More specifically is an antibacterial drug that is used to treat or prevent infections by terminating or inhibiting the growth of bacteria in or on the body of the patient[1].

There are several ways of classifying the numerous antibiotics discovered, the most common classification being based on their molecular structures. The most commonly used classes include β-lactams, with two subclasses, penicillins and cephalosporins, macrolides, tetracyclines, quinolones, aminoglycosides, glycopeptides and rifamycins[1,2].

Antibiotics can be also classified based on their mechanism of action: (i) inhibition of cell wall synthesis (β-lactams, glycopeptides), (ii) inhibition of protein synthesis (macrolides, tetracyclines, aminoglycosides), (iii) inhibition of nucleic acid synthesis (quinolones, rifamycins) and antimetabolite activity (sulfonamides).

Another separation can be made in bactericidal antibiotics, that kills bacteria, like β-lactams, aminoglycosides, and quinolones or bacteriostatic antibiotics, that only prevents bacterial growth and reproduction, like macrolides and tetracyclines[3].

The work presented in this thesis focused mainly on the detection of four compounds, each one from a different class: vancomycin (VAN) from glycopeptides class, cefalexin (CFX) from cephalosporins class, oxytetracycline (OXT) from tetracyclines class, and rifampicin (RIF) (**Fig. 1**).

Although there is a close structural similarity within one class, from the above mentioned, the overall antibiotics group is rather heterogeneous, the main attribute of the group being a pharmacological effect, not a chemical property. This heterogeneity regarding the chemical structures makes their chemical analysis more complex. There is a need of different approaches, depending on the class of antibiotics.

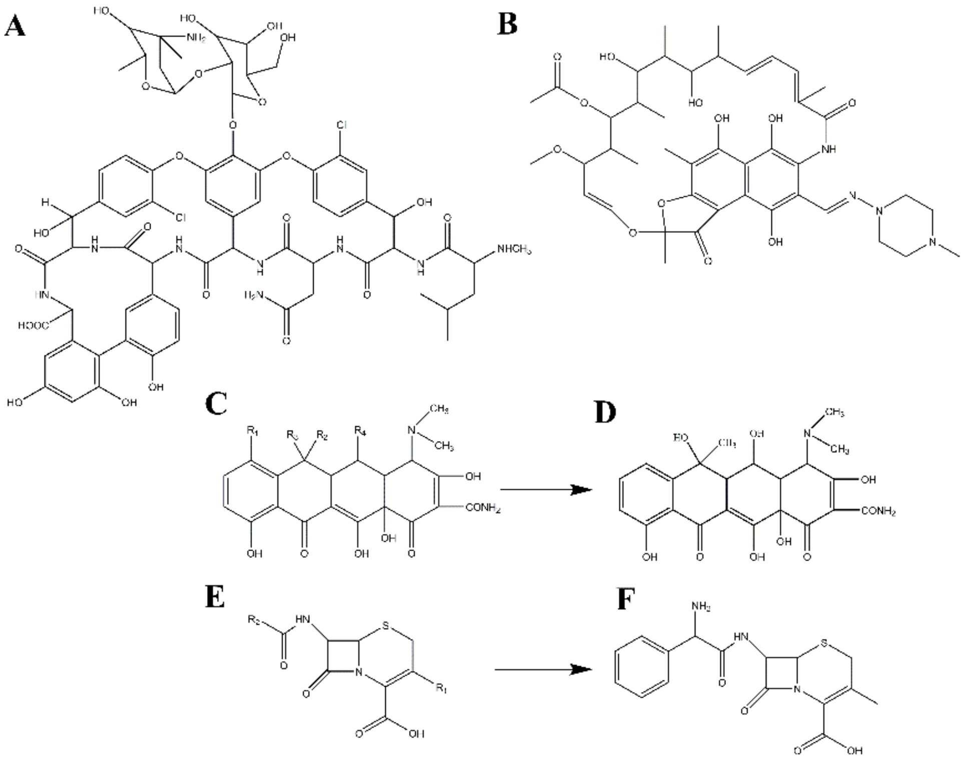

Fig. 1. The structures of the investigated antibiotics: (**A**) Vancomycin, (**B**) Rifampicin, (**C**) Tetracyclines general structure, (**D**) Oxytetracycline, (**E**) Cephalosphorins general structure and (**F**) Cefalexin.

As stated, the discovery of antibiotics meant a very important leap for the entire world, with various and profound consequences, but this leap also brought to attention a new problem, which appeared and grew in intensity due to the decades of intensive use of antibiotics. This problem is the development of antibiotics resistance[1,2].

1.2. Antibiotics resistance

Antimicrobial resistance is the ability of a microorganism (e.g., a bacterium, virus, or parasite) to resist the action of an antimicrobial agent. It is an adaptation of the microorganism to the environment[4]. Any use of an antimicrobial substance forces microorganisms to adapt or die. Antimicrobial resistance reduces or loses the effectiveness of the antimicrobial agent in curing or preventing infection caused by this microorganism[4,5].

The bacterial resistance to antibiotics is the ability of bacteria to resist the action of an antibiotic. Some bacteria are naturally resistant to certain antibiotics (intrinsic or innate resistance). An even more worrying problem occurs when some bacteria, normally sensitive to antibiotics, become resistant as a result of adaptation through genetic modification (acquired resistance). Genes encoding antibiotic resistance in one species of bacteria can be easily spread to other species of bacteria through an exchange of genetic material.

In the ongoing fight for "green space", all resistant bacteria are selected because the antibiotic eliminates the bacteria that are still sensitive around them. All resistant bacteria survive in the presence of antibiotics and continue to grow and multiply[5].

Infections caused by antibiotic-resistant bacteria may require more care and more expensive alternative antibiotics that can cause more serious side effects. Once installed in one person, antibiotic-resistant bacteria can spread to another person, and high antibiotic use in a population (hospital or community) strongly promotes such a spread.

Resistance to several antibiotics is the resistance of bacteria to several antimicrobial drugs. The challenge for multi-drug resistant bacteria lies in the limited number of options left (if any) for the treatment of patients infected with these micro-organisms.

Examples of bacteria usually resistant to several antibiotics are methicillin-resistant *Staphylococcus aureus* (MRSA), vancomycin-resistant enterococci (VRE), broad-spectrum β-lactamase-producing enterobacteria and *Pseudomonas aeruginosa*[5].

The two major factors governing antimicrobial resistance are:

- the intensive use of antibiotics, which exerts an ecological pressure on microorganisms and contributes to the emergence and selection of antimicrobial-resistant microorganisms in populations;
- spread and cross-transmission of antimicrobial-resistant microorganisms between humans, between animals and between humans and animals and the environment[5].

Antibiotics used to treat and prevent infections in animals belong to the same chemical groups as those used in human medicine, therefore animals can transfer antibiotic-resistant bacteria to humans through food or through direct human-animal contact. In addition to their therapeutic value, the discovery in 1950 of their ability to improve growth and feed efficiency in food animals led also to their widespread use as feed supplements[6].

Healthcare associated infections infections and antimicrobial resistance, including antibiotic resistance, are two special health problems with great implications in EU and the entire world[5]. according to Cassini *et al.*[7], a number of 671689 infections with antibiotic-resistant bacteria, were reported for European Union (EU) and European Economic Area (EEA) in one year, 2015. From these, 63,5% (426277 of 671689) were associated with health care. These infections accounted for an estimated 33110 attributable deaths and 874541 disability-adjusted life-years[7].

The problem of antibiotic resistance is even more worrying because there are a very small number of compounds in the research and development phase that would be potentially active against these bacteria and could be placed on the market in the next 5-10 years[2,8]. There is a general lack of investment and activity in the field of antibiotic drug discovery and consequently few new drugs are on the horizon.

World Health Organization (WHO) also has proposed a global action plan on this topic, recommending several strategies. These strategies include the raise of awareness regarding antibiotic resistace and an urgent increase in the surveillance of the use of antibiotics. Another important action, mentioned in the fight against antibiotic resistance, is the development of new, rapid, and more accessible detection methods for the determination of antibiotics from different and complex matrices[9–11].

Chapter II. Analytical methods for antibiotics detection

The problem of antibiotic resistance is facilitated by the increasing presence of antibiotics in the environment and food. The presence of antibiotics at concentrations as low as nanograms per milliliter has been shown to promote the development of resistance in the laboratory[12–16].

Due to the fact that low levels of antibiotics in soil and water can help in the selection and multiplication of antibiotic-resistant microorganisms, antibiotics are now regarded as a significant environmental pollutant[17–19]. However, the effect of antibiotic pollutants in the environment has not been yet sufficiently characterized[20].

There are no global models able to track and predict the distribution of antibiotic pollutants and their effects worldwide. A possible cause for this is that, in the most existing antibiotic distribution studies, the samples are obtained and taken to laboratories for analysis in a costly and time-consuming pipeline[8,21–24]. While localized studies are clearly valuable, tackling the problem of antibiotics in the environment is a global problem that needs a wider approach[25,26] .

In this context, there is a clear need for fast, economically accessible analytical methods, capable of decentralized, field-ready analysis of antibiotics. The availability of such techniques would increase the convenience of on-site measurement, meaning that samples may be taken and analyzed more frequently. In other terms, this would lead to more data and to the construction of better predictive models of antibiotic pollutant entry and persistence in local environments and the rise of antibiotic resistance[16,27].

On-site measurement will allow for the proper assessment of the correlation between the levels of antibiotic pollutants in a certain area and the development of antibiotic resistance, where antibiotic pollution has been shown to be correlated with antibiotic resistance development[28,29].

Another important source for the progress of antibiotic resistance is the intensive use of antibiotics in agriculture and animal husbandry and their subsequently presence in the alimentation of the general population. Although, the analysis of aliments can be somewhat easier to carry out, even in centralized manner there is still the problem of the determination of antibiotics in low concentrations.

An ideal method for the detection of antibiotic residues in food would be fast, efficient, and inexpensive while also able to identify a wide range of antibiotics.

Unfortunately, there is no such method yet for antibiotic analysis. The liquid chromatography (LC) techniques, coupled with mass spectrometry (MS) detection are one of the most sensitive and selective methods, but they are expensive, require complex instruments and are not suitable for decentralized analysis. This means that LC-MS techniques are a viable solution regarding a second level of antibiotic analysis, the one composed of confirmatory methods, but there is still a deficiency in regard to the first level, represented by the screening techniques.

In this context, several types of methods for the detection of antibiotics can be identified. The most important are the microbiological assay, the immunoassays, LC methods, biosensors, and electrochemical approaches.

2.1. Microbiological assays

A classic strategy, implemented since the 1950s[30] is the use of microbiological assays that employ antibiotic-sensitive species of bacteria to determine whether specific antibiotics are present in a given sample based on changes in the known growth patterns[30].

Current commercially available assays rely on one of two techniques to identify antibiotic presence in a sample. Disc diffusion uses discs coated in the sample of interest that are placed on plates on which bacteria are grown; the presence of a halo of cleared growth around the disc indicates that the bacteria were terminated by an antibiotic in the disc. This test can identify specific antibiotics or classes of antibiotics depending on the species of bacteria used[31,32].

A second technique uses bacteria that have been engineered to yield a colorimetric output that can be quantitatively analyzed with spectrophotometry to determine the concentration of antibiotic. The disadvantages of this strategy are the requirement of sterile procedure and laboratory facilities to co-incubate the sample with bacteria[33,34]. These color-change reactions can be quantitatively analyzed with spectrophotometry to determine the concentration of antibiotic as low as 1 $ng \cdot mL^{-1}$, present in the sample[33,34]. These methods can function in complex matrices, but due to their output, determining precise concentrations would be difficult to ascertain. Many microbiological assays are focused exclusively on the β-lactam family of antibiotics and have poor sensitivity outside this category. A review of commercial tests found that while they can detect concentrations as low as 4 $ng \cdot mL^{-1}$ within the β-lactam family, the tests are limited to 100 $ng \cdot mL^{-1}$ or more in the case of other antibiotic classes[35].

The use of microfluidics and paper-based techniques has mitigated the requirement for laboratory facilities for some microbiological assays. A challenge for field use of paper-based microbial assays is the requirement for live or lyophilized bacteria that can be reconstituted on-site without introducing contamination[36,37]. Considering everything mentioned above, microbiological assays are not yet optimal for on-site field testing.

2.2. Immunoassays

Immunoassays rely on specificity of interactions between antibodies and the molecule of interest[38]. They typically have colorimetric output[22,39,40], with some presenting fluorescent or chemiluminescent readouts[41].

Immunoassays, specifically enzyme-linked immunosorbent assay (ELISA), have been adapted for antibiotic detection in soil, food, and water samples[22,39–42]. In addition, commercially available ELISA kits created for food samples analysis have also been utilized for monitoring antibiotic presence in rivers and soil samples[22,39]. Due to the cross-reactivity of antibodies detecting isomers and degradation products, ELISA may overestimate the concentrations and fail to show the decline of antibiotics levels over time[39]. Immunoassays can provide sensitive detection of antibiotics in samples adding secondary antibodies to amplify the signal, but this increases the cost per sample, limiting the utility of immunoassays as a field-ready technique[40]. Another drawback for the use of immunoassays for on-site analysis is their reliance on spectrophotometers for quantitative measurements[40].

The use of antibodies generally restricts one immunoassay to a single or relatively few antibiotics depending on the specificity of antibodies used in the assay[22]. Crossreactivity of antibodies lessens the specificity of the test, as antibodies may react with non-biologically active components of antibiotic degradation pathways[39].

Despite these limitations, recent developments of miniaturized, user-friendly immunoassays offer some potential for the adaptation of this technique for the field analysis. The enhancement of the efficiency and of the throughput was achieved by implementing a multiplex format, which localizes different antibodies to distinct parts of a chip or strip. These multiplexed immunoassays, which have been specifically designed with on-site, high-throughput detection in mind, show promise for first-line use in the field[43–46].

2.3. Liquid Chromatography methods

LC, including its enhanced variants, like high performance liquid chromatography (HPLC) or ultra high performance liquid chromatography (UHPLC) have been used extensively for pharmaceuticals analysis, including antibiotics[6]. LC methods techniques can be coupled with various detectors for antibiotic analysis. Spectrophotometric, UV-Vis detection is often used, being one of the less complex and less expensive alternatives[6]. The resulting LC-UV-Vis approach can be found implemented in a plethora of studies, for the analysis of one antibiotic to several, by simultaneous detection[6,47,48]. Also, the LC-UV-Vis methods are the most mentioned in the monographies of antibiotics in European Pharmacopeeia[49–51]. The use of MS for detection with LC results in some of the most sensitive and selective techniques[6,47,48]. They also can discern between the analyte and its various possible degradation products. Although very sensitive and selective, the LC approach, can be used only for centralized analysis and are considered confirmatory methods[6,47,48], being the official standard mentioned in regulations[6,51].

Nevertheless, LC–MS strategies require extensive compound-dependent parameter optimization, which means that they are targeted assays and are not suitable to screen untargeted antibiotics. Based on the analytical needs of unknown antibiotics remaining in food, high-resolution MS analyzers, such as time-of-flight (TOF), quadrupole time-of-flight (QTOF), and Orbitrap, have been introduced into the environmental analysis field for purposes of non-target screening and unknown identification schemes, which can be run independently or combined with target analysis instruments. MS technologies, including both targeted analysis (such as LC–MS) and non-targeted analysis (such as TOF and Orbitrap), contribute greatly to promote the analysis of antibiotic residues in foods[6].

2.4. Electrochemical methods

In the recent decades, electrochemical methods have shown enormous potential towards the detection of antibiotic residues due to their advantages, such as excellent sensitivity, rapid analysis, and possibility of miniaturization[52,53]. To date, the most frequent technique used for the electrochemical detection of antibiotics is voltammetry with all its types: cyclic voltammetry (CV), differential pulse voltammetry (DPV), square wave voltammetry (SWV), and stripping voltammetry (SV). In general, voltammetric sensors have been attracted attention due to their improved performance in electroanalysis. Additionally, amplification of mass-transport, simple measurement and preparation, the possibility of miniaturization, and automation are the well-known advantages of voltammetric techniques. The fast response, selectivity, low detection limits, and wide linear range are additional advantages of such sensors[54,55].

The simplest way in which voltammetric methods can be used is in the direct detection of antibiotics, based on the current resulted from the direct electrooxidation or electroreduction of the antibiotic molecules, but this approach has some drawbacks, like limited selectivity and the lack of an electrochemical response for certain antibiotics[56,57]. These limitations can be overcome using an indirect approach, which generally registers the current caused by the electrotransformation of a mediator, a redox probe, rather than that of the antibiotic itself. This approach is a lot more developed, with numerous possibilities, being widely used in the development of electrochemical biosensors. In this case, the specific interaction between a recognition element, usually found immobilized onto the surface if the working electrode, and the analyte is correlated with an electrochemical signal[53,54]. As stated, the indirect approach generally means the creation of a biosensor, which can be of many types, representing an entire field and thus are treated separately.

2.5. Biosensors

A biosensor converts a biological or chemical reaction into a measurable and quantifiable signal which is proportional to at least one analyte of this reaction.

The biological or chemical event which leads to the generation of the signal, occurs at the level of an interfacial architecture, called a transducer –electrode surface, optic fiber, surface plasmon resonance (SPR) chip, on which a biorecognition entity is immobilized (**Fig. 2**). The mentioned reaction, represents the interaction of the biorecognition entity, also called bioreceptor, with the analyte, and leads to the generation of a signal in the form of pH change, heat, charge, light or mass change, etc[58–60].

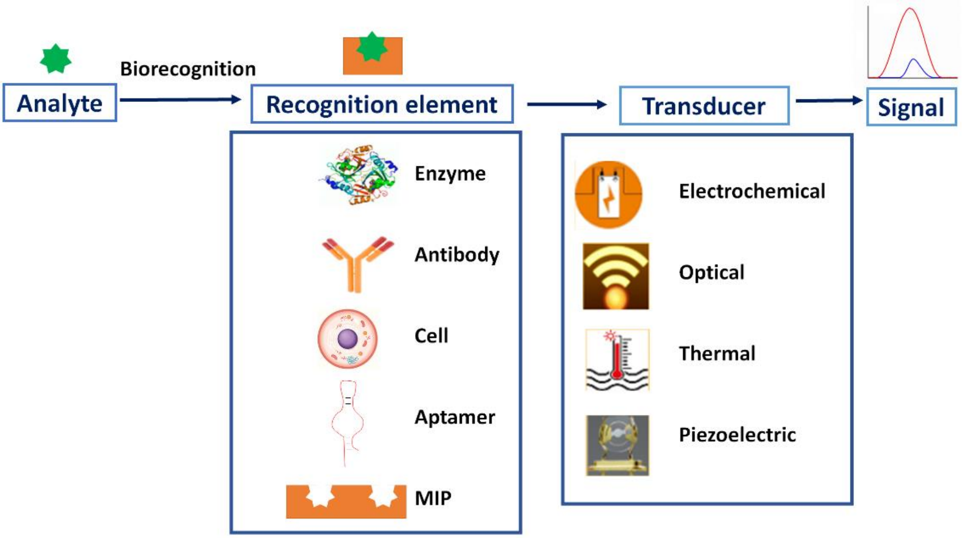

Fig. 2. Schematic representation of a biosensor (Adapted from Naresh and Lee[61]).

The biorecognition element is usually a biological element –i.e. enzyme, antibody, deoxyribonucleic acid (DNA), cell–, but it can be also a biomimetic element, like an aptamer (APT) or a molecularly imprinted polymer (MIP), that selectively binds the target molecule which could be found in simple or more complex matrices[58–60].

The function of the transducer is to generate a measurable electrical signal from the products of the biorecognition reaction, the intensity of this signal being directly or inversely proportional to the analyte concentration. This signal is amplified by complex electronic circuitry. The processed signals are then displayed in numeric or graphic form or as an image, depending on the requirements of the end user[58–60].

The signal from the biorecognition reaction that undergoes transduction depends on the nature of the transducer and may be electrochemical (current, potential), optical (absorbance, SPR), piezoelectric (mass) or thermal (temperature) [58–60].

Regarding the detection of antibiotics, biosensors appear to be a very useful analytical tool due to their advantages of high selectivity, rapid detection, and in-situ applications. Recently, there is a growing rise in the fabrication of antibiotic biosensors[54,62–66]. There are numerous studies dedicated to the development of all types of biosensors for the detection of antibiotics[63,64]. Among them, electrochemical biosensors represent one of the most important part, based mainly on their relative high sensitivity and on the more economically accessible equipment required for their development.

Chapter III. Electroanalytical methods and electrochemical sensors for the detection of antibiotics

3.1. Direct detection

In general, electroanalytical methods are based on the direct electrotransformation of the analyte. This is the direct approach and typically does not include the use of bioelements or of specific recognition elements. Properties like current or potential are measured and correlated with the changes resulted due to reduction/oxidation reactions of the analyte[58].

There are numerous studies that focused on the electrochemical behaviour and implicitly the direct electrochemical detection of antibiotics. Methods were developed for antibiotics from several classes, like β-lactams[56,57,67–70], aminoglycosides[71], quinolones[72–80], tetracyclines[81–84], macrolides[85–88], glycopeptides[89,90] and rifamycins[91–94]. Representative work in this direction, was carried out by Feier *et al.*[56,57], who investigated the electrochemical behavior of five pencillins, penicillin V (PEN V), penicillin G (PEN G), ampicillin (AMP), amoxicillin (AMX) and oxacillin (OXA) and of seven cephalosporins, ceftriaxone (CFTXO), cefotaxime (CFTX), ceftazidime (CFTZ), cefadroxil (CFD), cefuroxime (CFOX), cefaclor (CFC), and CFX, on a bare boron-doped diamond electrode (BDDE). Briefly, three penicillins, PEN V, PEN G and OXA, presented irreversible oxidation peaks, but all three at around the same potential (+1.6 V), which made their simultaneous detection very difficult to achieve. However, AMX presented only a shoulder at around +1V and AMP no signal[57]. Besides, the cephalosporins also had one anodic peak, observed for the tested molecules, but the differences in peak potential and peak area were large. The peak potential varied from around +1 V to around +1.6 V and regarding the peak area, CFX had a peak five times larger than CFD[56].

Based on these results, Feier *et al.* developed two distinct DPV-based methods for the quantitative determination of OXA[57] and CFX[56] from pharmaceutical samples, human urine and river water.

3.2. Indirect detection. Electrochemical (bio)sensors

Most of the indirect detection assays rely on the specific biorecognition of the analyte using a recognition element. In general, this single binding event does not result in a detectable signal, the system relying on additional interactions or on a indirectly induced reaction that generates an electrochemical signal correlated to the analyte concentration[95].

Considering that all the presented biosensors use an electrochemical transducer, they are divided in subgroups based on the type of the recognition element used: enzyme, antibody, APT, etc.

3.2.1. Receptor/enzyme-mediated electrochemical biosensors

Enzymes are employed in two roles in the detection of antibiotics. First, when the enzymes act as the direct recognition element, interacting directly with the analyte, resulting in its transformation through an enzymatic reaction. The most representative strategy is the use of penicillinase, which hydrolyzes penicillins, decreasing the local pH. The pH change is then registered amperometrically using a pH-sensitive redox probe[96–98].

A second approach is when enzymes act as labels or mediators in combination with other bioligands. In this case the antibiotic does not interact directly with the enzyme but with another bioelement[99] or with the product of the enzymatic reaction[100]. These interactions influence the concentration of electrochemically detectable enzymatic product, either by influencing the action of the enzyme[99] or by chemically interacting with the product[100]. Enzymes such as horseradish peroxidase (HRP)[100] and glucose oxidase (GOX)[99] are usually used in this approach.

3.2.2. Electrochemical immunosensors

Electrochemical immunosensors rely on the specific antigen-antibody reaction. Based on this, they are related to immunoassay and are also a subgroup of biosensors that use an antibody as a recognition element and generate an electrochemical signal.

Although highly specific, the “antigen-antibody” interactions require additional elements to translate this interaction into an electrochemical signal. Most often this means the use of electrochemical mediators or of redox probes, the signal of which can be correlated to the binding of the analyte by the antibody. Another problem is that the electrochemical immunosensors usually lack desired sensitivity. To address this problem, significant efforts have been directed towards the development and introduction of new electrode modifiers that can improve the functionalization with biomolecules. These modifiers can be carbon nanotubes and graphene[101,102], nanoporous gold[103], polymers (poly-pyrrole-N-hydroxysuccinimide)[104], and magnetic nanomaterials[105]. Apart from these, several enzyme labels[106], and dye molecules[107] have also been used with antigen-antibody complexes to improve the sensitivity of the sensors.

Although quite popular in the past, the electrochemical immunosensors lost popularity, like the enzymatic sensors, with the introduction of biomimetic elements such as APTs and MIPs. These biomimetic elements present several advantages compared to the biological elements, mainly a lower cost, higher stability and a more facile use, especially considering their immobilization on the electrode surface.

3.2.3. Aptamer-based electrochemical biosensors

In recent years, APT-based electrochemical biosensors have emerged as a robust detection approach for antibiotic residues. Compared to antibodies, APTs exhibit improved physicochemical stability and longer shelf life, with reasonable cost, ease of in vitro synthesis, and simple modification procedures[108]. The creation of the aptasensors is conventionally achieved by two main techniques: (i) direct modification of a biofunctionalized sensor surface with APTs using appropriate linkers and (ii) non-covalent modification of functionally activated surfaces with APTs. Nanomaterials (e.g. carbon fibers and gold nanoparticles) are widely used for the electrochemical detection of antibiotics to improve the sensitivity of aptasensors[109,110]. These aptasensors have been further developed by using methylene blue or ferrocene to produce highly sensitive and distinctive signal tags for multiplexed antibiotic detection[111,112].

Once with the increase in interest and use of APTs, it appeared also certain questions and concerns regarding their selectivity. For example, McKeague *et al.*, compared multiple techniques used for the determination of the K_D of APTs and showed how the sensitivity of each technique can affect the value obtained for K_D and implicitly the assumed selectivity of each APT[113].

Further studies highlighted the need to investigate and validate the APT-target interaction using a multifaceted analytical approach before using APT sequences in other studies. In particular, researchers should avoid relying solely on rapid and accesible assays as analytical approaches to validate binding affinity, as the risk of misinterpreting the true performance of a given APT is particularly high. The general conclusion emphasizes the fact that at the moment there is no technique that can be singlely applied for the charactherization of all APTs and therefore a strategy using multiple methods should be implemented[114,115].

3.2.4. Molecular imprinted polymer-based electrochemical biosensors

Molecularly imprinted sensors have gained increasing attention due to the ease in fabrication and relatively high selectivity. The overall fabrication process of MIPs represents mainly the polymerization of crosslinkers and functional monomers with template molecules. Simplified, the fabrication process consists in two main steps. First step is the polymerization of the template with the monomers, resulting in the entrapment of the template inside the polymer, followed, in the second step, by the template extraction, leaving “imprinted” cavities inside the polymer[116].

MIPs are quite simple to make and can be easily tailored to recognize and bind the target molecule[117]. In addition, MIPs have the advantage of high selectivity, low cost, high sensitivity, and robustness. As a result, MIPs have found application in many fields in recent decades, such as liquid chromatography, solid phase extraction, mimetic catalysis, chiral separation, biosensing, binding assay, diagnostic kits, controlled release of drugs, etc[118]. Thus, the properties of MIPs are potentially very suitable for the development of sensors for the detection of various small molecules[119], including antibiotics[120,121].

A wide variety of nanomaterials –including graphene oxide (GO), catalytic Prussian blue polymer, magnetic nanomaterials, metal nanoparticles, and graphene– have been extensively used to enhance the sensitivity of the MIP-based electrochemical sensor for antibiotic residues[116,122–125].

Chapter IV. Specific electrochemical strategies employed in the present work

4.1. Electrochemical fingerprint

There is a large variety of electrochemical detection strategies, the majority of them being also employed for the detection of antibiotics[52,54]. These electroanalytical strategies can be broadly split into indirect or mediated detection[126] and direct detection. Generally, direct detection implies that the recorded electrochemical signal is caused directly by the analyte compound, for example, in voltamperometric techniques the registered current is generated by the electrochemical transformation, oxidation or reduction, of the target molecule. The indirect detection usually implies the use of a redox probe, which suffers an electrochemical process that leads to the recorded signal. The electrochemical reaction of the analyte can be affected by chemical or physico-chemical process occurring at the electrode surface.

The direct strategies are usually easier to develop and implement, although, less sensitive and most importantly, less selective. Considering that the electrochemical transformation of the target molecule is happening at a certain functional group, it is easy to predict that this means that a large number of related compounds, will have similar electrochemical signals, almost indistinguishable[56,57]. This disadvantage has been also demonstrated for certain classes of antibiotics with the same core structure, like penicilins[57] and cephalosporins[56,127].

A particular direct strategy, among the direct electrochemical strategies, that aims to overcome these disadvantages and presents an increasing interest in the recent years is the electrochemical fingerprinting (EF)[128].

Electrochemical fingerprints have been already employed for the analysis of drugs of abuse (cocaine) from street samples[129], for food quality control, for the analysis of green curry[130] and of different brands of ciders[131], for As[132] and for antibiotic analysis[127,133].

Although frequently mentioned, the term “electrochemical fingerprint” has been used to describe, different things, sometimes with unclear meaning, like the characteristic electrochemical behavior of a specific electroactive target molecule[127,134] as well as the electroanalytical response of certain electrode materials, such as gold disk electrodes[135].

To clarify this, Moro *et al.*[128] gave a definition using as a starting point other chemical fingerprints, like those commonly used in MS or X-ray spectroscopy. They defined EF as "the unique electrochemical signal or pattern, mostly recorded by voltammetric techniques at one electrode, specific for a certain molecule that can be used for its quantitative or semi-quantitative identification in a given analytical context with specified circumstances". Based on this, a detection strategy can be classified as an EF-based one when the following general criteria are fulfilled[128]:

1. The target molecule contains at least one functional group electroactive, and the signal of its electrochemical behavior is used to identify or quantify it.
2. The proposed EF is directly linked to a certain given analytical context, characterized by well-defined working conditions, such as pH or electrode material, in which the detection occurs.

The use of additional supporting analytical methods is also strongly encouraged, to characterize the different processes and pathways involved in the EF in order to better identify which reactive groups of the target molecules are directly responsible for the observed redox signals.

These criteria help in the clarification of the concept of EF, by putting on a more particular EF, more related to the working conditions and analytical characteristics, like the influence of the matrix and of the possible interferents. Another possible interpretation is a broader one, with more emphasis on the target analyte and on the exploitable particularities of the pattern of its electrochemical signal in a larger variety of working condition. This second approach can represent an initial phase, when considering a certain analyte, which can be further developed for a specific application.

Regarding the use of EF for antibiotics, there are few studies[90,127,133,136]. Moro et *al.*[133] studied the electrochemical fingerprint of cefquinome, employing for the final method, conductive MIPs, electropolymerized onto electrodes modified with carbon nanotubes (CNT). This final platform allowed the detection of cefquinome in the nanomolar range using SWV[133].

In photoelectrochemical sensing applications, it is possible to obtain a fingerprint based on the shape of the current during illumination (photocurrent) by using CA. Neven *et al.* [136] observed that the shape of the photocurrent changes with buffer pH and correlated these changes to the pKa of the phenolic groups involved, like in the case of doxycycline (DXC) and CFD[128,136].

More advanced electrochemical fingerprints have been constructed also, which combined the electrochemical detection with LC-MS analysis. The use of MS allowed also for the investigation of the electrooxidation mechanism of the targeted analytes. Sleegers *et al.* investigated the EFs of three cephalosporin antibiotics by using SWV as electrochemical technique[127]. Analyzing the oxidation products with LC-MS, they proposed an oxidation mechanism for the cephalosporin core structure. Similarly, VAN was characterized by Feier *et al.*[90] using a combination of DPV and MS analysis. The electrochemical fingerprint for VAN was constructed by combining the data of the reduction and oxidation behavior and an oxidation mechanism was proposed.

4.2. Biomimetic sensors. Biomimetic elements

The direct electrochemical detection approach is easy to implement and, depending on the target molecule, can be very sensitive, but still has significant drawbacks regarding selectivity. This is especially apparent when analyzing complex matrices, like biological fluids or wastewater[54]. To confer selectivity, the electrochemical sensor can include certain recognition elements, with a strong affinity to a certain compound. Over the time, a large plethora of types of recognition elements have been used, either chemical (complexes[137], catalysts[138,139]) or biological (enzymes[96] or antibodies[106,140,141]).

All these types of recognition elements have certain disadvantages. The chemical ones, although relatively easy to synthesis and stable, have limitations in the types of analytes that they can target (e.g., complexes tend to be used mainly for metal cations). The biological ones, although presenting high selectivity, tend to be very sensitive to certain working conditions (e.g., low or high pH, high temperatures) and also have important drawbacks in terms of reproducibility. For example, the enzymatic activity is highly dependent on the working temperature. There is also higher variability in terms of characteristics between different batches of the same biological product, a problem less present in synthetic products.

A solution to these problems can be a different type of recognition element, situated somewhere in the middle of the previous two mentioned, the biomimetic elements, more specifically MIPs and APTs.

Considering that the selective molecular recognition is the very essence of many biological processes, with utility not limited to sensoristics, the idea to substitute the biological elements (antibodies and enzymes) by “biomimetic recognition elements”, either on the basis of nucleic acids or fully synthetic polymers, has fascinated a large community of scientists from numerous fields.

Biomimetic binders have been created in order to substitute the biological ligands in separation techniques and bioanalysis. The two major approaches use either “evolution in the test tube”[142] of nucleotides for the preparation of APTs or total chemical synthesis for MIPs[117,142].

The reproducible production of APTs is a clear advantage, whilst the preparation of MIPs typically leads to a population of polymers with many binding sites. The realization of binding sites in the total bulk of the MIPs results in a higher binding capacity, however, on the expense of the accessibility and exchange rate. Furthermore, the readout of the bound analyte is easier for APTs, since the integration of signal-generating labels is well established[117,142,143].

On the other hand, the overall negative charge of the nucleotides makes APTs prone to non-specific adsorption of positively charged constituents of the sample and the "biological" degradation of non-modified APTs and ionic strength-dependent changes of conformation may be challenging in some application[142,143].

4.2.1. Molecularly imprinted polymers

A broad spectrum of "selective sorbents" and later of synthetic polymers with specific binding sites — so called MIPs —has been developed based on early concepts of Polyakov *et al.*[144] and Dickey *et al.*[145].

The general concept of developing MIPs involves two important steps (**Fig. 3**). First step consists in the polymerization of one or several functional monomers in the presence of the target compound, resulting in heterogeneous polymer that has incorporated inside molecules of the target compound, also called the template. The second step is the removal of the incorporated target, or a part of it, from inside the polymer, leaving behind "imprinted" cavities that are ideally complementary in size, shape, and functionality to the target molecule. Through these two important steps, a synthetic polymer can be obtained that bears the imprint of the target, providing sites for the specific rebinding of the template[142].

The prerequisite of a successful molecular imprinting is the interaction of the target through covalent (pre-organized approach)[146] or non-covalent (self-assembly approach)[147,148] bonds with certain, specific chemical moieties of the functional monomers in the pre-polymerization mixture. This arrangement is fixed in the subsequent polymerization of the functional monomers and reaction with a cross-linker[142].

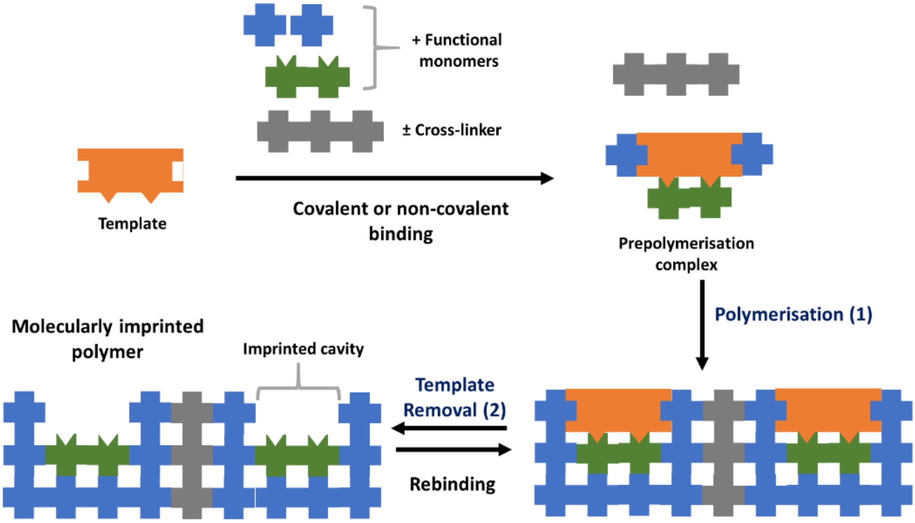

Fig. 3. Simplistic workflow of MIPs preparation.

4.2.2. Aptamers

APTs appeared when a new, *in vitro* method, called SELEX (Systematic Evolution of Ligands by EXponential Enrichment), was reported, for the selection of nucleic acids capable of binding to a target molecule with high affinity and specificity[149,150]. These nucleic acids were called "aptamers", a term derived from the Latin word *aptus* and the Greek word *meros* signifying "parts that fit". APTs are primarily short, single-stranded nucleic acids, DNA or ribonucleic acid (RNA), with a typical length of 20 to 120 nucleotides[151]. Nucleic acids can fold into manifold complex three-dimensional structures as a function of their sequence and the conditions of their solvents[152,153]. These structural varieties enable very specific and high-affinity binding to a target molecule as a result of a combination of hydrogen bonds, π–π stacking and electrostatic interactions.

Hence, APTs have already been selected against a multitude of targets, from small organic molecules[149,154] like amino acids[155] and antibiotics[143,156], to bacteria [157,158] and viruses[159] and even whole living cells[142,160].

The generation of highly specific APTs, with high affinity, requires a well-defined process of several steps (**Fig. 4**). The SELEX protocol consists mainly of repetitive cycles of incubation, binding, partitioning and amplification steps. The protocol starts with a random pool of different oligonucleotide sequences which are incubated with target molecules. During incubation, some of the sequences are bound to the target molecules but a large number of sequences are weakly bound or do not interact.

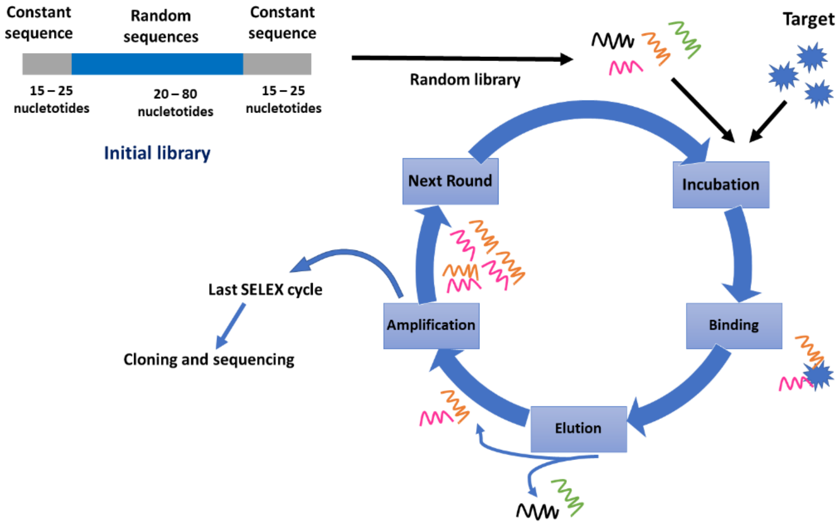

Fig. 4. Illustration of the SELEX procedure (adapted from Bayat et al.[161]).

The sequences that did not interact or were weakly bound to the target are discarded in the partitioning step, isolating only the bound sequences.

The eluted oligonucleotides are amplified by polymerase chain reaction (PCR) – in the case of DNA sequences– or reverse transcription PCR (RT-PCR) –in the case of RNA sequences– to enrich the library[143] and are reintroduced in the incubation step, beginning a new cycle.

The broad selection of successfully applied target molecules underscores the great potential of APTs as it was possible to develop APTs with dissociation constants (K_D values) in the picomolar to low nanomolar range[143], comparable and sometimes even better than those of monoclonal antibodies.

4.2.3. Biomimetic sensors. Electrochemical MIPs sensors vs aptasensors

The two biomimetic elements, APT and MIPs, have been used extensively in recent years, in the development of electrochemical biosensors for the detection of antibiotics. They offer mostly an improved selectivity, something that is difficult for the direct electrochemical strategies to achieve. They also present higher chemical and thermal stability. They are more economically accessible and easier to tailor for specific target and detection strategy. This means that are more adaptable to various modifications and additions, like linkers and labels, for APTs, or metallic nanoparticles (NPs) inserted in the structure of the polymer, in the case of MIPs.

Another important advantage that makes them suitable for their employment in the field of electrochemical biosensors is their compatibility with the miniaturization of the electrochemical techniques and the ease with which they can be attached to the surface of the electrode. An important role in their attachment is played by the various nanomaterials, especially by AuNPs, used for the modifications of the electrodes.

Although included in the same category and fulfilling roughly a similar role, the practical aspects of the use of MIPs and APTs vary significantly.

In principle, the measuring process by biomimetic sensors can be divided into two essential steps:

1. Molecular recognition of the analyte by the APT or MIP, which is determined by the corroborative effect of the composition/sequence and spatial arrangement of the respective biomimetic elements.

2. Generation of a measurable signal as a result of the interaction of the target-biomimetic recognition element with the transducer.

The first step is specific to each category of analyte and strongly influences the possible pathways for the second step.

For the construction of MIP-based electrochemical sensors, one of the most convenient and most employed strategies involves the use of electropolymerization, which offers a quick method of fabrication and one that also allows for easy control of the properties of the imprinted polymeric film (through the modification of the parameters of the electrochemical technique used for polymerization). The use of electropolymerization also implies that the MIP is already attached to the electrode surface. There are also studies that do not use electropolymerization, especially when MIPs are in the form of nanoparticles – nanoMIPs are employed. In this case, the nanoMIPs are usually synthesized and characterized through other methods and afterward suspended and used to modify the electrode surface through drop-casting.

The binding of the analyte by the MIP-based sensor can be generally exploited in two ways. One approach implies the detection of an analyte that produces a direct electrochemical signal and the use of a conducting polymer (**Fig. 5A**). In this protocol, the increase in the bound analyte results in an increase in the signal. One advantage of this approach is the additional element of identification, provided by the specific electrochemical signal of the analyte.

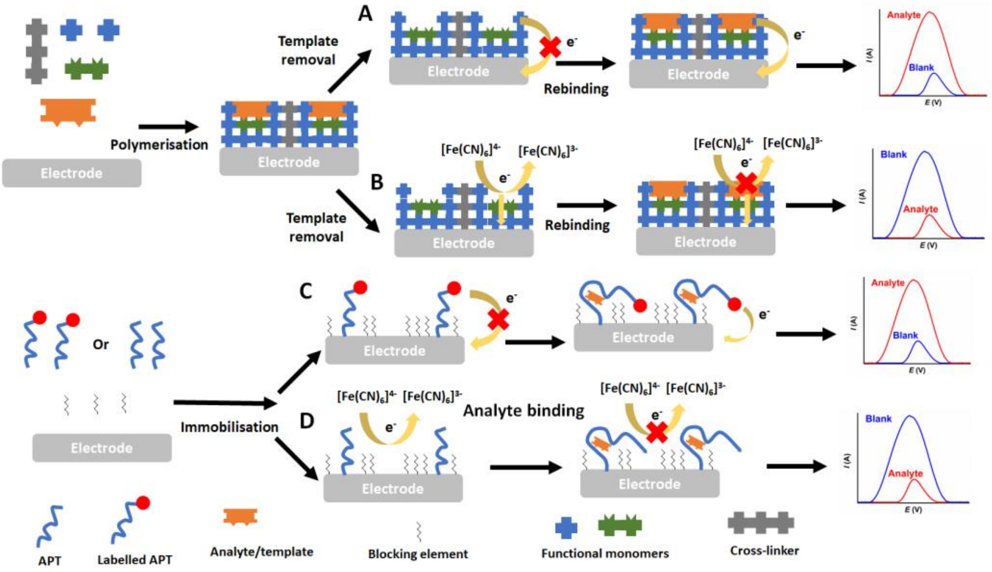

Fig. 5. Comparison between MIP-based and APT-based electrochemical sensors: MIP-based, direct (**A**) and indirect (**B**) approach and APT-based, labeled (**C**) and label-free (**D**) approach.

A second and more often employed approach is an indirect one, which measures the increase in the resistance to charge transfer of the MIP film, which is proportional with the amount of "imprinted" cavities re-occupied by the analyte (**Fig. 5B**). This change in resistance is measured using a redox probe. Even though in this approach the electrochemical signal of the analyte is not present, the methods employing this strategy tend to have increased sensitivity.

In the construction of an electrochemical aptasensor, the APT sequence is usually immobilized through one end onto the electrode surface, using a linker. For the immobilization, two common strategies are employed, involving either the Au-S bonds, formed by alkanthiols, or the amidic bonds formed between amino and carboxyl groups. The end result is that the elongated APT sequence is immobilized perpendicularly onto the transducer surface, with one end free. The interaction of the APT with the target leads to a conformational change, with the formation of the APT-analyte complex, the sequence adopting a more compact conformation, bringing the outer end of the sequence closer to the electrode surface and also entrapping the analyte onto the sensor surface.

This conformational change can be exploited in several ways. One involves using a labeled APT (**Fig. 5C**), at the distal end of the APT, which means that the conformational change translates in an increase of the electrochemical signal, due to the closer proximity of the label to the electrode. A second approach (**Fig. 5D**) involves the use of a label-free APT and a redox probe in the solution, the signal of which decreases proportionally with the binding of the analyte and the conformational change, due to an increase in the resistance to charge transfer.

4.3. Nanomaterials employed in the construction of electrochemical sensors

Discoveries in the field of nanomaterials have intensified greatly in the last two decades, their use spreading in various scientific and technological fields, including electrochemical methods of analysis. Their use for electrode modification, to optimize methods, has become a common practice [54,162].

The main advantages of their use in electroanalysis derive directly from their size:

- Increase of the electroactive surface area due to the large surface-to-volume ratio of the nanoparticles
- By changing the electron transfer surface, from a smooth to a nanostructured one, the diffusion process changes partially from a linear to a radial one
- The small spatial dimensions of nanoparticles can allow a direct, intimate electrical connection with biological affinity elements
- Very small spatial dimensions allow a stable number of molecules to be fixed on the nanostructured surface of the electrode[54,162]

Electrode surfaces modified with nanostructures make specific connections with the analyte through them. Nanostructures have practically an electrocatalytic activity resulting in the reduction of the potential at which a process takes place or the amplification of the electron transfer resulting from the process. All of this ultimately helps to achieve larger and better-defined oxidation or reduction peaks.

Owing to the unique physical and chemical properties, nanomaterials are considered as the most attractive option in the design and construction of "functional" transducers for electrochemical biosensing systems. The flexibility of these systems in terms of post-modification or functionalization has helped improve the analytical performance dramatically for the detection of antibiotics.

The main representatives among nanomaterials, with applications in the field of antibiotics electroanalysis, are carbon-based nanomaterials, like CNT, graphene, or metal-based nanomaterials, generally nanoparticles or nanostructures. In general, metals such as Au, Pt, Pd, Ag, Ti, Mn, Ni, Cu or metal oxides of these metals, like TiO_2 or MnO_2, are used to obtain NPs for electrode modification (**Fig. 6**)[53,54].

Carbon is an extremely interesting element because it can have various hybridization states including sp, sp^2, sp^3, and sp^2-sp^3 combinations[162,163]. Due to its inherent attributes (e.g., high chemical stability, biocompatibility, high electrical conductivity, and robust mechanical strength), carbonaceous nanomaterials are recognized as promising options for diverse biosensing applications. The unique electrochemical properties of carbonaceous nanomaterials depend on the diverse synthesis procedures. Therefore, many morphological variants of carbons (such as zero to three-dimensional scales) have been employed conveniently as “nanoprobes” for routine biosensing applications[162,163] .

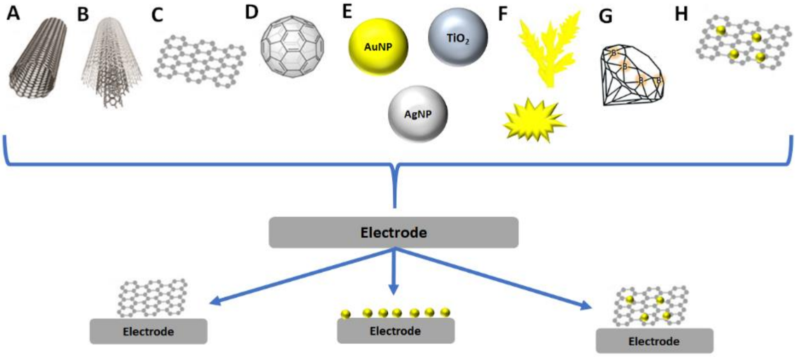

Fig 6. Nanomaterials used for electrode modification: (**A**) single-walled CNT (SWCNT), (**B**) multi-walled CNT (MWCNT), (**C**) graphene, (**D**) fullerene, (**E**) Metal or metal oxide NP (AuNP, AgNP, TiO_2 NP), (**F**) AuNSs, (**G**) BDDE and (**H**) graphene-AuNPs composite.

In addition, carbon-based nanomaterials are often called "doped" hybrid materials, such as CNT, doped graphene or fullerenes. These doped carbon-based nanomaterials are obtained by substituting carbon atoms with atoms of other elements, e.g. BDDE[162,163].

Metal nanoparticles and metal oxide nanoparticles have been also used extensively for electrode modification and implicitly in the development of electrochemical biosensors. These nanoparticles possess good electrical and photocatalytic properties because of their size, shape, stability, and larger surface area. Biocompatible metallic nanoparticles are generally used to immobilize biomolecules onto the electrode surface, to produce various biosensors or as electrochemical markers[54,164]. From all, AuNPs possess the most distinct and highly favorable physicochemical properties for diverse sensing applications, being commonly combined with bio-recognition elements like APTs, enzymes, or antibodies[54]. Certain NPs can have more special properties and uses. For example, Ni or NiO and Cu or Cu oxides are used as catalysts for the oxidation of organic compounds, like carbohydrates, in an alkaline medium[165]. Another example is the extensive use of TiO_2 as a photocatalyst in photoelectrochemical detection[166].

Modification of the electrode surface with metallic NSs or NPs, is usually achieved either through electrochemical deposition of a metallic precursor, or drop-casting of a preformed nanoparticulated material[167].

4.4. Photoelectrochemical methods – Singlet oxygen strategy

The concept of “photoelectrochemical (PEC) sensing” is relatively new, probably less than two decades. Regardless, PEC sensing has witnessed rapid development recently as an important branch of electrochemical detection[168].

Photoelectrochemistry evolved from electrochemistry as the discipline that explores the effect of light on photoactive materials, also involving the transformation of light into electricity and interconversion of electric energy and chemical energy.

It is accepted that the photoactive materials absorb photons with enough energy to produce electron–hole pairs. The subsequent transfer of the photogenerated charge carriers to the electrode generates the electrical signal, and the participating redox reactions implement the energy conversion[168].

PEC sensing employs photoactive materials on the electrode interface as the signal converter. These materials generate an electrical signal under light irradiation that can be affected by the interaction with the targeted analytes. In the entire PEC detection system, the generation of the electrical signal involves a series of physical and chemical processes.

A particular strategy of PEC sensing is the singlet oxygen-based electrodetection of phenols, developed by Trashin *et al.*[169] (**Fig. 7**). This strategy is different from the traditional PEC sensing systems as it encounters an energy-based transfer rather than an electron transfer.

The electrochemical detection of phenols using enzymatic biosensors, mainly based on the use of HRP, is a well-known analytical method[170–172]. The use of an enzyme in the electrochemical detection of phenolic compounds brings an advantage due to the catalytic signal amplification, which translates into high sensitivity and low limits of detection (LOD). However, enzymatic biosensors have limitations, such as complexity of the fabrication due to thermal and chemical instability of enzymes, a comparatively short shelf life of biomolecules and issues with the reproducibility of enzymatic activity in different batches[173,174].

The singlet oxygen-based strategy was created with the aim to overcome the shortcomings of enzymatic biosensors, like thermal and chemical instability of enzymes[173,174] and it is usually used for the detection of phenols.

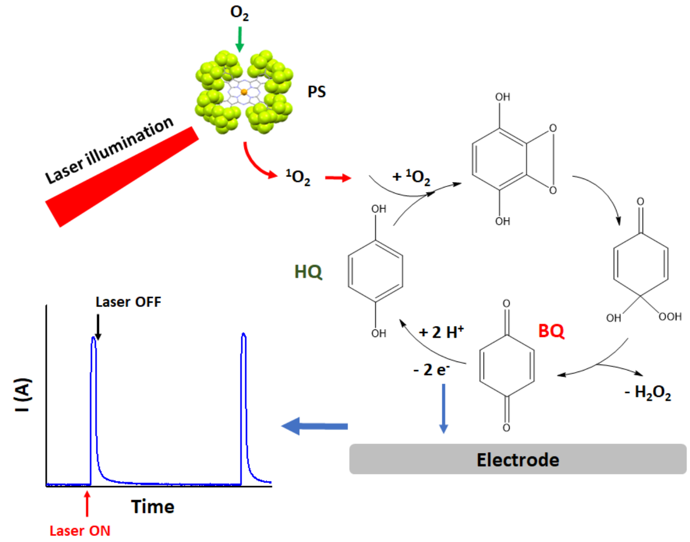

Fig. 7. Singlet oxygen-based detection strategy; PS – photosensitizer, HQ – hydroquinone, BQ – benzoquinone.

It swaps the biological catalyst with a robust photosensitizer type II (perfluorinated zinc phthalocyanine), capable of generating singlet oxygen under illumination by red light in aerobic condition[169,175]. The photosensitizer acts as a photocatalyst mimicking the kinetic scheme of a biocatalyst (HRP or phenol oxidase) in biosensors although via a different molecular mechanism, i.e. [4+2] cycloaddition of singlet oxygen ($^1O_2$) to a phenolic moiety followed by the formation of a corresponding quinone. The product can be electrochemically reduced in mild conditions back into a phenolic compound –expectedly, hydroquinone (HQ) or its derivative– completing the electrocatalytic loop[136,169], similar to the action of peroxidases[172]. Moreover, the response related to the photocatalytic action appears only under light illumination and, thus, a baseline current can be instantly distinguished from a useful signal by switching the light off[136,169].

The method was developed using HQ as a prototype analyte, to better reveal the mechanism, but it was quickly expanded for more complex analytes, especially phenol-containing antibiotics, like in the case of AMX[169], RIF[138], DXC and CFD[136]. The strategy showed great sensitivity and an inherent certain selectivity by targeting only phenol-containing compounds, selectivity which has been shown that can be further improved, based on the influence of the working conditions (e.g. the pH and the potential applied for the detection) on the phenolic compounds response[136].

PERSONAL CONTRIBUTIONS

Chapter I. The development of direct electrochemical methods for the detection of antibiotics

1. The complex fingerprint of vancomycin by electrochemical and mass spectrometry analysis

1.1. Introduction

The most important and well-known glycopeptide antibiotic, VAN is used for the treatment of severe bacterial infections, like MRSA infections, endocarditis caused by enterococci, bone, lower respiratory tract, soft tissue infections and sepsis[176].

The aim of this study was the development of a complex fingerprint, involving a battery of tests, in oxidation and reduction domains, using commercially available screen-printed electrodes (SPEs), with different materials as working electrode, different analysis procedures, and several electrolytes and using the pretreatment of the VAN solution. All these simple and rapid tests led to the formation of a specific electrochemical fingerprint for VAN.

In order to explain the electrochemical behavior of VAN, the mechanism of its anodic oxidation was elucidated for the first time by HPLC-MS analyses of the oxidation products obtained after small scale electrolysis.

1.2. Experimental

1.2.1. Chemicals and instrumentation

All chemicals and the commercial human serum were of analytical grade and purchased from Merck, except VAN hydrochloride (from Linaris, Germany) and gentamicin sulphate (GEN) (from Bioworld, USA). All solutions were prepared with ultrapure water (18.2 MΩ, Millipore Simplicity).

The electrochemical experiments were performed using an AUTOLAB PGSTAT 302N (Ecochemie, The Netherlands) equipped with the associated NOVA 1.10.4 software. All the SPEs, [carbon-based (C-SPE); carbon-based modified with carbon nanotubes (CNT-SPE); carbon-based modified with graphene (G-SPE); carbon-based modified with carbon nanofibers (CNF-SPE); gold-based (Au-SPE); carbon-based modified with AuNPs (AuNPs-SPE); platinum-based (Pt-SPE)] were purchased from

Dropsens (Spain). The HPLC-MS/MS experiments were conducted using an Agilent 1100 series HPLC system (Agilent Technologies, Germany), using a Gemini-NX C18 50mm×2.0mm i.d., 3.5 µm column (Phenomenex, USA), coupled with an Agilent Ion Trap SL MS (Brucker Daltonics, Germany) equipped with an electrospray ion source (ESI).

1.2.2. Electrochemical techniques and pretreatment methods

Three electrochemical techniques, CV, chronoamperometry (CA) and DPV, were employed in this study. CV experiments were performed on all seven types of SPE, using 5 mM VAN solutions in 0.1M H_2SO_4, in phosphate buffer saline solution (PBS) pH 7.0 and PBS pH 12.0, in the potential window −1V to +1.2 V, with a scan rate of 0.1 $V{\cdot}s^{-1}$.

The CA method was used in the electrolysis studies. DPV was used following the CV tests to monitor the oxidation behavior of VAN, in order to better construct the complex electrochemical fingerprint (CEF). The parameters used were: pulse height 0.1 V; pulse width 50 ms; scan rate 0.02 $V{\cdot}s^{-1}$. Multiple consecutive DPV scans were also run to observe the behavior of possible adsorbed oxidation products. DPV was also used to characterize the interaction between VAN and AuNPs in the reduction domain, the pulse height being −0.1 V in this case. For better visualization, all the DPV voltammograms presented here were baseline-corrected using the moving average filter included in the NOVA 1.10.4 software (window size 1), without affecting the results.

In order to achieve hydrolysis or a certain degree of degradation of the VAN molecule, chemical pretreatments using strong acidic or basic solutions were tested[177,178]. The electrochemical response of 0.1 mM VAN solutions in 0.1 M H_2SO_4 was tested after a previous chemical pretreatment of 1 mM VAN for 15 min in 0.5 M NaOH or 0.5 M H_2SO_4 at 75 °C. As a control test, an aqueous solution of VAN was tested in a similar way.

1.2.3. Selectivity tests and real samples analysis

Spiked samples of commercially available human serum were prepared as follows: 10 µl of VAN stock solutions was added to 990 µl of untreated serum and then 50 µl of $HClO_4$ 70% was used to precipitate the protein and the mixtures were centrifuged for 10 min at 10,000 rpm. 100 µl of the supernatant was diluted with 100 µl of 0.1M H_2SO_4 and this mixture was analyzed with multiple successive DPV scans using C-SPE. Unspiked samples were prepared and analyzed in an identical way.

1.2.4. Electrolysis and HPLC-MS/MS procedures

In order to elucidate the mechanism behind the electrooxidation of VAN, the molecule was subjected to advanced electrolysis at fixed potential using a G-SPE on which 120 µl of 1 mM VAN solution in 0.1 M H_2SO_4 had been dropped, and a constant potential of +0.9 V (corresponding to peak potential plus 0.1 V) was applied for 75 min. A portion of the 1 mM VAN solution was kept under the same conditions, without applying any potential, to test the possible non-electrochemical degradation of VAN. After electrolysis, 30 µl of both solutions were diluted 100 times with the mobile phase and injected into the RP-HPLC-MS/MS system. For the RP-HPLC-MS/MS analysis, the mobile phase was composed of 0.1% acetic acid (V/V) in water and acetonitrile (ACN), under gradient elution, with a flow of 0.6 ml/min. The elution gradient was as follows: from 15% to 95% ACN (linear gradient for the first 5 min) and constant 95% ACN until 6 min. The mass spectrometer was operated in positive Auto MS/MS mode, using nitrogen as a nebulizer and drying gas. The scan speed was 5500 amu·s-1 and the scan range was 500–1500 m/z. The capillary voltage was −4000 V, the nebulizer was set at 60 psi and the dry gas flow was 12 l/min at 350 °C.

1.3. Results and discussion

1.3.1. The electrochemical fingerprint of vancomycin

The determination of the VAN fingerprint involved the determination of the voltamperommetric behavior of VAN at C-based SPEs (bare C-SPE and modified with CNTs, graphene and CF), at Au-based SPEs (Au-SPE and AuNPs-SPE) and at Pt-SPE (**Fig. 8**). At C-SPE, VAN presents only irreversible oxidation peaks: one at 1 V, one at 0.6 V and two peaks at 0.15 V and 0.6 V at pH 1.0, 7.0 and 12.0, respectively, with the best-defined peak at pH 6.0 and largest currents at pH 12.0. At G-SPE, the recorded currents are larger, but a well-defined peak (at 1 V) is obtained only at pH 1.0.

At CNT-SPE, the electrochemical behavior of VAN is very similar to the one at C-SPE, the currents being larger, and the peaks are better defined. At CF-SPE, at pH 1.0, the large oxidation peak for VAN can be used only after blank subtraction, because a smaller peak is obtained at 1 V also for the blank; at pH 7.0 the peak obtained is the well-defined, but still smaller than the one obtained at pH 1.0; at pH 12.0 VAN presents just one small, oxidation peak at 0.9 V. In the case of Pt-SPE, VAN presents a signal distinguishable from the blank only at pH 1.0, when a peak is obtained at 0.9 V.

Both Au-based SPEs led to large oxidation peaks for VAN at pH 1.0, but oxidation peaks (small for AuNPs-SPE) were obtained for the blank also. For the Au-SPE no usable electrochemical oxidation signal was obtained at pH 7.0 and 12.0, but for the AuNPs-SPE at pH 7.0 a peak at 0.65 V and one at 1.05 V were obtained, larger than in the case of blank. Also, at pH 12.0, a small peak is obtained at 0.5 V.

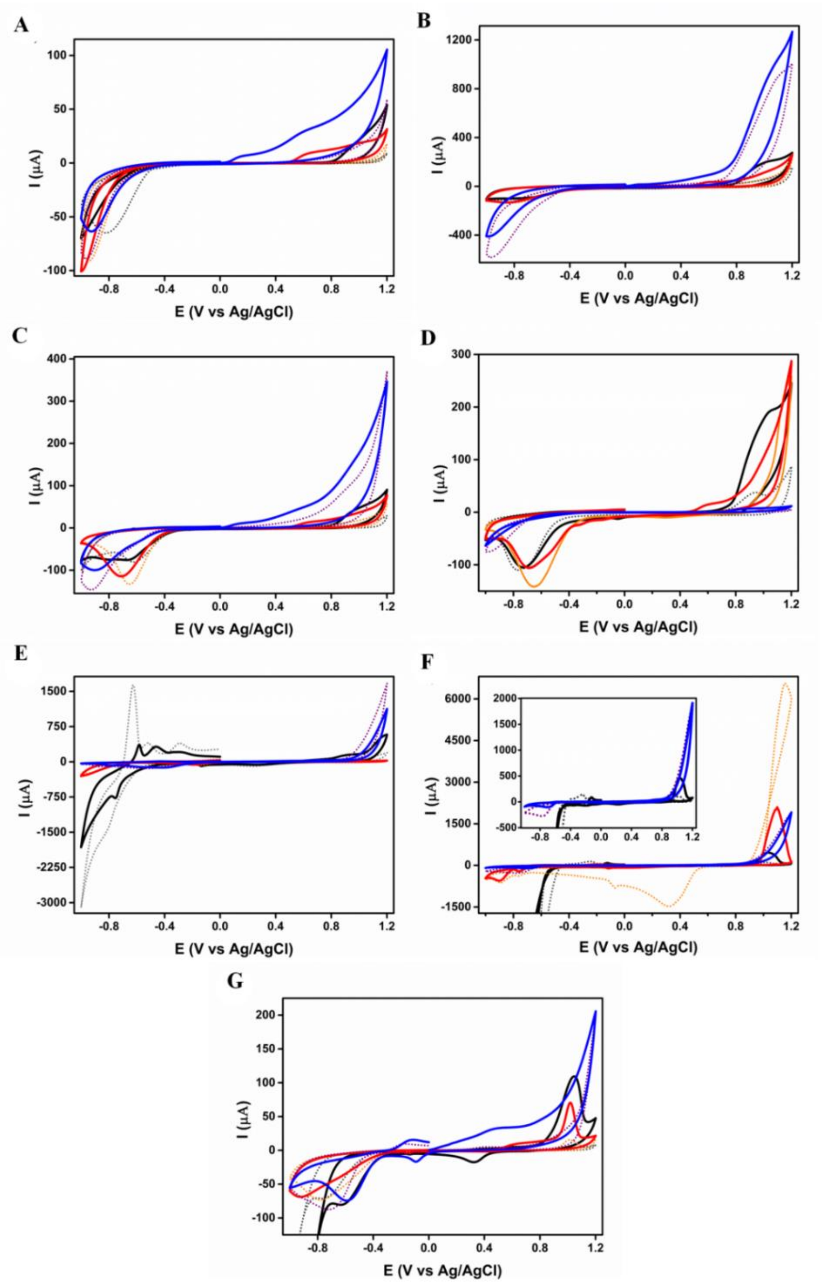

Fig. 8. CVs of 5 mM and the blank VAN solutions at: (**A**) C-SPE, (**B**) G-SPE, (**C**) CNT-SPE, (**D**) CNF-SPE, (**E**) Pt-SPE, (**F**) Au-SPE (inset: zoomed area) and (**G**) AuNPs-SPE at pH 1.0 (**dark** and **dotted grey**), pH 7.0 (**red** and **dotted orange**) and pH 12.0 (**blue** and **dotted purple**);

Interestingly, the Au-based SPEs offer the possibility to analyze VAN in reduction. A reduction peak at 0.25 V was obtained at Au-SPE only at pH 1.0, while using AuNPs-SPE a reduction peak at 0.35 V was obtained at pH 1.0 and one at -0.1 V at pH 12.0.

Depending on the sample to be analyzed (concentration, matrices, possible interferents) only certain analyses, in well-established conditions may be performed (oxidation or reduction, on certain types of electrodes).

The VAN presents a characteristic behavior at successive DPV analyses, without cleaning steps between them (**Fig. 9A**), with the peak at 0.65 V decreasing and the peak at 0.2 V increasing after every DPV analysis. This suggests a further oxidation process of the first product of oxidation.

The previously reported interaction between VAN and different forms of Au (AuNPs or ionic $AuCl_4^-$)^{179} could be exploited in electroanalyses. These interactions were investigated by performing DPV analyses from 1.2 V to 0 V at Au-SPE in a VAN solution and at C-SPE in a VAN solution containing $HAuCl_4$ (**Fig. 9B**).

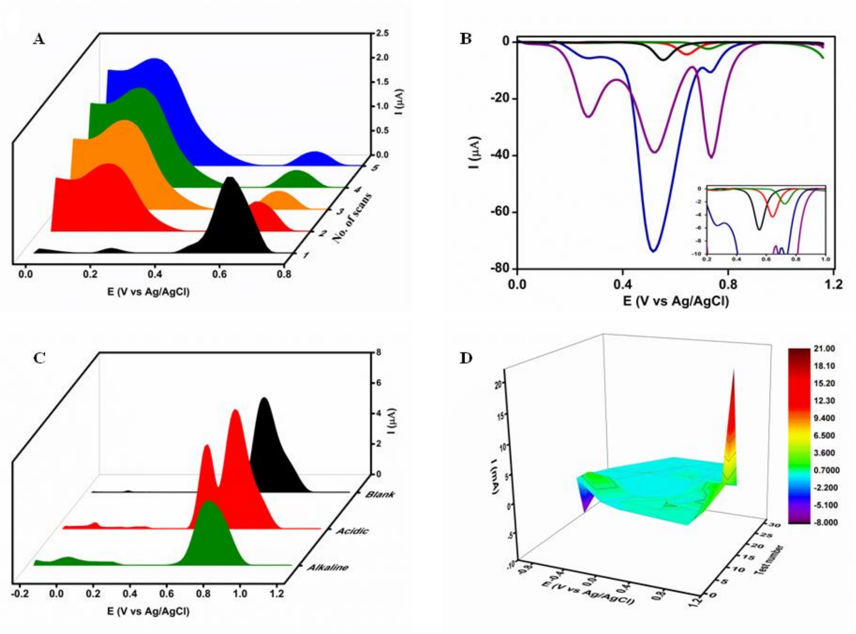

Fig. 9. (**A**) Consecutive DPVs of 10 µM VAN in 0.1 M H_2SO_4 at C- SPE; (**B**) DPVs at AuNPs-SPE for blank (**black**), VAN 0.1 mM (**red**), VAN 1 mM (**green**) in 0.1 M H_2SO_4 and at C-SPE for 1 mM $HAuCl_4$ (**blue**) and for a mixture of 1 mM VAN and $HAuCl_4$ in 0.1 M H_2SO_4 (**purple**) (inset: zoomed area); (**C**) DPVs at C-SPE of 0.1 mM VAN in 0.1 M H_2SO_4 after acid (**red**) and alkaline (**green**) pretreatment and for blank (**black**); (**D**) The 3D electrochemical fingerprint of VAN incorporating the results **A-C** (the anodic peaks were 10x amplified).

In the case of Au-SPE (**Fig. 9B**), the increase in VAN concentration resulted in smaller reduction peak and at more anodic potential compared to the peak obtained in the absence of VAN. At C-SPE, the presence of VAN leads to appearance of three reduction peaks at 0.75 V, at 0.575 V and 0.275 V, compared to only one larger peak at 0.575 V obtained for $HAuCl_4$ alone.

The simple pretreatment of the VAN solution (15 minutes heating at 75º C of VAN solution in a strong acid solution and in a strong base solution) determines the appearance of characteristic anodic peaks (**Fig. 9C**).

The DPV of VAN, after acid pretreatment, shows a peak at 0.725 V, slightly reduced in area, than the same peak for the untreated VAN and another peak, smaller, at 0.575 V, suggesting that the VAN acid hydrolysis allows the easier anodic oxidation of VAN, at a different moiety. The DPV of VAN, after alkaline pretreatment, reveals a decrease of the peak at 0.725 V and a smaller peak at 0 V. These results show that the simple pretreatment can facilitate the electrochemical identification of VAN.

The results obtained using an accessible battery of electrodes and tests can be combined and incorporated into a CEF, (**Fig. 9D**). Having this complex fingerprint, the analysis of VAN can be easily adapted according to the purpose of the analyses and type of samples (matrix), performing only specific tests.

1.3.2. The mechanism of electrooxidation

In order to investigate the products of VAN electrochemical oxidation, LC-MS/MS analyses were performed on the electrolyzed and non-electrolyzed VAN solutions. The total ion chromatogram for electrolyzed VAN solution (**Fig. 10A**) presented a peak with the retention time (RT) of 5.1 minutes, corresponding to non-electrolyzed VAN, since the HPLC-MS/MS extracted ion chromatogram confirmed the presence of VAN characteristic ion[48,180] at m/z 724.8 (**Fig. 10B**) and a peak with RT of 4.2 minutes, corresponding to an ion at m/z 732.8, attributable to the VAN electrooxidation product. The theoretical molecular weight of the product corresponds to the molecular weight of VAN plus 16, suggesting the insertion of an oxygen atom onto the original structure of VAN.

The MS/MS spectra revealed a similar fragmentation pattern for VAN and the oxidation product and also with those present in literature[48,180]. The obtained ions at m/z 1305.5 and at 1143.4 for VAN (**Fig. 10D**) and at m/z 1321.5 and 1159.4 for the oxidation product (**Fig. 10E**), strengthens even more the hypothesis of one oxygen atom addition. Based on the fragmentation products it can be deduced that the insertion of the oxygen takes place in the peptidic part of the molecule, since the glycosidic part is lost during fragmentation and the same difference of 16 is observed for the fragments of VAN and of the oxidation product.

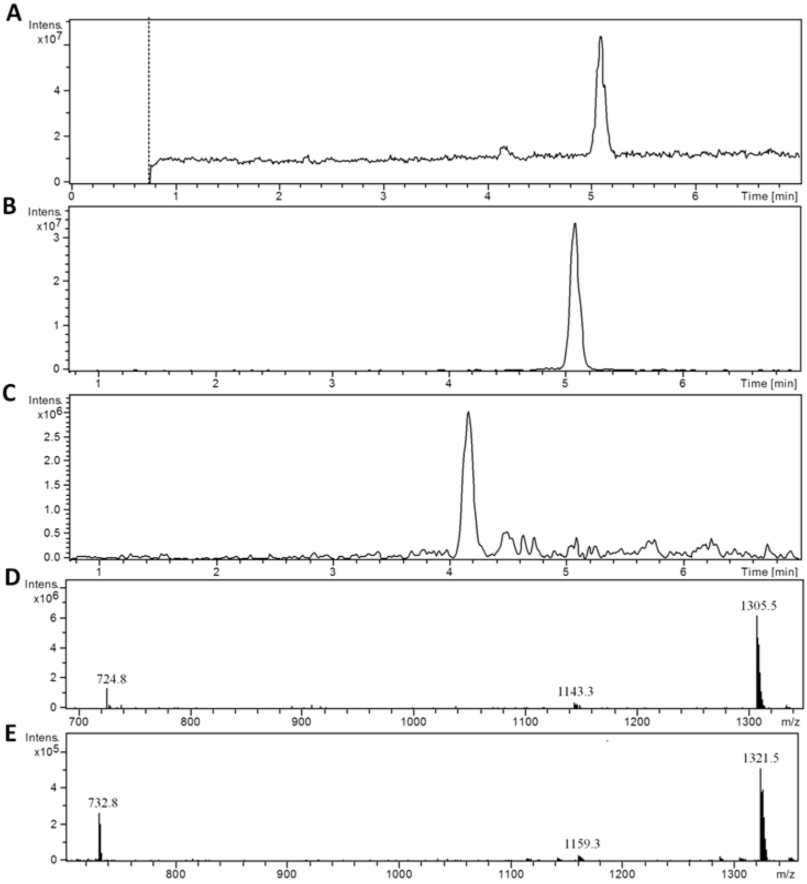

Fig. 10. (**A**) Total ion chromatogram for VAN solution after electrolysis; (**B**) extracted ion chromatogram for VAN and (**C**) oxidation product; (**D**) MS/MS spectra for VAN and (**E**) oxidized VAN.

A mechanism of electro-oxidation of peptides containing tyrosine proposed a pathway involving an electrochemical step, in which two electrons and one proton are lost, followed by a chemical step, involving the reaction with a molecule of water, simultaneously with the loss of one proton[181,182]. Therefore, based on the structural similarities, on the experimental electrochemical and HPLC-MS/MS data, we propose a combined electrochemical-chemical mechanism, for the VAN electrooxidation, involving the loss of two electrons and one proton, in the first step, the electrochemical one, and the addition of one water molecule combined with the loss of a second proton, in the second step, the chemical one (**Fig. 11**).

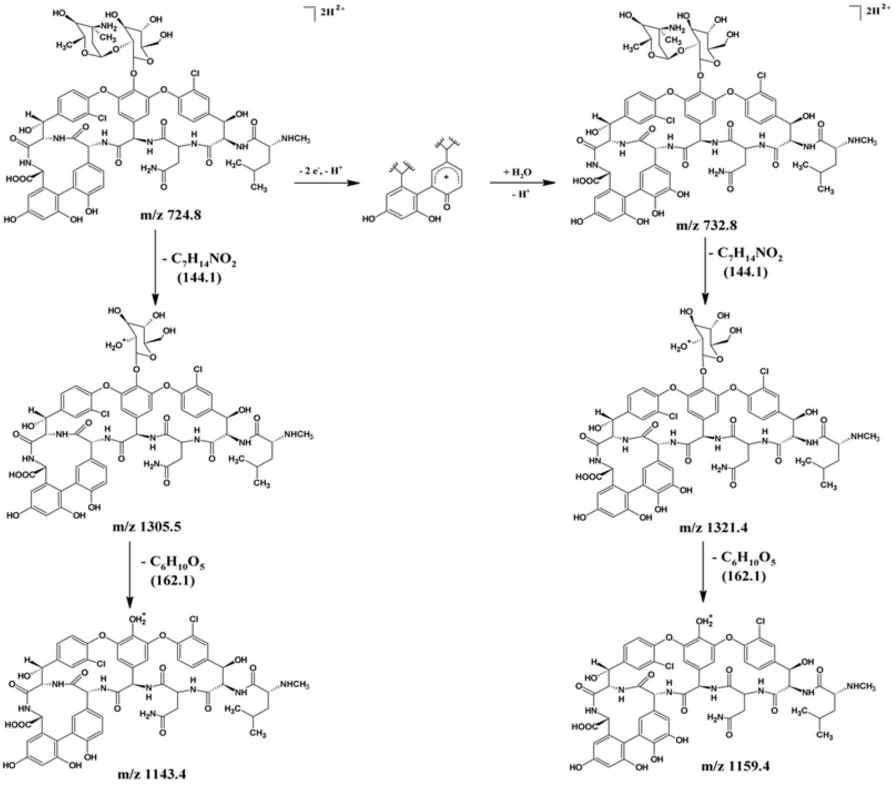

Fig. 11. Proposed mechanism for the electrochemical oxidation of VAN.

1.3.3. Selectivity tests and real samples analysis

The applicability of the proposed CEF was tested by analyzing spiked biological samples of commercially available human serum, used for therapeutic drug monitoring (TDM) of VAN. Having a battery of tests allows the identification of a specific test that allows the quantification of VAN from the required matrix. For commercial human serum analysis, multiple DPV scans on a C-SPE at pH 1.0 proved to be the best test. During the first scan, there was no clear difference between spiked and unspiked samples (**Fig. 12A**), but in the second scan (**Fig. 12B**), the interfering peak from the matrix drastically decreased, allowing the quantification of VAN.

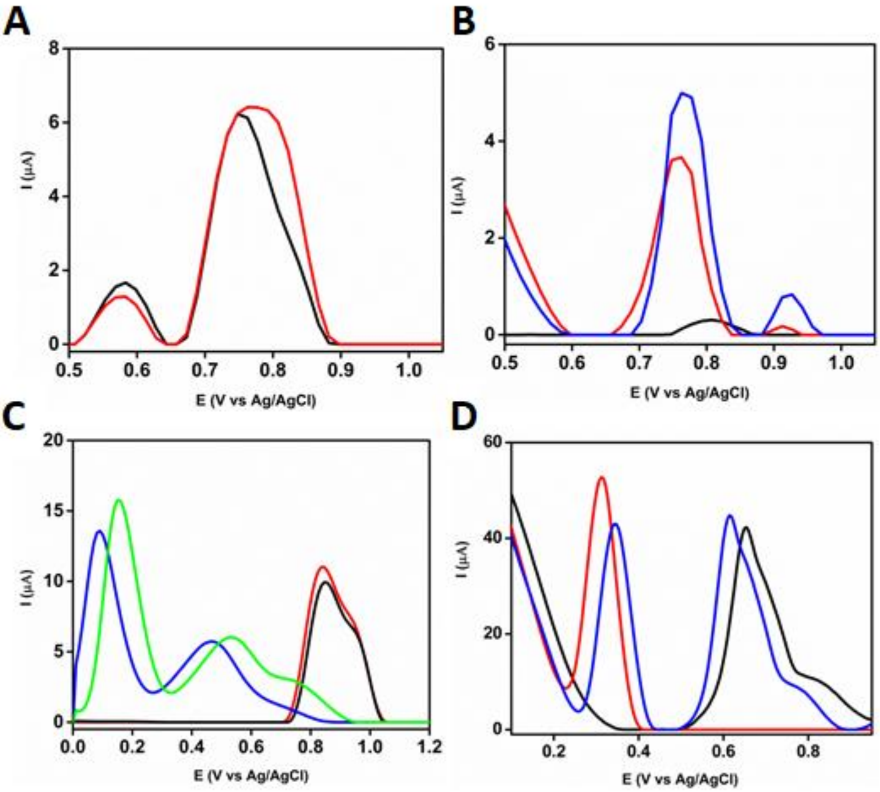

Fig. 12. Commercial human serum sample analysis: (**A**) First scan and (**B**) Second scan, blank serum (**black**), serum spiked with 25 µM (**red**) and with 50 µM (**blue**) final concentrations of VAN; Interferent studies: (**C**) DPVs on a C-SPE for 1mM VAN (**black**) and 1mM VAN and GEN (**red**), at pH 1 (in 0.1M H_2SO_4) and for 1mM VAN (**blue**) and 1mM VAN and GEN (**green**), at pH 12 (in PBS); (**D**) DPVs on a G-SPE for 50 µM VAN (**black**), for 50 µM VAN and APAP (**blue**) and for 50 µM APAP (**red**), at pH 1 (in 0.1M H_2SO_4).

The achievable selectivity for VAN detection, using the CEF, was demonstrated by measuring the response to VAN in the presence of GEN and acetaminophen (APAP) (an antipyretic drug), drugs often co-administered with VAN.

GEN strongly interferes with the VAN signal on C-SPE at pH 12, but this interference is strongly diminished in an acidic medium (pH 1) (**Fig. 12C**). Similarly, VAN could be detected easily in the presence of APAP using a G-SPE at pH 1 (**Fig. 12D**).

1.4. Conclusions

A complex electrochemical fingerprinting for VAN was obtained, which includes the electrochemical behavior of VAN at different commercially available SPEs, in several electrolytes, for successive analyses, after simple pretreatments, and using both anodic and cathodic peaks.

In order to explain the electrochemical behavior of VAN, its anodic oxidation mechanism was elucidated. RP-HPLC-MS/MS analyses allowed the identification of the oxidation product obtained after smallscale electrolysis and an electrochemical mechanism was proposed.

This complex fingerprint approach offers a wide image of the behavior of VAN and allows the easy adaptation of electrochemical methods for the detection of VAN to the specifics of the sample to be analyzed.

2. The direct electrochemical detection of vancomycin using a graphene–gold nanostructures composite platform

2.1. Introduction

The combination of graphene and gold nanostructures (AuNSs) or gold nanoparticles (AuNPs) can represent a viable alternative due to the synergic electrocatalytic effect of graphene and AuNSs towards electrooxidation of VAN, but also due to the interaction between the AuNSs and VAN, usable in the cathodic domain [90,183].

Similarly, AuNSs are an attractive nanomaterial for the fabrication of electroanalytical platforms because of their large specific surface area, good biocompatibility, strong binding ability, and excellent conductivity. The use of nanoparticles to modify SPEs offers significant advantages in enhancing the mass transference rate and the electrocatalytic activity of the electrode[184].

Two of the most common strategies used for the modification of electrodes with NS are the drop casting method and electrochemical deposition[167]. Drop casting is the easiest method, only one parameter needing to be optimized, the final amount drop casted onto the electrode. Platforms developed with this methodology are used further in two main directions: direct modification of selected NS, usually NP, onto the electrode or the ex-situ fabrication of composites incorporating NPs[167]. The electrochemical deposition strategy is the most common method, especially for SPE. This method allows an easy way to control the morphology and diposition of NSs. This methodology is based on the reduction of oxidized species, typically metallic water-soluble salts, at a fixed potential or current to obtain tailor-made metal particles grown on conductive substrates. The parameters usually optimized are separated in two main groups: (i) the ones related to the precursor solution where the salt type and concentration are involved, and (ii) the conditions of electrochemical deposition[167].

There are previously reported interactions between VAN and different forms of Au (AuNPs or ionic $AuCl_{4}^{-}$), which can be exploited in electroanalysis[90,179,185,186]. VAN can interact with $HAuCl_4$, leading to the formation VAN caped AuNPs, with enhanced antibacterial properties[179,185,186], but also with already synthesized AuNPs. This affinity of VAN for AuNSs, together with their special electrochemical properties can be exploited for analytical purposes, in the development of methods for VAN quantification.

Considering all of the above, herein, in this study, we present a simple electrochemical method for VAN sensing that uses a hybrid graphene-AuNSs nanocomposite electrode. This method allows a double detection, in one analysis, directly, in the oxidation domain and also indirectly, in reduction, using the electroactive AuNSs as probe to monitor the current changing due to the interaction between Au and VAN.

2.2. Experimental

2.2.1. Materials and instruments

HCl, Na_2HPO_4, NaH_2PO_4, NaCl, $HAuCl_4$, $HClO_4$, H_2SO_4, AMP trihydrate, PEN V potassium salt, penicillin sodium salt, OXA sodium salt, AMX, ascorbic acid (AA), APAP, and the commercially available human serum were purchased from Sigma-Aldrich (Saint Louis, MO, USA); CFX monohydrate from Antibiotice SA (Iași, Romania); VAN sulfate from Linaris, (Dossenheim, Germany); and GEN sulfate from Bioworld (Dublin, OH, USA). AuNPs of 15 and 50 nm were purchased from Nanovex Biotechnologies (Asturias, Spain). In order to test if the size of these AuNPs influences the VAN detection, these two dimensions were chosen as they are at extremes of the usual dimensions of AuNPs obtained through electrogeneration[187]. All solutions were prepared with ultrapure water (18.2 MW, Millipore Simplicity, Burlington, MA, USA). The supporting electrolyte used in this study was the solution of 50 mM PBS prepared with Na_2HPO_4, NaH_2PO_4 and NaCl, adjusted to the mentioned values of pH.

The electrochemical experiments were performed using an AUTOLAB PGSTAT 302N (Ecochemie, Utrecht, The Netherlands) equipped with the associated NOVA 1.10.4 software. All the SPEs, with different working electrodes (C–SPE, G–SPE, and carbon-based modified with gold nanoparticles –AuNPs–C–SPE–) and with a silver pseudoreference and a carbon counter electrode were purchased from Dropsens (Asturias, Spain). Spectrophotometric analyses were performed using a SPECORD 250 PLUS UV-VIS spectrophotometer (Analytik Jena AG, Jena, Germany), with 1 cm cells.

2.2.2. Electrochemical and UV-VIS characterization

Two electrochemical techniques, CV and DPV, were used for the electrochemical characterization of VAN behavior on the modified surfaces. CV experiments were performed in the potential window of -0.2 V to +1.2 V, with a scan rate of 0.1 $V \cdot s^{-1}$. The parameters used for the DPV technique were a pulse height of 0.1 V, a pulse width of 50 ms, and a scan rate of 0.02 $V \cdot s^{-1}$ for the oxidation studies, the only difference for the reduction studies being a pulse heigh of -0.1 V.

The UV-VIS studies were performed by recording the UV spectra between 200 and 350 nm and the VIS spectra between 350 and 850 nm, with a 1 nm slit, 1 nm wavelength step, and a speed of 5 $nm \cdot s^{-1}$.

2.2.3. Functionalization of the working surface with Au nanostructures

The modification of the SPEs with AuNSs and AuNPs was carried out employing two different approaches, one involving the electrogeneration of the AuNSs, directly onto the sensing surface and a second one, involving a drop-casting protocol, using a suspension of preformed AuNPs.

For the electrogeneration of AuNSs, a volume of 60 μL of an aqueous solution of 0.6 mM $HAuCl_4$ and 0.5 M H_2SO_4 was deposited on the SPE surface and two different electrochemical techniques were used, CV and CA[188]. For the CV technique, the potential was scanned in the window of -0.2 V to +1.2 V, with a scan rate of 0.1 $V \cdot s^{-1}$, for 10 cycles. For the CA technique, the main parameters used, potential and duration, are mentioned in the Results and Discussion section for each experiment.

For the drop-casting protocol, a volume of 10 μL of an aqueous suspension of AuNPs, with a particle concentration of 6×10^{11} $particles \cdot mL^{-1}$, was deposited on the SPE surface and left to dry at room temperature. This procedure was repeated up to five times, totaling a volume of 50 μL, in order to assess the influence of the amount. AuNPS of two dimensions, 15 and 50 nm, were used.

2.2.4. Selectivity tests and real samples analysis

The optimized method was tested for possible interferents, mainly other antibiotics (AMX, PEN V, PEN G, OXA, CFX, GEN), but also other drugs, like APAP and AA, by testing the signal of VAN in mixture solutions.

The method was also tested on real samples, more precisely commercially available human serum. The samples were spiked with different concentrations of VAN. Before the analysis, a volume of 1 mL of the spiked and of the unspiked samples was treated with 50 μL $HClO_4$ 70% and centrifuged at 10000 rpm, for 10 min, for protein precipitation. After that, the supernatant was diluted at 1:10 with 0.1 M H_2SO_4 and tested.

2.3. Results and discussion

2.3.1. Vancomycin interaction with Au and Au nanostructures

2.3.1.1. Electrochemical studies

Tests were carried out, using CV, on AuNPs-SPE and on C-SPE and G-SPE, modified in the lab with AuNS (AuNS-C-SPE and AuNS-G-SPE), electrochemically generated using CV from a solution of $HAuCl_4$. For all three surfaces a single well-defined reduction peak, around +0.5 V, could be observed for the blank solution.

When the VAN containing solutions were tested a clear shift around 0.2 V could be observed on all three surfaces for the peak at +0.5 V, which moved around +0.7 V. Alongside this shift a substantial decrease in the peak intensity was observed. In the oxidation, a peak at around +0.9 V was also observed due to the electrooxidation of VAN (**Fig. 13**). These tests revealed that there is an interaction between the Au and VAN, considering the electrooxidation of VAN, catalyzed by Au but also in reduction where the peak caused by the electroactive forms of Au present on the electrode surface is affected by the possible interactions between Au-VAN, which hinder the reduction electrochemical signal of the Au forms. This interaction is further favorized by the graphene-modified electrode surface, which increases the adsorption of VAN onto the sensing surface.

Considering that in oxidation, on the AuNS-G-SPE, no peak was observed for the blank solution and for the VAN solution, the highest intensity was obtained on AuNS-G-SPE, this surface proved to be the more suitable one. Also, in reduction, the most important decrease in the intensity of the peak was observed for the AuNS-G-SPE.

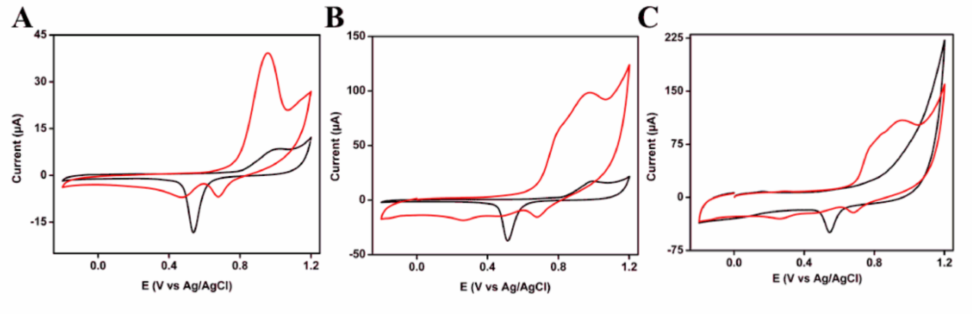

Fig. 13. CVs of 1 mM VAN (**red**) in 0.1 M H_2SO_4 and the blank (**black**) solutions at AuNPs-SPE **(A)**, at AuNSs-C-SPE (electrogenerated) **(B)** and at AuNSs-G-SPE **(C)**; Scan rate 0.1 V s^{-1}.

The CV analysis revealed a more intense electrochemical signal for the interaction VAN-Au, in the case of C-SPE electrochemically modified with AuNSs (AuNSs-C-SPE), compared to the AuNPs-SPE, modified with AuNPs by the manufacturer. This proved that the “homemade” modification, provided a more sensitive platform. Another advantage of the “homemade” modification was the ability to better control the modification of the surface.

Taking into consideration the special properties of graphene, in general, but also as a working surface in electrochemistry, the modification of the surface of a G-SPE with AuNS was also performed. This direction was also supported by previously reported data[90], which revealed that graphene is a more sensitive electrochemical platform for VAN detection and by the data found in the literature[183]. Also, there is additional data that suggests that VAN shows a good affinity towards graphene, graphene being used in the procedures for the VAN extraction[189,190].

The experiments confirmed the theoretical assumptions showing a similar electrochemical response on both electrodes (AuNS-G-SPE and AuNS-C-SPE), but with both a higher oxidation peak and a bigger difference in intensity between the peak of the blank and the peak of the VAN solution, in reduction, on the AuNS-G-SPE.

2.3.1.2. UV-VIS studies

Besides the electrochemical tests, spectrophotometric studies were carried out to investigate the interaction between VAN and different species of Au and different AuNSs, in aqueous solutions. For this the UV-Vis spectra of VAN and mixtures of VAN and $HAuCl_4$ or AuNPs of different size (15 and 50 nm) were recorded.

As it can be seen in **Fig. 14** no changes in the spectra were observed for the mixture of VAN and $HAuCl_4$ in fresh solutions, compared to the monocomponent solutions. However, the appearance of a new, smaller peak at around 450 nm, after 4h, revealed the presence of AuNP, caused by the chemical interaction between VAN and $HAuCl_4$. This data suggested that there is indeed an interaction between VAN and $HAuCl_4$, but which in our working conditions will require a longer period to lead to the formation of detectable VAN-AuNPs aggregates.

When the mixture of VAN and citrate stabilized AuNPs were tested, for the fresh solutions, small changes intensified after 4h were observed, indicating the interaction between VAN and AuNPs. The changes were similar for both types of AuNPs, of 15 nm and 50 nm diameter. The changes consisted mostly of a bathochromic shift, indicating the possible formation of VAN-AuNP aggregates, larger in dimensions. These findings confirmed the electrochemical data obtained regarding the VAN-Au interaction.

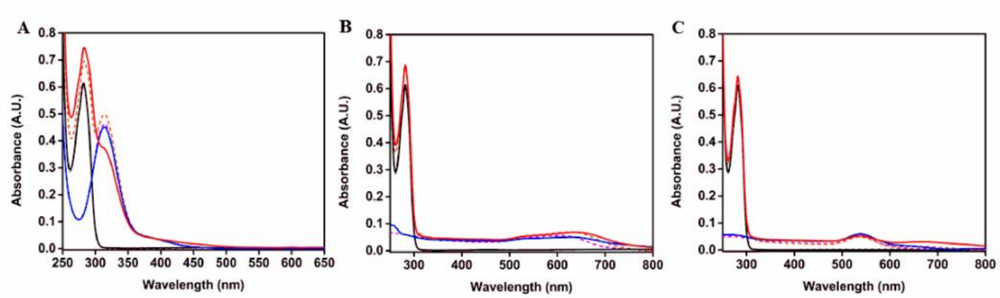

Fig. 14. UV-VIS spectra, fresh solutions and after 4h, of VAN 0.1 mM (**dotted grey** and **black**), of Au species (**(A)** $HAuCl_4$ 0.1 mM, **(B)** AuNPs 50 nm and **(C)** AuNPs 15 nm) (**dotted pink** and **blue**) and of mixture of VAN 0.1 mM and Au species Au species (**(A)** $HAuCl_4$ 0.1 mM, **(B)** AuNPs 50 nm and **(C)** AuNPs 15 nm) (**dotted orange** and **red**).

2.3.2. Optimization of the modification with Au nanostructures

Two different approaches of modifying the G-SPEs were investigated after G-SPEs were established as the best analytical platform. The two approaches were tested to obtain the conditions which lead to a large, well-defined anodic peak for VAN and to the highest, quantifiable difference between the cathodic peak of the blank and in the presence of VAN. The first approach involved the electrogeneration of the AuNSs, using two different techniques, CV, and CA. The second approach involved the modification with already synthesized AuNPs, of two different sizes, 15 and 50 nm, through drop-casting.

From the data obtained (**Fig. 15**), the protocol involving the electrogeneration through CA proved to be the best strategy, showing a higher sensitivity towards VAN, considering both domains, in oxidation and reduction (blue line, **Fig. 15A, C**). It could be observed that the sensing surfaces modified through electrogeneration with AuNS were more sensitive towards VAN in reduction compared to the surfaces modified with already synthesized AuNPs, through drop-casting. This can be explained by the higher reactivity of the AuNS obtained in situ, electrochemically, which are not modified on the surfaces with stabilizing anions like citrate, resulting in stronger interactions with VAN. The VAN molecules interact,most probably, through physisorption with the modified surface of the electrode. Also, it can be observed in **Fig. 15A, C** that they present a stronger signal in reduction when the blank solution is tested, due to their higher electrochemical reactivity.

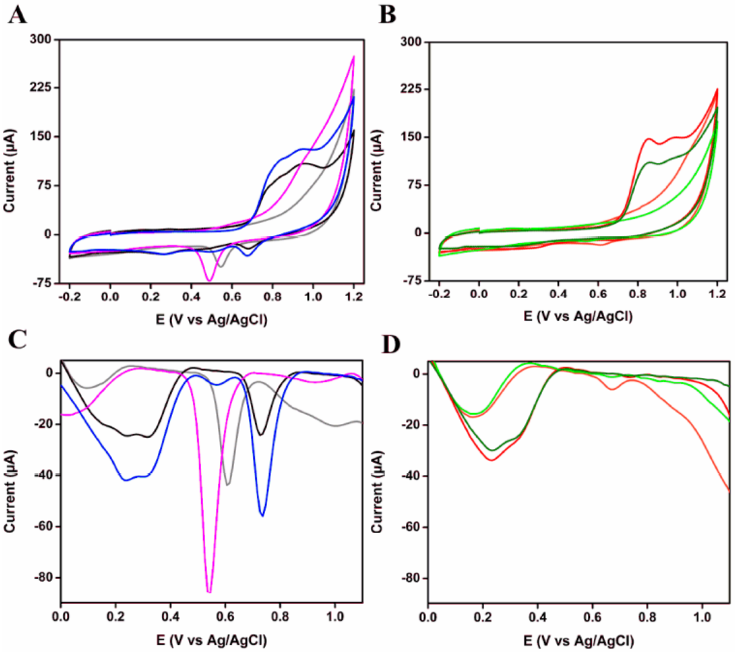

Fig. 15. (**A**) CVs and (**C**) DPVs of 1 mM VAN in 0.1 M H_2SO_4 and the blank solutions at CV–AuNS–G–SPE (**black** and **grey**) and CA–AuNS–G–SPE (**blue** and **pink**); (**B**) CVs and (**D**) DPVs of 1 mM VAN in 0.1 M H_2SO_4 and the blank solutions at AuNP 15 nm G–SPE (**red** and **orange**) and AuNP 50 nm G–SPE (**dark green** and **light green**).

In oxidation, the electrode modified with 15 nm AuNPs presented an anodic peak for VAN with a peak current a little bigger than the one obtained for the electrode modified with 50 nm AuNPs.

Similarly, a larger anodic peak was obtained for the electrode modified through CA, compared to CV. Even though in oxidation it seemed that the electrodes modified through drop-casting gave slightly better results, considering their worse results in reduction, 10 nA difference compared to 28 nA difference for the electrogenerated AuNSs, the electrogeneration protocol looked to be the more suitable approach overall.

Considering all these, we have chosen to continue the sensing platform obtained through electrogeneration by using CA.

The potential used for the electrogeneration of AuNS was also optimized (**Table I**). For the optimization of this parameter, a balance between the signal in the two approaches in oxidation and reduction was considered. For this, both (i) a well-defined peak, clearly distinguishable from the signal of the blank, in oxidation and (ii) the biggest difference between the signals of AuNSs in the blank and the presence of VAN (**I_B-I_{VAN}**), in reduction, were chosen as selection criteria.

Table I. Optimization of the electrogeneration procedure

Deposition Potential Optimization				
	Reduction			**Oxidation**
Deposition Potential (V)	**Response Intensity (µA)**			**Response Intensity (µA)**
	Blank	**50 µM VAN**	**I_B-I_{VAN}**	**50 µM VAN**
−0.5	−94.14	−55.30	−38.84	43.87
−0.4	−89.04	−48.89	−40.13	45.43
−0.3	−77.67	−40.92	−36.75	42.35
−0.2	−66.84	−42.21	−24.63	40.90
−0.1	−51.45	−46.8	−4.65	37.16
0	−36.57	−42.59	6.02	32.92

I_B – Intensity obtained for blank solutions; I_{VAN} – Intensity in the presence of VAN

Several potentials from -0.5 V up to 0 V were tested. The experiments showed an increase in the sensitivity with the decrease of the potential applied down to around -0.4 V. No significant improvement was observed at lower potentials and at higher potentials; a decrease in the response and even a change in the behavior were observed around 0 V, concluding that a potential of - 0.4 V is the optimal one for the electrogeneration of AuNSs.

2.3.3. Analytical performance

2.3.2.1. Calibration curves

Two calibration curves were realized, for each redox domain of detection, in the range of concentrations from 1 µM to 100 µM VAN (**Fig. 16**). The linear relationships found, with their correlated equations and their correlation coefficients (R^2), were as it follows: I_{VAN} (µA) = 0.7689 × C_{VAN} (µM) - 0.0332; with R^2= 0.9873, for the oxidation domain and, I_B - I_{VAN} (µA)= −0.3782 × C_{VAN} (µM) – 18.791; with R^2=0.9713, for the reduction domain.

For the determination of the LOD the following equation was used: LOD = 3·Sb/m, in which Sb is the standard deviation of the response of the blank solution and m is the slope of the calibration curve. LODs of 0.29 µM and 0.5 µM were calculated for the oxidation domain and the reduction domain, respectively.

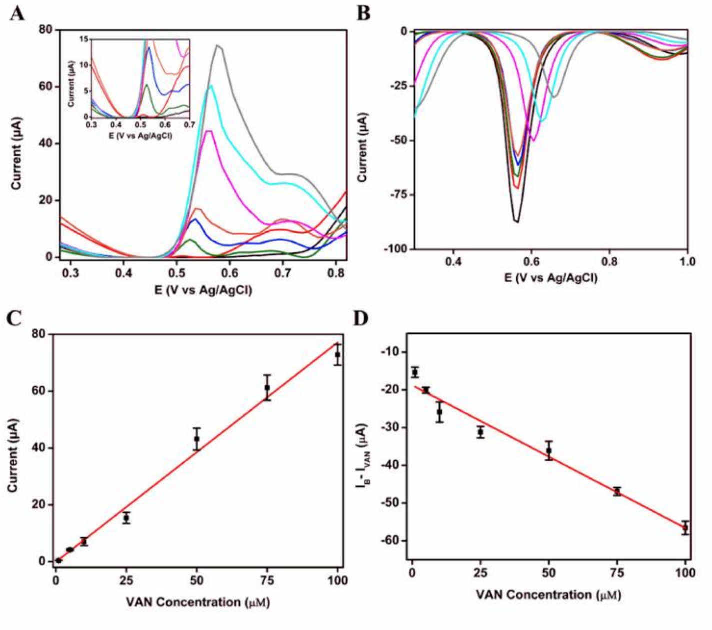

Fig. 16. (First row) DPVs in oxidation **(A)** and in reduction **(B)**, at AuNS-G-SPE, of **1 µM**, **5 µM**, **10 µM**, **25 µM**, **50 µM**, **75 µM** and **100 µM** VAN solution in 0.1 M H_2SO_4 (**blank**) (Inset **(A)** – zoomed area); (Second row) Linear relationship between the response in oxidation **(C)** and the response in reduction **(D)** for VAN concentration from 1 to 100 µM.

2.3.2.2. Selectivity studies and real sample analysis

The selectivity of the method was tested by recording the signal of VAN in mixture solutions, with other antibiotics and drugs. Both approaches proved to be selective towards VAN, its signal not being significantly affected by the presence of the tested interferents (**Fig. 17**).

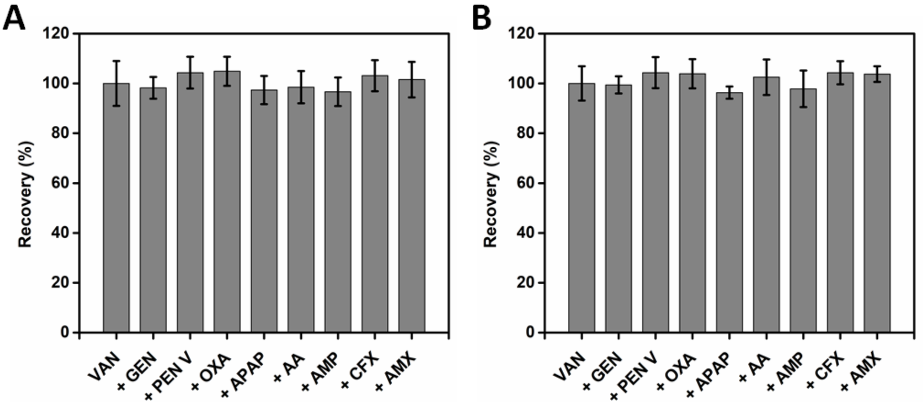

Fig. 17. Selectivity tests using the optimized method for direct approach in oxidation (**A**) and for the indirect approach in reduction (**B**).

The developed method was used for the analysis of real samples, consisting of commercially available human serum spiked with VAN (**Fig. 18**). The concentration of VAN in the tested samples was determined using the standard addition method. Recoveries of 97.38% and 104.54% in oxidation and of 107.06% and of 103.70% in reduction were obtained for both approaches after a minimal sample treatment.

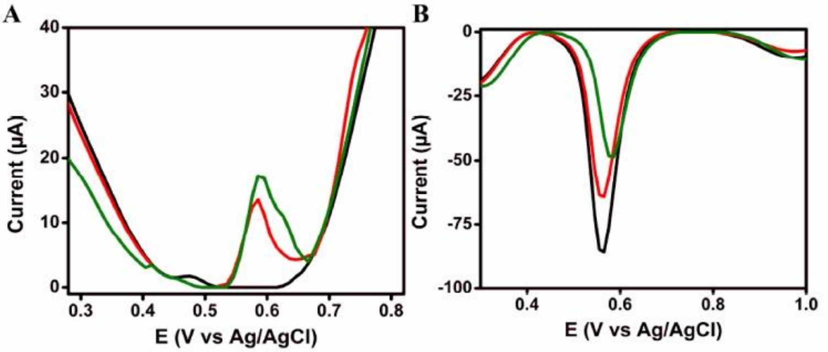

Fig. 18. Real sample analysis: (**A**) in oxidation and (**B**) in reduction of blank diluted serum (**black**) and diluted serum spiked with 10 µM (**red**) and 50 µM (**green**) final concentrations of VAN.

2.4. Conclusions

A selective method was developed for the electrochemical analysis of VAN, based on a C-SPE modified with a hybrid graphene–Au nanocomposite with two different detection approaches in one analysis, one direct using the electrooxidation of VAN, and the other one indirect, based on the intrinsic electrochemical signal of AuNS, in reduction, and their interaction with VAN.

The developed method was able to successfully detect VAN in the linear dynamic range (LDR) of 1 – 100 μM with a LOD of 0.29 μM for the direct approach and 0.5 μM for the indirect one. The selectivity of the method was tested in the presence of other antibiotics and drugs. This method was successfully applied for the detection of VAN from commercial human serum samples.

This study shows the utility of the combination of two different nanomaterials such as graphene and AuNS and how they can be combined in an electroanalytical platform for the sensitive detection of an antibiotic.

Chapter II. The development of biomimetic-based electrochemical sensors for the detection of antibiotics

1. Molecularly imprinted polymer-based sensor for the detection of cefalexin

1.1. Introduction

Cefalexin is an orally active β-lactam antibiotic, belonging to the first generation of cephalosporins and it is effective against Gram-positive bacteria, and, to a limited extent, Gram-negative bacteria[9]. It is frequently used in the treatment of upper respiratory tract infections, pneumonia and uncomplicated urinary tract infections[191].

The BDDE has been used for the quantification of cephalosporins and penicillins[56,57]. Its unique characteristics such as low background and capacitive currents, higher resistance to fouling, wide potential window and high resistance to chemical and physical damaging agents make it a very attractive electroanalytical platform[192]. Nonetheless, a disadvantage of the BDDE is that, for CFX, a decrease of the peak in the presence of other cephalosporins was noticed. A promising alternative to overcome this issue and enhance the selectivity is the use of MIPs as electrode modifiers.

In this context, the objective of this study was the development of a MIP-based electrochemical sensor for the sensitive and selective detection of CFX. Indole-3-acetic acid (I3AA) was chosen as the monomer because it presents functional groups capable to interact with CFX and it can be electropolymerized[193] (**Fig. 19**).

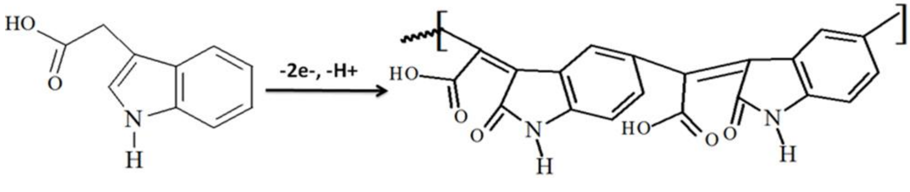

Fig. 19. I3AA structure and the polymerization mechanism (adapted from Prasad *et al.*[193]).

The MIP was obtained through "green chemistry", the electropolymerization of the monomer (I3AA) being performed in an aqueous solution, on a glassy carbon electrode (GCE) or a BDDE in the presence of CFX, as the template molecule. The two electrodes were used in order to assess how different electrode materials and structures translate to the performance of the MIP sensor. Due to its wide electrochemical potential window, the BDDE allowed also to assess the influence on the MIP sensor of the high potential applied during the electrogeneration of the MIP and implicitly, of the overoxidation of the MIP film.

1.2. Experimental

1.2.1. Chemicals, instrumentations, and electrochemical measurements

All reagents were of analytical grade and were used as received. CFX monohydrate, CFTXO sodium salt, CFD monohydrate, CFTX sodium salt, CFC monohydrate, CFOX sodium salt, CFTZ pentahydrate were provided by Antibiotice SA (Iasi, Romania). AMP trihydrate monosodium, HCl, Na_2HPO_4, NaH_2PO_4, NaCl, I3AA were purchased from Merck; $K_4[Fe(CN)_6]$, $K_3[Fe(CN)_6]$, and methanol from Sigma-Aldrich (St. Louis, MO, USA), phosphoric acid, APAP and AA were purchased from Merck (Whitehouse Station, NJ, USA). Capsules containing 500 mg CFX (Cefalexina Atb® (Antibiotice SA)) and Somes River water collected near Cluj-Napoca, Romania were used for real samples analysis.

The electrochemical experiments were performed with an AUTOLAB PGSTAT 302N (EcoChemie, Utrecht, The Netherlands) equipped with the NOVA 1.10.4 software. The BDDE (3 mm diameter, with approximately 0.1% boron content) was purchased from Windsor Scientific (Slough Berkshire, UK), the GCE from BAS Inc. (West Lafayette, IN, USA) and they were used as working electrodes in the conventional three-electrode cell, in static mode, along with Ag/AgCl KCl 3 M as reference electrode and a Pt wire as counter electrode, which were obtained from BAS Inc. (West Lafayette, IN, USA).

Before each analysis, the BDDE and the GCE were polished using a 0.05 μm alumina suspension and polishing cloth, followed by an intense rinsing step using ultrapure water. The electrochemical cell contained 5 mL of supporting electrolyte and for the characterization steps; the exact concentration of the redox probe was added to the supporting electrolyte solution. For the polymerization procedure, the same volume of supporting electrolyte solution was used containing the mentioned concentrations of monomer and template, for MIP fabrication, and only the mentioned concentration of monomer for the non-molecularly imprinted polymer (NIP) fabrication. All electrochemical measurements were performed without the deaeration of the solution. The main electrochemical techniques employed in this study were CV, DPV and electrochemical impedance spectroscopy (EIS).

The CV technique was used for the polymerization procedure. The CV parameters for the polymerization procedure were a potential window between -1.6 to +1.6 V vs. Ag/AgCl, for the BDDE and between -1.0 V to +1.2 V vs. Ag/AgCl for the GCE, with a scan rate of 0.1 V·s^{-1}, for both electrodes. The number of cycles was optimized, varying between 2 and 10 cycles, with 5 cycles giving the best results.

The EIS and DPV techniques were used to assess the response of the unmodified electrode and the modified one, after each step, DPV being also used for CFX quantification. EIS, which is used in the optimization part, is a sensitive technique, very useful for surface characterization, but also with a longer duration of the procedure and with more complex technical requirements. Thus, for the quantitative analyses, DPV was employed, representing the optimal procedure considering sensitivity, reproducibility, time of analysis and accessibility.

For the DPV technique, the values of the main parameters of the method, represented by the pulse height, the pulse width, and the scan rate, were as it follows: a potential window between +0.55 V to -0.30 V vs. Ag/AgCl, a scan rate of 0.02 V s^{-1}, a pulse height of -0.1 V and a pulse width of 50 ms. The DPV in reduction was used, to observe the reduction peak of the chosen redox probe, due to the lower probability of interferences in this approach. EIS measurements were carried out in the presence of 10 mM $[Fe(CN)_6]^{3-/4-}$ in PBS (20 mM, pH 7.4) as redox probe, the impedance being measured in a frequency range of 0.01 and 100,000 Hz using the open circuit potential.

1.2.2. Construction of the MIP-based sensor and analysis procedure

The MIP formation was achieved by immersing the working electrode in 20 mM PBS, pH 7.2 containing the corresponding amount of the monomer (I3AA) and the template (CFX). Theelectropolymerization procedure was performed as previously reported[193]: CV in a potential window between -1.6 to +1.6 V vs. Ag/AgCl, for the BDDE and between -1.0 V to +1.2 V vs. Ag/AgCl for the GCE, with a scan rate of 0.1 V·s^{-1}, for both electrodes. Different concentrations of monomer and template and different ratios between them were tested. The studied concentrations of the monomer were 0.1, 1 and 5 mM. The following concentrations of the template were measured 0.01, 0.05, 0.1, 0.5 and 1 mM. The resulting tested ratios were (monomer: template): 1:1, 2:1, 20:1 and 100:1. Also, included in this step, three different values for the number of cycles for the CV procedure were examined: 2, 5 and 10. The same procedure was used for the formation of the NIP, except the polymerization solution did not contain the template (CFX).

The removal of the CFX (template) from the MIP film was performed by keeping immersed the modified electrode in an exact volume of 2 mL of the corresponding solvent or solution (methanol, NaOH 0.1 M and PBS), in identical cells, under a constant stirring, at a speed of 7000 rpm, achieved with identical magnetic bars (stirrers), at room temperature, for 5, 15, 30 and 60 min.

After the generation of the MIP film and extraction of the template, the electrode modified with MIP was immersed in PBS containing 10 mM $[Fe(CN)_6]^{3-}$ and DPV analysis was performed, recording the I_e current. After electrode rinsing with 10 mL of ultrapure water, the electrode was kept in 2 mL of solutions of different concentrations of CFX, prepared in ultrapure water or PBS, under a constant stirring, at a speed of 7000 rpm, at room temperature for 5, 15, 30 and 60 min. Subsequently, the electrode was rinsed and it was immersed in PBS containing 10 mM $[Fe(CN)_6]^{3-}$ and DPV analysis was performed, recording the I_C current. In the end, the signal after incubation (S_{incub}) was calculated as $S_{incub} = (I_e - I)/I_e$. The signal obtained for the extraction procedure (S_{extr}) was calculated as $S_{extr} = (I_e - I_0)/I_0$, where I_0 was the current registered in DPV after the polymerization procedure.

Each time the electrode (GCE or BDDE) was immersed in a different solution during the sensor fabrication (polymerization, extraction, incubation and after each characterization procedure) the working surface was thoroughly rinsed with exact 10 mL of ultrapure water using each time the same procedure. This was done in order to assure the complete removal of any unwanted residues from the previous step, to prevent the contamination of the solutions and to achieve a better reproducibility. The study focused on the use in parallel of two different working surfaces represented by two different types of electrodes, GCE and BDDE. All the mentioned steps and procedures were carried on using both, according to the specified conditions.

1.2.3. Surface characterization measurements

Atomic force microscopy (AFM) measurements were performed using an NTEGRA Spectra platform (NT-MDT, Russia), in intermittent contact mode, under ambient conditions, with 1 Hz scan frequency, and 512 x 512 scan points. We used standard silicon probes HQ-NSC15/Al BS (MikroMasch) with a typical force constant of 40 Nm^{-1}, typical resonance frequency of the cantilever of 325 kHz, and tip radius less than 10 nm. AFM data processing was performed with the integrated software Nova v1.1.0.1837 (NT-MDT). Scanning electron microscopy (SEM) analysis was performed with a UHR Scanning Electron Microscope model SU8230 (Hitachi, Japan). The samples were sputtered with gold (7 nm) before analysis.

1.2.4. Selectivity studies and real sample analysis

For the selectivity studies, the rebinding step was performed in 500 nM solutions containing AMP, CFD, CFTXO, CFTX, CFC, CFOX, CFTZ, GEN, VAN, AA, APAP.

For the analysis of the environmental samples, CFX was added to untreated river water to obtain a 5 mM solution. This solution was further diluted with the same untreated river water in order to obtain a 100 nM solution, which was analyzed using the developed MIP-sensor. To this solution standard solution of cephalexin in ultrapure water was added to obtain 200 nM, 300 nM, 400 nM spiked river water. The concentration of CFX was determined by the standard addition method (n = 3).

For the analysis of the pharmaceutical samples, the content of five capsules of Cefalexina Atb® (Antibiotice SA) containing 500 mg/capsule were fine grounded and using the declared concentration, the accurately weighted quantity of powder corresponding to 5 mM CFX was dissolved in ultrapure water. After 40 min of sonication, 100 µL of the supernatant was diluted with ultrapure water to a volume of 5 mL, to obtain a concentration of 0.1 mM CFX. This was further diluted to obtain a final concentration of 100 nM, which was used for tests. Next, the same procedure was applied as in the case of river water.

1.3. Results and discussion

1.3.1. Elaboration of the sensor

1.3.1.1. Electropolymerization of the I3AA

The modification of the GCE and of the BDDE with MIP film was performed by the electropolymerization of the I3AA in aqueous medium, using a procedure comprised of multiple CV cycles in PBS (pH = 7.4) that contained the monomer and the template (**Fig. 19**). The applied potential range was adapted to the electrode material: in the case of the GCE, the potential was scanned between −1.0 V and +1.2 V vs. Ag/AgCl, while in the case of the BDDE between −1.6 to +1.6 V vs. Ag/AgCl, due to the wide potential window and high mechanical and chemical stability of the BDDE. Similarly, in order to obtain the NIP film, the same procedure was applied, but in PBS containing only the monomer.

In **Fig. 20**, a well-defined oxidation peak is observed at around 0.8 V on both electrode materials, corresponding to the anodic oxidation of the I3AA. This peak decreases from the second to the fifth scan, suggesting the formation at the surface of the electrode of an insulating film. In the case of the BDDE, a small peak is obtained in the first scan at around 1.5 V, corresponding to the anodic oxidation of CFX, as previously reported[56]. Similar voltammograms were obtained in the case of electro-generating the NIP film (data not shown).

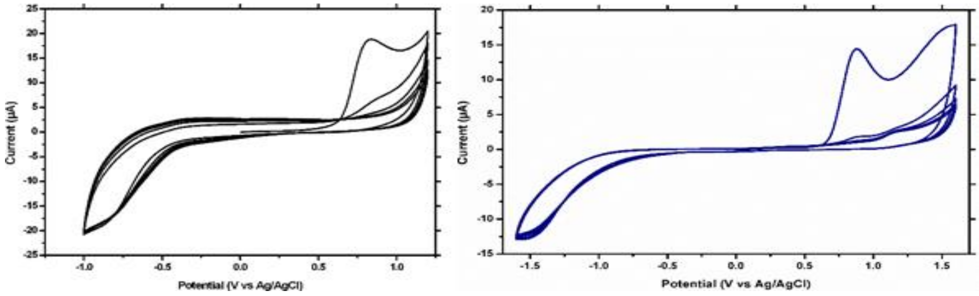

Fig. 20. CVs for MIP formation on the GCE (**left**) and on the BDDE (**right**).

The proposed mechanism for the formation of the MIP film involves the electro-oxidation of I3AA involving the loss of $2e^-$ and $1H^+$, with the oxidation product 3-methylenindolenine carboxylic acid, which further undergoes step-wise electropolymerization[193].

1.3.1.2. Interaction mechanism between the MIP film and CFX

Considering the structure of CFX and of the MIP film, multiple interactions can be imagined between the template and the polymer: H bonds, electrostatic interactions, π-π stacking, all contributing to the selective rebinding of CFX (**Fig. 21**).

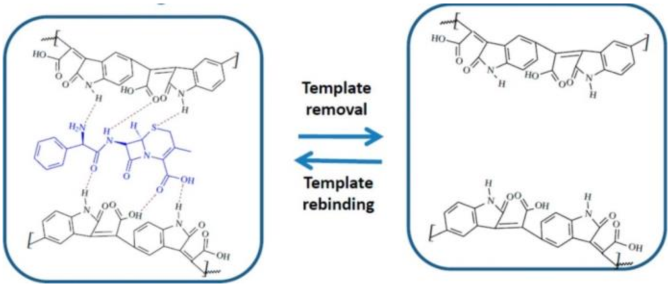

Fig. 21. The possible interaction sites between the MIP film and CFX.

1.3.2. Electrode Characterization

1.3.2.1. Electrochemical Characterization

Electrochemical measurements were carried out to characterize the modified electrodes at different stages of the fabrication of the MIP-sensor. Using the DPV technique to measure the signal caused by the reduction of the $[Fe(CN)_6]^{3-}$, a high peak current was observed for the unmodified electrode (**Fig. 22A, a**), which was severely decreased after polymerization (**Fig. 22A, b**).

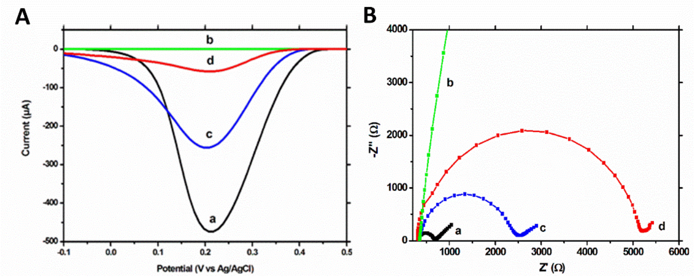

Fig. 22. (**A**) DPV voltammograms on the BDDE in 10 mM $[Fe(CN)_6]^{3-}$, in 0.02 M PBS on: (a) the unmodified electrode, (b) after electropolymerization, (c) after template removal (incubation for 30 min, under stirring, in NaOH 0.1 M solution) and (d) after rebinding of CFX (incubation for 30 min, under stirring, in 1 µM CFX solution). (**B**) EIS spectra (50 frequencies) on the BDDE in 10 mM $[Fe(CN)_6]^{3-}/[Fe(CN)_6]^{4-}$ in 0.02 M PBS, on: (a) the unmodified electrode, (b) after electropolymerization, (c) after template removal (incubation for 30 min, under stirring, in NaOH 0.1 M solution) and (d) after rebinding of CFX (incubation for 30 min, under stirring, in 1 µM CFX solution).

After the extraction procedure, the intensity of the peak current significantly increased (**Fig. 22A, c**), although not reaching the intensity obtained for the unmodified surface. This difference between the signal for the unmodified electrode and for the MIP-modified electrode, after extraction, indicates that the extraction procedure removed only the template molecules, decreasing the insulating properties of the MIP film, but not removing the film in its entirety, the extracted imprinted film retaining, although to a lesser degree, its insulating properties. After the incubation with CFX, a reduction in the peak current was once again observed (**Fig. 22A, d)**. This can be explained by the fact that a large percentage of the imprinted cavities are reoccupied during the incubation process.

The EIS tests showed a similar behavior. In the Nyquist plots, the semicircle portion, at higher frequencies, corresponds to the electron transfer limited process, and the linear portion, at lower frequencies, may be ascribed to diffusion. Thus, the diameter of the semicircle equals to the charge transfer resistance (R_{ct}), which is correlated with the dielectric and insulating features of the electrode/electrolyte interface, mainly, in our case, of the modifying film. For the unmodified electrode, a low value of R_{ct} was obtained (**Fig. 22B, a**), but after polymerization (**Fig. 22B, b**), this value increased drastically, confirming once again the strong insulating properties of the polymeric film. After extraction, a decrease of the R_{et} was observed (**Fig. 22B, c**), but the response did not reach the values of the unmodified electrode, showing once again the persistence of the imprinted film on the working surface. The capacity of the MIP to rebind the CFX molecule was proven by the increase of the R_{ct} after the incubation step (**Fig. 22B, d**).

All these results demonstrate the modification of the electrode with a MIP film, the successful extraction of the template and the capacity of the MIP to recapture the analyte molecules. They also show that by removing the template and making available the imprinted cavities, the polymeric film increases its porosity and decreases its insulating properties, the unoccupied cavities allowing an easier electron transfer between the redox probe and the electrode, and these changes can be quantified using the signal of the redox probe.

1.3.2.2. Surface Characterization

SEM images at higher magnification (100 k×) were used to get an insight into the surface morphology of NIP (**Fig. 23A**) and MIP (**Fig. 23B**) films and, more interesting, into the surface of the MIP film after the extraction procedure (**Fig. 23C**).

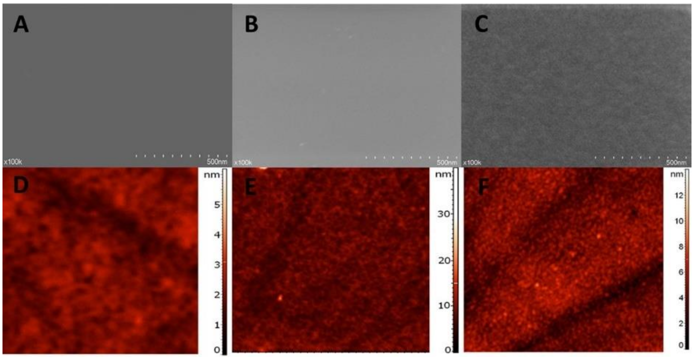

Fig. 23. Surface characterization–SEM images: (**A**) NIP, (**B**) MIP and (**C**) MIP after extraction and AFM images: (**D**) NIP, (**E**) MIP and (**F**) MIP after extraction.

NIP film surface looks compact and smooth. The MIP film, at a first glance seems similar to the NIP surface, but a more porous morphology and some roughness of the surface can be observed. However, the MIP surface after extraction, appears to present an additional change in surface morphology, with a higher degree of roughness, indicating that the extraction procedures of the template molecules lead to a change in the morphology of the MIP film.

In contrast to SEM, which provides a two-dimensional projection or a two-dimensional image of a surface, the main advantage of AFM is the fact that it provides a true three-dimensional profile of the surface. Through AFM is possible to carry out topographic contrast direct height determinations, quantifying the thickness and roughness of the layer.

In the present work, the formation of both NIP and MIP layers was suggested by the AFM images (**Fig. 23D, E**), indicating an elevated layer with the surface height of 3.1 nm for NIP and 15 nm for MIP. The root mean square (RMS) roughness obtained was 0.33 nm for NIP and 0.65 nm for MIP. These results can be explained by the inclusion of the template molecule in the MIP film. CFX, the template, has a more voluminous molecule than the monomer and it does not make covalent bonds with the polymer, likely causing a considerably less structured organization of the polymeric film, promoting an increase in both roughness and thickness of the MIP film.

Similar to the results obtained through SEM, the thickness of the MIP layer after extraction (**Fig. 23F**) was 7 nm and the roughness was 0.95 nm. These data support the hypothesis that the extraction procedure removed partially or totally the template, resulting in the creation of the “imprinted” cavities, which further leads to an increase in roughness. The removal of the template, combined perhaps with the elimination of certain residues remnant from the polymerization procedure and with a certain degree of reorganization of the polymeric film, is the cause of the decrease in thickness of the MIP layer after extraction.

1.3.3. Optimization of the sensor

The development of the MIP-based sensor required several steps and each one needed to be optimized. In the optimization of each parameter, the final signal (the signal difference after the extraction and the incubation step) was considered, because all of the optimized steps influence the final response of the sensor.

The most important part to be optimized is the electropolymerization procedure. Two crucial parameters need to be studied: (i) the composition of the solution used for the polymerization and (ii) the electrochemical procedure used. From the data obtained (**Table II**), a concentration of 1 mM for monomer and of 0.5 mM for template, with a procedure using five cycles, provided the best results in terms of the amount of recaptured analyte.

Table II. Optimization of polymerization (Extraction: NaOH 0.1 M, 30 min; Incubation: 0.5 µM CFX, water, 30 min)

GCE					
Parameter	**Value**	**MIP**		**NIP**	
		S_{extr}	S_{incub}	S_{extr}	S_{incub}
C_{mon} (mM) (C_{temp} = 0.05 mM)	0.1	5.210	0.311	2.425	0.284
	1	4.870	0.358	2.310	0.292
	5	3.920	0.243	1.485	0.287
C_{temp} (mM) (C_{mon} = 1 mM)	0.01	3.460	0.303	2.310	0.292
	0.05	4.870	0.358		
	0.1	6.650	0.398		
	0.5	8.820	0.501		
	1	9.750	0.373		
No of cycles	2	7.240	0.382	2.670	0.294
	5	8.820	0.501	2.310	0.292
	10	6.230	0.238	1.860	0.107
BDDE					
Parameter	**Value**	**MIP**		**NIP**	
		S_{extr}	S_{incub}	S_{extr}	S_{incub}
C_{mon} (mM) (C_{temp} = 0.05 mM)	0.1	6.930	0.327	1.432	0.271
	1	6.340	0.398	1.235	0.257
	5	5.280	0.289	0.845	0.238
C_{temp} (mM) (C_{mon} = 0.05 mM)	0.01	5.670	0.297	1.235	0.257
	0.05	6.340	0.398		
	0.1	7.860	0.475		
	0.5	9.530	0.604		
	1	10.230	0.412		
No of cycles	2	7.830	0.432	1.023	0.246
	5	9.530	0.604	1.235	0.257
	10	8.010	0.367	0.723	0.209

C_{temp} - Concentration template, C_{mon} – Concentration monomer; S_{extr} – Signal obtained after extraction; S_{incub} – Signal obtained after incubation

For the extraction step, the solvent and the duration of the incubation were the main parameters of the procedure that were optimized. Three options were tested as solvents for extraction, based on the solubility of CFX, CFX being highly soluble in MeOH and alkaline aqueous solutions. The best results were obtained using an aqueous solution of NaOH 0.1 M (**Table III**). This can be explained by the fact that the use of a pure non-aqueous solvent as MeOH, affects severely the integrity of the imprinted film, which even though it can cause a better response after extraction, it also affects the binding capacities of the imprinted cavities. Regarding the duration of the procedure, 30 minutes offered enough time for a satisfactory extraction, without any significant damage to the film.

Table III. Optimization of extraction (Polymerization: 1 mM I3AA, 0.5 mM CFX, 5 cycles; Incubation: water, 30 min;)

Solvent	**Time (minutes)**	**GCE**				**BDDE**			
		MIP		**NIP**		**MIP**		**NIP**	
		S_{extr}	S_{incub}	S_{extr}	S_{incub}	S_{extr}	S_{incub}	S_{extr}	S_{incub}
MeOH	5	6.410	0.352	1.813	0.284	7.762	0.415	1.627	0.203
	15	7.560	0.391	2.840	0.312	8.853	0.521	2.154	0.225
	30	9.750	0.448	3.152	0.287	10.236	0.557	3.231	0.248
	60	11.380	0.37	3.750	0.279	12.053	0.456	3.689	0.235
NaOH 0.1M	5	4.510	0.345	1.423	0.289	5.387	0.423	0.926	0.25
	15	6.330	0.404	1.873	0.29	7.325	0.527	1.085	0.253
	30	8.820	0.501	2.310	0.292	9.530	0.604	1.235	0.257
	60	9.280	0.435	2.458	0.283	9.864	0.461	1.367	0.239
PBS, pH 7.4	5	2.320	0.345	0.856	0.285	3.213	0.423	0.763	0.244
	15	4.530	0.404	1.341	0.283	4.345	0.525	0.959	0.248
	30	6.210	0.467	1.557	0.278	5.847	0.585	1.183	0.245
	60	6.850	0.374	1.625	0.277	6.329	0.46	1.348	0.247

S_{extr} - Signal after extraction, S_{incub} – Signal after incubation

For the final step, the incubation with the analyte, similar parameters as for the extraction were optimized. Two solvents were tested, PBS and ultrapure water. Even though PBS yielded slightly better results (**Table IV**), water offered the advantage of bearing more resemblance to the matrix of the targeted samples. Concerning the duration of the incubation, the captured amount of analyte seemed to peak at 30 minutes. Hence, the optimal parameters were chosen for the incubation procedure were water as medium and 30 minutes of incubation.

Table IV. Optimization of incubation (Polymerization: 1 mM I3AA, 0.5 mM CFX, 5 cycles; Extraction: NaOH 0.1 M, 30 min;)

Solvent	**Time (minutes)**	**GCE**		**BDDE**	
		MIP	**NIP**	**MIP**	**NIP**
		Sincub			
Water	5	0.369	0.205	0.435	0.179
	15	0.430	0.237	0.546	0.213
	30	0.501	0.292	0.604	0.257
	60	0.505	0.298	0.609	0.261
PBS, pH 7.4	5	0.372	0.204	0.440	0.205
	15	0.435	0.276	0.553	0.231
	30	0.506	0.293	0.612	0.262
	60	0.508	0.301	0.615	0.265

S_{incub} – Signal after incubation

1.3.4. Analytical parameters of the sensor

1.3.4.1. Calibration Curve

Because the process of rebinding the template can be simulated as an adsorption process, for the MIP surfaces it is required to establish the adsorption isotherm governing the rebinding of the template. The data obtained for our work presented a logarithmic growth, the Freundlich adsorption isotherm, being the one that fitted the best our results. The fact that this empirical equation fitted our data can be explained by the heterogeneity of our imprinted surface, in which characteristics of the Langmuir model, such as a monolayer of adsorbate and equivalency between adsorption sites cannot be fulfilled, the Freundlich model being developed for more irregular and complex surfaces. The unfitted data presented a logarithmic growth of the signal in relation to the concentration of the template, reaching a plateau at higher concentrations, a sign of the fact that all active imprinted cavities have been filled. This type of behavior is characteristic to MIP-based sensors[194–196].

That is why, for the calibrations curves, in order to obtain a linear correlation, the signal was plotted against the negative value of the decimal logarithm of the concentrations, four different calibration curves being constructed, one for each type of modified surface, in the same range of concentrations: 10–1000 nM.

The linear relationships found, with their correlated equations and their correlation coefficients (R^2), were as it follows: for MIP-BDDE, $S_{incub}=-0.1809 \times (-\log(C)\ (M)) + 1.7392$; with $R^2 = 0.9066$, for NIP-BDDE, $S_{incub} = -0.05566 \times (-\log(C)\ (M)) + 0.62457$; with $R^2 = 0.9343$, for MIP-GCE, $S_{incub} =-0.1483 \times (-\log(C)\ (M)) + 1.44859$; with $R^2 = 0.9792$ and for NIP-GCE, $S_{incub} = -0.1317 \times (-\log(C)\ (M)) + 1.1615$; with $R^2 = 0.9927$ (**Fig. 24**).

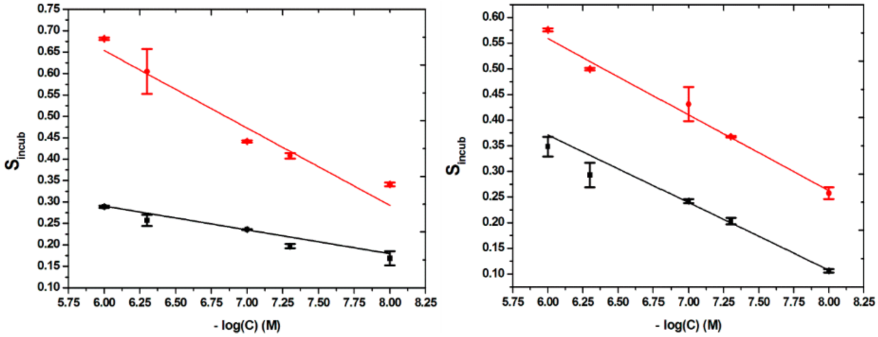

Fig. 24. Linear relationship between MIP-based BDDE (**left**) and GCE (**right**) response (MIP (**red**) and NIP (**black**) and CFX concentration from 10 to 1000 nM).

For the determination of LOD the following equation was used: LOD = $3S_b/m$, in which S_b is the standard deviation of the response of the blank solution and m is the slope of the calibration curve. An LOD of 3.2 nM and 4.9 nM was obtained for the BDDE and the GCE, respectively. These results are better than the one obtained by other electrochemical methods and even instrumental methods, as seen in **Table V.**

From the results presented it can be deduced that the BDDE-modified surface presented better sensitivity, even if you take into account only the MIP signal or the difference in response for the MIP and NIP surfaces. This can be attributed to larger number of imprinted cavities, for the film on the BDDE surface, caused by several factors, such as the larger potential window, the better conducting properties of the BDDE and also to the possibility of a higher incorporation of the template, in the process of its electrooxidation. However, the GCE offered a greater reproducibility and a better correlation for the results, which can also be easily explained by the more homogeneous composition of the GCE surface, compared to the BDDE surface, known for its more heterogeneous nature, which causes some researchers to avoid, it when wanting to develop a biomimetic sensor. Considering all this, it can be said that even though the BDDE offered a slightly greater sensitivity, one should choose the GCE, when wanting to develop a biomimetic platform, because of the very heterogeneous composition of the BDDE surface and slightly less reproducible response, which could affect the performance of the developed analytical platform.

Table V. Comparative analytical performance of different methods for CFX detection

No.	Method of detection	LDR (ng/mL)	LOD (ng/mL)	Real-life samples	Ref.
1	Visualised microarray	8.20 – 68.60	8.20	Milk	[197]
2	MIP for SPEx+ HPLC			Milk	[198]
3	MIP for SPEx-UHPLC–MS/MS		2.24	Milk	[199]
4	Spectrophotometric UV	800.00 – 2800.00	168.00	Pharm. form.	[200]
5	DPV on bare BDDE	173.80-243313.00	34.74	River water, pharm. form., human urine	[56]
6	SWV on heated GCE	208.55-17379.50	52.00	Pharm. form.	[201]
7	HPLC with UV detection	25.00 - 1600.00	10.00	Bovine milk	[191]
8	LC–ESI–MS/MS	2.00 – 100.00	0.50	Pork muscle	[202]
9	Microbiological system	-	128.00	Ovine milk	[203]
10	CV on thin-film BDDE	In the range of mM	-	-	[204]
11	Our MIP-based sensor	3.47 - 347.38	1.11 (BDDE) 1.70 (GCE)	Pharm. form., river water	This work

Pharm. form - pharmaceutical formulations; UHPLC – Ultra high performance liquid performance, SPEx - Solid phase extraction

1.3.4.2. Selectivity Studies

The selectivity of the MIP-based sensor was tested by performing the incubation step in solutions containing other cephalosporins antibiotics (CFD, CFC, CFTXO, CFTX, CFTZ, CFOX), AMP that belongs to the penicillin class, two other antibiotics from different classes (GEN, VAN) and two pharmaceutical compounds intensively used (AA and APAP). The incubation with CFTXO, CFTX, CFTZ or CFOX led to no significant signal modification, because even though these molecules present the common cephalosporin nucleus, they have different substituents, impairing them to be bound in the cavities of the MIP film (**Fig. 25**). In contrast, CFD and CFC (two cephalosporins with a similar and respective identical one side chain to the one of CFX) were bound in the cavities of the MIP, suggesting the importance of the side chain in the fabrication of the MIP film. This is supported by the results obtained after incubation with AMP, penicillin with the side chain identical to the one of CFX and different core nucleus, AMP being bound also by the MIP film.

Because the compounds that are not structurally related to CFX, presented a low affinity for the MIP film fabricated on both electrodes, it can be concluded that the sensor is selective for CFX. Improvements in terms of selectivity are possible, through further future optimization, like the introduction of crosslinkers.

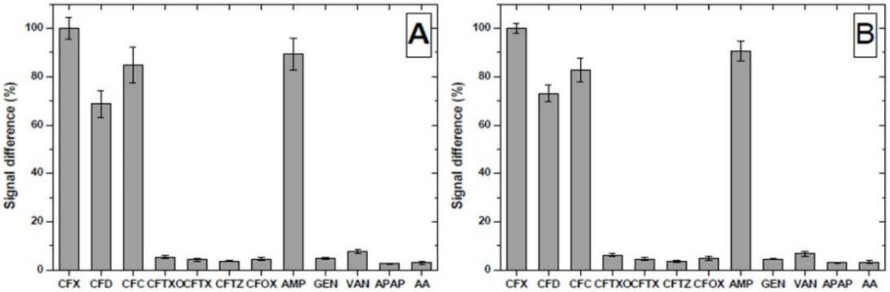

Fig. 25. Selectivity tests using the MIP modified (**A**) BDDE and (**B**) GCE.

1.3.4.3. Real Sample Analysis

The developed MIP-sensor was tested by analyzing two main types of real samples, containing CFX, environmental samples, represented by river water (Someș River, Cluj-Napoca, Romania) and pharmaceutical formulations, represented by capsules (Antibiotice Iași, Romania, 500 mg). The concentration of CFX in the tested samples was determined using the standard addition method. Good recoveries were obtained for both types of samples (**Table VI**) after a minimal samples treatment, this features being a huge advantage for the presented method.

Table VI. The results obtained for real sample analysis

Sample	BDDE			GCE		
	Added -log (C) / M	**Found -log (C)/ M**	**Recovery (%)**	**Added -log (C)/M**	**Found -log (C)/M**	**Recovery (%)**
River water	7	7.50	107.14	7	7.46	106.57
Capsules	7	7.59	108.43	7	6.75	96.43

1.4. Conclusions

A MIP using I3AA as monomer was successfully electro-generated on GCE and BDDE, with the latter leading to better sensitivity. The MIP film was characterized by surface and electrochemical analyses, and it was optimized.

The developed sensors presented good selectivity, with low interferences from other antibiotics and pharmaceutical compounds and very good sensitivity, with a low LOD. The MIP-based sensor was successfully applied for the detection of CFX from pharmaceuticals and river water samples. To the best of our knowledge, this is the first time an MIP-based electrochemical sensor was developed for CFX detection.

2. Aptasensor for oxytetracycline based on innovative Au-based nanostructured platforms

2.1. Introduction

Oxytetracycline, a member of the tetracycline family, is a common antibiotic with a broad range of activity and widely used as both human and veterinary drug in the treatment of various diseases caused by Gram-positive and Gram-negative bacteria and pathogenic Rickettsia[205].

A common strategy in the development of electrochemical aptasensors is the use of classical bare gold electrodes, with a relative flat surface, as a starting platform, which is further functionalized with APTs, *via* S-Au bonds[206]. However, an increasing number of recent studies revealed that nanostructures can enhance interfacial molecular recognition by accelerating the molecular diffusion and reducing steric hindrance[207]. Depending on the architecture of AuNSs, different types can be described: flower-like or spear-like[208], pine-like hyperbranched nanodendrites[209], cauliflower-shaped[210], etc.

The nanostructuring of the electrode surface results in high-curvature electrodes which exhibit higher efficiency for the interaction of the DNA sequence with the target. To explain this increase, two hypotheses have been proposed. The first one stipulates that the nanostructuring provides higher surface areas, allowing for a greater number of probes and hybridization sites. The second suggests that nanostructuring promotes the display and accessibility of probe molecules by increasing their deflection angle which permits for more space between probes and a more efficient APT – target interaction[207,211]. Other extended effects include the large surface area of sharp structures protruding into a solution that can boost interactions between target biomolecules and probes and the accelerated transport of redox reporters *via* radial diffusion at the high-curvature tips of the nanostructures, allowing for amplified electrochemical currents[211]. These properties inspired us to explore the advantages of structured platforms for the development of an electrochemical aptasensor and to investigate how the architectures of the obtained nano- and micro-structures influence the analytical performance of the aptasensors.

In the present work, the development and optimization of a new sensitive, “signal-on” aptasensor for the detection of OXT, using a C-SPE-based platform modified with AuNSs (C-SPE|AuNSs) is described. The nano-/micro-scale morphologies and topographies of the gold structured surfaces were examined by SEM, AFM, X-ray photoelectron spectroscopy (XPS), for better interpretation of the electrochemical behavior.

2.2. Experimental

2.2.1. Materials and instruments

All chemicals were of analytical grade and were used as received without further purification. HCl, NaOH, KCl, NaCl, $MgCl_2$ and 6-mercapto-1-hexanol (MCH) were purchased from Merck (USA); H_2SO_4, $HAuCl_4$, $K_4[Fe(CN)_6]$, $K_3[Fe(CN)_6]$, Tris(hydroxymethyl)aminomethane (TRIS), L-Histidine (His), AMP trihydrate, AMX were purchased from Sigma-Aldrich (USA), OXT and tetracycline (TET) from Alfa Aesar (USA), VAN hydrochloride from Linaris (Germany), and GEN sulphate from BioWorld (USA). A ferrocene (Fc) -labelled thiol-modified APT (ssDNA) (Fc-APT) presenting the following succession of bases: 5′- Fc-GGA-ATT-CGC-TAG-CAC-GTT-GAC-GCT-GGT-GCC-CGG-TTG-TGG-TGC-GAG-TGT-TGT-GTG-GAT-CCG-AGC-TCC-ACG-TG-$(CH_2)_6$-SH-3′, capable of selectively binding the OXT molecules was synthesized by Alpha DNA (Canada).

The APT presents high affinity and specificity to OXT with a K_D of 12.08 nM[212]. All solutions were prepared with UltraPure DNase/RNase-Free distilled water (ThermoFisher, USA). The supporting electrolytes used in this study were 0.1 M KCl and TRIS buffer containing 10.0 mM TRIS, 100.0 mM NaCl, 100.0 mM KCl and 5.0 mM $MgCl_2$, pH 7.2. The lyophilized APT was dissolved in TRIS buffer obtaining a stock solution divided in small aliquots that were kept at − 20°C. Prior use, the APT solutions of desired concentration were freshly prepared by dilution in TRIS buffer and thermally activated by heating the APT solution to 90°C for 5 min, then quickly cooled at − 20°C for 20 s.

The electrochemical experiments were performed using an Autolab PGSTAT 302N (Metrohm Autolab, The Netherlands) equipped with the associated NOVA 1.10.4 software.

The C-SPE and Au-SPE working electrodes, both with a silver pseudoreference and a carbon-based counter electrode were purchased from Metrohm-DropSens (Asturias, Spain). The pH measurements were carried out with a C830 pH-meter (Consort, Belgium).

2.2.2. Electrochemical characterization

For the electrochemical characterization, the obtained platforms were compared with C-SPE, and with the platform aimed to substitute Au-SPE.

Mainly, two electrochemical techniques, CV and EIS, were used for the characterization of the platforms. Both CV and EIS measurements were performed in the presence of 5.0 mM $[Fe(CN)_6]^{3-/4-}$ prepared in 0.1 M KCl as the redox probe. The impedance was measured in a frequency range from 0.01 to 100.000 Hz, for a total number of 50 frequencies, at open circuit potential value. For the indirect CV electrochemical characterization, the potential was cycled between − 0.60 V and + 0.80

V, with a scan rate of 0.1 V/s. These two procedures were also used for the indirect characterization of the platforms after functionalization.

For the direct CV electrochemical characterization, the potential was cycled between − 0.20 V and + 1.50 V in 0.5 M H_2SO_4, with a scan rate of 0.1 $V \cdot s^{-1}$.

For the characterization of the modifications occurred at the surface of the C-SPE|AuNSs platforms (both, during the functionalization and for the quantification of the binding of OXT) CV and DPV were used, by monitoring the anodic signal of the Fc-APT label. For the CV characterization, the potential was cycled between −0.20 V and + 0.50 V, with a scan rate of 0.025 $V \cdot s^{-1}$. The parameters used for the DPV technique were pulse height of 50 mV, pulse width of 40 ms and scan rate of 0.01 $V \cdot s^{-1}$.

2.2.3. Electrodeposition of the Au nanostructures

Several protocols reported in the literature[89,187,208,209,213] were tested for the modification of the C-SPEs with AuNSs. Five protocols were adapted for OXT determination based both on the results obtained during their electrochemical characterization and on the architecture and morphological properties of the AuNSs electrogenerated at C-SPE, revealed by the SEM and AFM studies. The experimental conditions for the development of the five protocols are presented in **Table VII**.

Table VII. Electrodeposition procedures of gold at C-SPEs

Protocol number	Electrochemical deposition procedure	Solution composition	Ref.
Protocol 1 (P_1)	CA, − 0.40 V, 1200 s	5.0 mM $HAuCl_4$ in 0.5 M H_2SO_4	89
Protocol 2 (P_2)	CA, − 0.30 V, 1200 s	10.0 mM $HAuCl_4$ in 0.1 M KCl	208
Protocol 3 (P_3)	CA, 0 V, 600 s	20.0 mM $HAuCl_4$ + 150.0 mM His in 0.5 M H_2SO_4	209
Protocol 4 (P_4)	CP, − 100 µA, 600 s	10.0 mM $HAuCl_4$ in 0.5 M H_2SO_4	213
Protocol 5 (P_5)	MPA, 2 pulses, E_1 = 0.00 V, E_2 = + 0.75 V, $t_1 = t_2$ = 50 ms, total duration = 600 s	10.0 mM $HAuCl_4$ in 0.5 M H_2SO_4	187

CA – chronoamperometry; CP – chronopotentiometry; MPA – multipulse amperometry;

2.2.4. Surface characterization measurements

AFM measurements were performed using a Cypher S AFM (Asylum Research, Santa Barbara, CA, USA), in amplitude modulated AC mode (*aka* tapping mode), under ambient conditions in air. Silicon probes AC160TS-R3 (Olympus), having a rectangular shape silicon cantilever with resonant frequency of 300 kHz, nominal spring constant of 26 N/m, reflex coating Al and tip with nominal radius of 7 nm were used for all the experiments. Several areas of the electrode surface were analyzed. Image processing was performed using the integrated Asylum Research software written within Igor Pro software package (Igor Pro 6, WaveMetrics, Inc., Lake Oswego, USA).

SEM analysis was performed with a scanning electron microscope (GeminiSEM 300; Zeiss) with EHT of 15 kV. The SEM images were recorded using SmartSEM software version 6.05.

The XPS analysis was performed on a ThermoScientific™ ESCALAB™ 250Xi+ X-ray Photoelectron Spectrometer with monochromatic Al Kα, X-Ray source at 1486.6 eV. High resolution spectra were obtained at a perpendicular take off angle. The binding energy (BE) scales were reference by setting the $Au4_{7/2}$ at 84.0 eV. The major adventitious C1s peak (C-C) is measured at 284.5 eV. Two types of scans were carried out in this study: survey scans from 0 to 1344 eV BE and 200 eV pass energy (PE); and high resolution with both 20 eV PE and 200 eV PE for better results interpretation. The XPS spectra and XPS imaging were recorded and fitted using Avantage software. No flood gun was used during XPS data acquisition. Fitting parameters were independently chosen for a consistent fit for all samples in the analyses.

2.2.5. Aptasensor elaboration

For the functionalization of the platforms, two strategies were tested. First one implied the incubation of the C-SPE|AuNSs substrate and of Au-SPE with 40 µl solution of 1.0 µM Fc-APT in TRIS buffer, for a total duration of 2 h. The second one implied the use of MPA for the immobilization of Fc-APT, by applying short alternative potential pulses, of − 0.20 V and of + 0.50 V, both with a duration of 30 ms, for a total duration of 300 ms[66]. For the blocking step with MCH, the same protocol was used as in the Fc-APT immobilization, but with a 100.0 µM MCH solution in TRIS buffer.

2.2.6. Selectivity tests and real samples analysis

The optimized aptasensor was tested for possible interferents, other antibiotics like TET, AMX, AMP, GEN and VAN, by testing the signal for solutions of antibiotics alone and for mixtures 1:1 of interferent and OXT.

Samples of effluent obtained from the Cluj-Napoca Wastewater Treatment Plant (Somes Company, Cluj-Napoca, Romania) were spiked with a solution of OXT in TRIS buffer and passed through a 0.45 µm pore size membrane filter (Chromafil AO-45/25, Macherey-Nagel, Germany) to give a final OXT concentration of 1 µM. Samples were diluted 10 times with the measuring buffer before being analyzed.

Several milk samples were obtained from a local market and were kept at 4°C before analysis. The preparation and sample pretreatment of the spiked milk samples were adapted from previous work from our group[90] and from other studies from literature regarding OXT analysis in milk. The samples were prepared as follows: 10 µl of OXT stock solutions were added to 990 µl of untreated milk and then 50 µl of $HClO_4$ 70 % was used to precipitate the protein and the mixtures were centrifuged for 10 min at 10,000 rpm. 100 µl of the supernatant was diluted with 900 µl of TRIS buffer and this mixture was analyzed.

2.3. Results and discussions

2.3.1. Generation and characterization of the platforms

Optimization of the electrodeposition of gold AuNSs at C-SPE working surface started by screening different protocols from the literature and by varying different parameters such as concentration of $HAuCl_4$ solution, supporting electrolytes, additives, and electrochemical techniques. Hence, the electrode support influence is evaluated as not all procedures were employed at C-SPE in the reported works.

Five protocols were selected, in their optimized state, resulting in the creation of five C-SPE|AuNSs platforms (P_1 – P_5), each one presenting a specific architecture (**Fig. 26**). All five protocols showed good reproducibility and additionally, the reproducibility was monitored online from the recorded signals during deposition, electrodes with too large deviations in response being discarded.

The selected protocols can be considered as representative examples in the electrodeposition of AuNPs/AuNSs. Thus, the optimization of the electrodeposition procedures was performed for all five platforms through electrochemical studies (**Table VIII**).

Protocol P_1 was adapted from our previous work[89] and involved the simple electrodeposition based on the electroreduction of Au^{3+}, through CA. The deposition potential was kept constant (E_{dep} = − 0.40 V), being already a well-established value from other studies[89,214]. However, the concentration of $HAuCl_4$ solution and the deposition time play an important role in the morphology of the resulted gold structures. Therefore, these two were drastically increased to ensure the formation of well-defined Au nanostructures and a good surface coverage.

The second protocol, P_2, was adapted from a study by Shu *et al.* [208] which studied the electrogeneration of AuNSs at GCE through CA using a 10 mM solution of $HAuCl_4$ in 0.1 M KCl. Briefly, P_2 was chosen to evaluate the influence of the supporting electrolyte used during electrodeposition by changing the H_2SO_4 solution from P_1 with KCl.

The third strategy involved the addition of aminoacids to the solution of $HAuCl_4$. Recent studies reported different gold platforms when Au^{3+} solution was mixed with cysteine[214,215] and histidine (His)[209], respectively. Hence, for the P_3 we selected His to be added to the 20 mM $HAuCl_4$ solution and employed CA at 0 V as electrodeposition technique.

Table VIII. The influence of the electrodeposition parameters.

			I_{pa} (µA)	***I_{pc} (µA)***	***Area (mm^2)***	***R_f***
P_1	C_{HAuCl4} (mM)	1	182.56 ± 10.12	-178.36 ± 9.41	31.97	2.54
	t_{dep} = 1200 s	**5**	**205.12 ± 12.56**	**-195.59 ± 14.33**	**83.85**	**6.67**
	E_{dep} = − 0.4 V	10	212.36 ± 11.63	-201.43 ± 11.04	94.61	7.53
	t_{dep} (s)	600	188.33 ± 7.52	-184.59 ± 7.46	54.77	4.36
	C_{HAuCl4} = 5 mM	**1200**	**205.12 ± 12.56**	**-195.59 ± 14.33**	**83.85**	**6.67**
	E_{dep} = − 0.4 V	2400	209.32 ± 15.47	-200.39 ± 8.57	98.80	7.86
P_2	E_{dep} (V)	-0.4	194.48 ± 12.63	-175.13 ± 5.12	138.27	11.00
	C_{HAuCl4} = 10 mM	**-0.3**	**192.62 ± 5.67**	**-172.32 ± 5.64**	133.04	**10.59**
	t_{dep} = 1200 s	-0.2	186.56 ± 7.35	-167.29 ± 7.1	109.32	8.70
		-0.1	177.21 ± 9.21	-154.78 ± 12.5	95.50	7.60
	t_{dep} (s)	600	182.59 ± 14.35	-161.28 ± 8.47	98.27	7.82
	C_{HAuCl4} = 10 mM	**1200**	**192.62 ± 5.67**	**-172.32 ± 5.64**	**133.04**	**10.59**
	E_{dep} = − 0.3 V	2400	195.46 ± 8.65	-176.83 ± 9.88	167.44	13.32
P_3	t_{dep} (s)	300	175.15 ± 6.89	-161.7 ± 7.22	26.53	2.11
		600	**183.58 ± 11.79**	**-170.7 ± 9.57**	**34.06**	**2.71**
	C_{HAuCl4} = 10 mM E_{dep} = 0 V	1200	186.32 ± 11.43	-172.37 ± 7.41	36.96	2.94
P_4	t_{dep} (s)	300	178.51 ± 10.05	-174.34 ± 14.65	60.65	4.83
	C_{HAuCl4} = 10 mM	**600**	**203.43 ± 28.07**	**-191.2 ± 27.53**	**80.98**	**6.44**
	I_{dep} = − 100 µA	1200	207.23 ± 18.96	-195.36 ± 13.44	89.84	7.15
P_5	t_{dep} (s)	300	176.31 ± 7.96	-162.57 ± 9.55	39.47	3.14
	C_{HAuCl4} = 10 mM	**600**	**197.9 ± 18.41**	**-180.47 ± 15.47**	**48.25**	**3.84**
		1200	202.56 ± 16.36	-184.33 ± 11.45	51.46	4.09

*E_{pa} - potential of the anodic peak; I_{pa} – anodic peak current; E_{pc} - potential of the cathodic current; I_{pc} - cathodic peak current; ΔE - potential difference; ΔI_{pa} (%)/ΔI_{pc} (%) - anodic/cathodic peak current increase in comparison to C-SPE; R_{et} - resistance to charge transfer; **ΔR_{et}** – difference of charge transfer resistance between each step in the aptasensor development*

P_4 employs a different electrochemical technique, CP instead of CA. The galvanostatic method employed in our work was adapted from a study by Martínez-Paredes *et al.*[213] which studied the galvanostatic deposition of AuNSs as mean of modifying C-SPE for Pb(II) detection. The last strategy selected (P_5) uses MPA, which is a less employed technique for AuNSs generation. Similar to P_4 the protocol was adapted from a study which aimed to test the influence of the electrodeposition technique used for the modification of GCE with AuNSs on the analytical performance regarding the detection of Hg(II)[187].

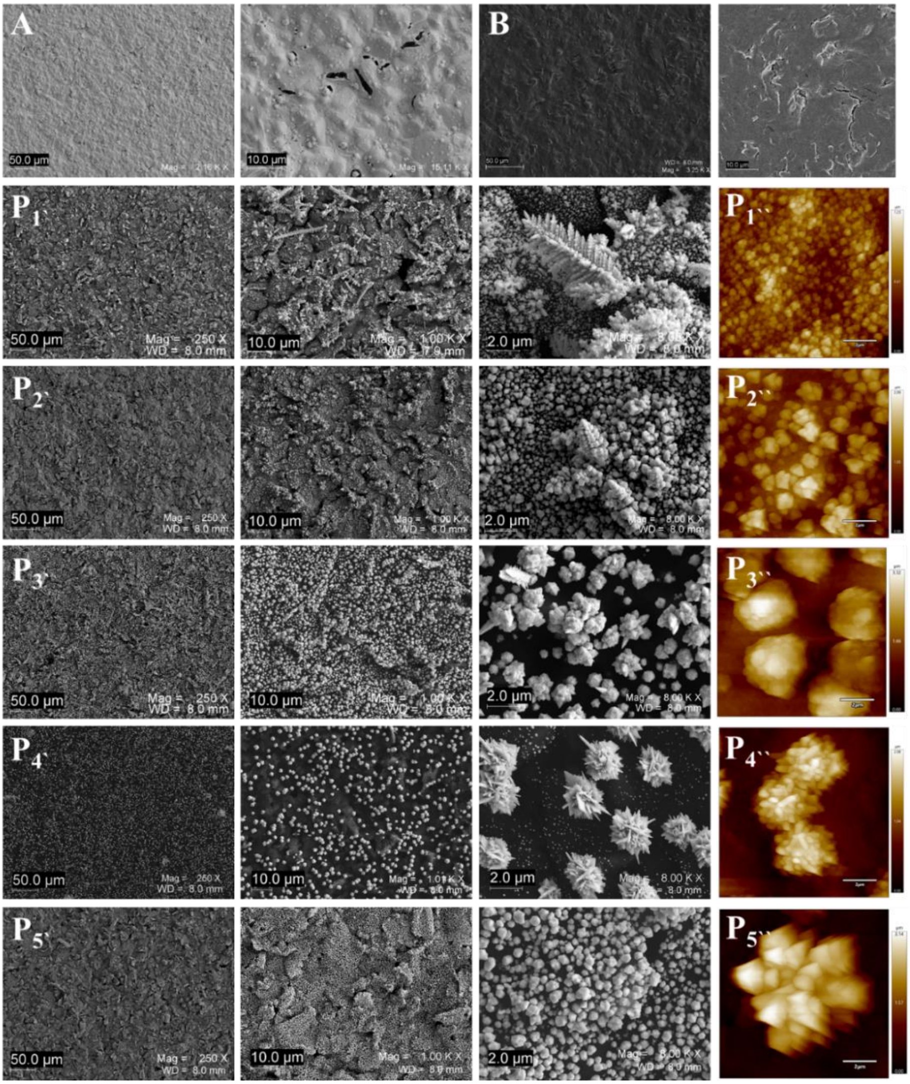

***Fig. 26*. SEM images** of **Au-SPE** (A), **C-SPE** (B) (two magnifications), **P**$_{1`}$ (fern-like structures), **P**$_{2`}$ (spear-like structures), **P**$_{3`}$ (cauliflower-like structures), **P**$_{4`}$ (thistle-like structures) and **P**$_{5`}$ (tetragonal pyramid stuctures) at three magnifications (250x, 1000x, and 8000x) and the corresponding **AFM images: P**$_{1``}$, **P**$_{2``}$, **P**$_{3``}$, **P**$_{4``}$ and **P**$_{5``}$ (AFM scan size 10 µm, scale bar 2 µm).

When considering the electrodeposition of Au, there are two important processes involved: nucleation and growth. Thus, two limiting cases for the coverage of the surface with AuNSs can be distinguished, instantaneous and progressive nucleation. In the case of instantaneous nucleation, the number of nuclei, reaches fast a value that is constant, whereas in the case of progressive nucleation, new nuclei are formed continuously[216,217]. Another aspect is the fact that each AuNS, with a specific larger shape, is practically the conglomeration of numerous nanoscale grains. This means that the formation process follows three phases: (i) the formation of the nuclei, (ii) the aggregation of tiny particles on nuclei and (iii) the growth of each nucleus into crystal grains. These mean that the initial number of formed nuclei is very important, for obtaining AuNSs with specific shape. A large number of initial nuclei can result in a fewer clearly defined AuNSs and in a large number and density of small gold nanoparticles (AuNPs)[216]. Thus, the reaction conditions (including electrochemical technique, electrodeposition potential, $HAuCl_4$ concentration, additives, and electrodeposition time) and the role that they play in the control over the nucleation and directional aggregation gives rise to a non-equilibrium system and thereby favors the formation of AuNSs with specific architectures[216].

The SEM images (**Fig. 26, $\mathbf{P_1}^{`}$-$\mathbf{P_5}^{`}$**) revealed interesting AuNSs with clear distinction in morphology between the different protocols used. AFM images (height data) of the 5 platforms are shown in **Fig. 26, $\mathbf{P_1}^{``}$- $\mathbf{P_5}^{``}$**. The morphologies of surfaces determined by AFM confirmed the presence of SEM features at the electrode surfaces.

The first two protocols resulted in a higher density of NSs but also in a higher heterogeneity both in shape and size (**Fig. 26$\mathbf{P_1}^{`}$** and **26$\mathbf{P_2}^{`}$**). Although NSs with specific shapes could be distinguished as fern-like (**$\mathbf{P_1}^{`}$**) and spear-like (**$\mathbf{P_2}^{`}$**) gold structures, the carbon electrode surface appeared to be cover with relatively smaller, non-specific AuNSs, mostly small AuNPs of 275±49 nm for P_1 (**Fig. 26$\mathbf{P_1}^{``}$)** and about two-times larger, 506±125 nm diameter in the case of $P_2$ (**Fig. 26$\mathbf{P_2}^{``}$**). In these first two cases, the fern-like and spear-like features are too large to be determined by AFM.

These more unorganized arrangements could be explained by the formation of a larger number of Au nucleation centers at the electrode surface in the initial stage of the electrodeposition followed by the growth into specific shapes of the mentioned structures, simultaneously with the formation of additional smaller seed crystals. Although these arrangements could provide augmented Au surface available for bioelement immobilization, one needs to consider the heterogeneity which could lead to highly unorganized arrangement of the immobilized elements of recognition – APTs that might hinder their binding capabilities. Hence, the probability of additional steric hindrance due to the presence of basically two different levels of Au sites onto which both the Apt and the blocking element (MCH) can bind must be considered: (i) one in the proximity of the electrode surface, formed by non-specifically structured gold particles in a relatively homogenous layer, and (ii) another level, further away from the electrode, formed by the ramifications of larger AuNSs.

Hence, when comparing the first two protocols, P_1 and P_2, the influence of the deposition potential and $HAuCl_4$ concentration, apart from the electrolyte used, must be considered. The literature emphasizes the influence of both[216,217]. Although cost-effective, a high concentration of $HAuCl_4$ is needed to ensure Au nuclei formation; however, at a certain threshold, they can become too large and too densely distributed on the electrode surface, inhibiting the formation and growth of organized AuNSs. Also, a similar effect can be obtained by longer electrodeposition time. One practical and cost-effective particularity of our study is the electrode setup employed. Only a small drop (40 μl) of deposition solution at SPEs is needed, which also limits the values of certain parameters like deposition time. Extra lengthy procedures (>30 min) can result in stability problems or the complete deposition of the available Au^{3+}.

In terms of the influence of the deposition potential[167], the more negative value (E_{dep} = − 0.40 V) employed in P_1 combined with a lower concentration (5.0 mM) of $HAuCl_4$ resulted in a larger number of AuNSs and a more defined shape, in comparison with P_2. These mean that the instantaneous nucleation is predominant in the case of P_1, followed by a greater growth of AuNSs, compared to P_2, where the less negative value (E_{dep} = − 0.30 V) of the deposition potential and the higher concentration (10.0 mM) of Au^{3+}, lead to a more pronounced progressive nucleation, resulting in a larger number of nuclei, but in a smaller number of large structures.

Regarding the nature of the electrolyte used for electrodeposition and of the composition of additives, although the influence of the electrolyte and pH are mentioned, the strongest effect on the shape of AuNSs is attributed to the organic additives, like aminoacids, observations that can be seen also in our case for P_3 [209]. The addition of His, in the implementation of P_3, lead to the formation of more organized structures (**Fig. 26P$_{3'}$**) with little presence of additional, smaller particles. The electrode surface (30-50 nm uniformly distributed carbon nanoparticles) presents few 400-850 nm diameter Au clusters, but most of Au structures are larger (cauliflower-like structures), up to 2.1 μm diameter with a density of features at the surface of about 8 clusters/100 μm^2 (**Fig. 26P$_{3''}$**). This might be attributed both to His and the concentration of $HAuCl_4$ solution which was 2-times more concentrated (20.0 mM) than in P_2. Organic additives, like His, can promote the aggregation of the particles and the growth of the clusters, resulting in a smaller number of nuclei, with a drastically decrease in the coverage of the surface, but in more uniform structures, both in terms of size and shape[209,214,215]

The galvanostatic protocol, P_4, resulted in the generation of thistle-like structures (**Fig. 26P$_{4'}$**), relatively large (1.5-2 μm), but more organized, with almost no small distribution of AuNPs, but with lower distribution (3 clusters/100 μm^2) of AuNSs onto the C-SPE surface (**Fig. 26P$_{4''}$**).

The last protocol, involving MPA with short, alternative pulses of different levels of potential, P_5, similarly resulted in relatively organized AuNSs with a large number of nuclei, but with less defined structures. The shape of the AuNSs was less defined, resembling a tetragonal pyramid structure (**Fig. 26P$_{5'}$**), with flat sides and size that can reach up to 3 μm (**Fig. 26P$_{5''}$**), overall presenting less rugosity compared to P_3 and P_4.

Even though the similarity in the pattern of the three protocols (P_3, P_4, P_5), the first two present more organized shapes, analogous to natural ones (thistle and cauliflower) which allow the apparition of more binding sites; therefore, the immobilization of the recognition element may occur in different 3D positions (not necessarily perpendicularly) and also may prevent its "flattening" (i.e. the horizontal disposition of the DNA sequence) and its binding/non-specific adsorption to the surface through other segments than the terminal thiol group. Also, the density of AuNSs and the dispersion in terms of size were higher for P_5 compared to the rest of the protocols.

2.3.2. Electrochemical characterization of the platforms

The platforms were electrochemically characterized, indirectly, using CV and EIS in $[Fe(CN)_6]^{3-/4-}$ redox probe. The experiment revealed an increase in the current intensity in CV (**Fig. 27A**) and a decrease in impedance (**Fig. 27B**), for all C-SPE|AuNSs platforms when compared to the starting surface, C-SPE, although not fully achieving the performance of Au-SPE (**Fig. 27D**). This increase in charge transfer can be attributed mainly to the increase in active surface, due to the resulted three-dimensional, nanostructured platforms obtained by the modification of C-SPE, using several methods.

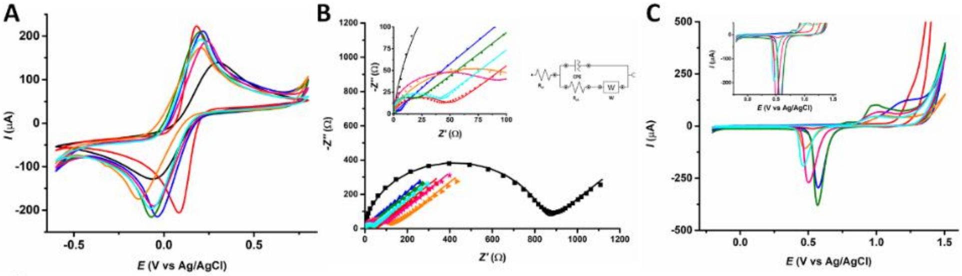

D

Platform	E_{pa} (mV)	I_{pa} (μA)	E_{pc} (mV)	I_{pc} (μA)	ΔI_{pa} (%)	ΔI_{pc} (%)	Q (μC)	RSA (mm^2)	Roughness factor (R_f)
C-SPE	297.85	141.65 ± 10.22	-45.57	-137.94 ± 14.16					
AuSPE	175.78	231.16 ± 17.00	89.52	-226.57 ± 17.71	63.18	64.25	-47.25	12.24	0.97
P_1	214.84	205.12 ± 12.56	-34.18	-195.59 ± 14.33	44.80	41.79	-323.68	83.85	6.67
P_2	202.64	192.62 ± 5.67	-61.04	-172.32 ± 5.64	35.98	24.92	-513.55	133.04	10.59
P_3	234.38	183.58 ± 11.79	-48.83	-170.70 ± 9.57	29.60	23.75	-131.49	34.06	2.71
P_4	197.76	203.43 ± 28.07	-107.42	-191.20 ± 27.53	43.61	38.61	-312.59	80.98	6.44
P_5	205.08	197.90 ± 18.41	-63.48	-180.47 ± 15.47	39.71	30.83	-186.23	48.25	3.84

Fig. 27. **(A)** CVs and **(B)** EIS spectra obtained in 5.0 mM $[Fe(CN)6]^{3-/4-}$ prepared in 0.1 M KCl and **(C)** CVs in 0.5 M H_2SO_4 obtained at C-SPE (**black**), Au-SPE (**red**) , P_1 (**blue**), P_2 (**green**), P_3 (**orange**), P_4 (**pink**), P_5 (**cyan**);**(D)** Electrochemical characterization of C-SPE|AuNSs platforms, E_{pa} - potential of the anodic peak; I_{pa} – anodic peak current; E_{pc} - potential of the cathodic current; I_{pc} - cathodic peak current; ΔI_{pa} (%)/ΔI_{pc} (%) - anodic/cathodic peak current increase in comparison to C-SPE; Q - charge consumed for reducing the Au oxides; RSA - real surface area.

The CV characterization revealed a well-defined redox couple with a peak separation of about 330 mV at bare C-SPE. For the obtained C-SPE|AuNSs platforms, the peak separation decreased to values between 250 and 280 mV, demonstrating the enhancement in charge transfer. The peak separation was about 85 mV for the commercial Au-SPE.

EIS analysis was performed at each developed platform to confirm the results obtained by CV and to evaluate of the interfacial charge transfer processes, which can help with the kinetic characterization of the electrochemical reaction [218]. The EIS data were fitted using the facilities provided by NOVA 1.10.4 software and the simulated values of kinetic parameters were determined after each modification step (**Table IX**).

As it can be seen from **Fig. 27B**, the Nyquist plots are described by a slightly deformed semicircle followed by a straight line at all C-SPE|AuNSs platforms, C-SPE and Au-SPE, respectively. A perfect semicircle is described by the well-know Randles circuit. The slight deformation of the circle can be attributed to the fact that in real systems the double layer at the electrode surface is not completely homogenous. To characterize this non-ideal behavior, the standard Randles circuit is adapted by replacing the ideal capacitor by a constant phase element (CPE) (**Fig. 27B**, inset right). The presence of the diffusion limitations at low frequencies must also be present in the circuit and is represented by a Warburg element (W).

As it can be seen from **Table IX**, the resistance to charge transfer (R_{et}) was around 780 Ω at C-SPE and after electrodeposition dropped to 2 Ω, the lowest (P_1) or down to 130 Ω for P_3, the highest. From the obtained values, it can be observed that there is an acceptable correlation between the CV and EIS results, although the EIS results varied more between platforms.

Table IX. Values of circuit elements obtained by fitting the experimental data obtained for each platform

Platform	R_S (Ω)	R_{et} (Ω)	*W* (mMho)	*CPE* (µMho)	*n*	*C* (µF)	$\chi 2$
C-SPE	140.730	780.980	3.224	1.998	0.941	1.332	0.009
P_1	258.280	1.958	3.099	346.330	0.770	39.174	0.001
P_2	374.015	16.300	3.423	5.510	1.070	10.106	0.002
P_3	496.000	132.000	3.006	14.540	0.814	3.481	0.002
P_4	436.320	85.380	2.908	14.932	0.877	5.864	0.002
P_5	381.445	33.626	3.483	5.592	0.923	2.734	0.001
Au-SPE	27.045	46.973	3.505	7.564	0.826	1.789	0.040

Rs - Solution resistance; R_{et} - resistance to charge transfer; W - Warburg element impedance; CPE - Constant phase element; C – calculated capacitance; χ^2: Goodness of fit

The platforms were also characterized by CV in 0.5 M H_2SO_4 (**Fig. 27C**). By using this protocol, an anodic response starts to appear at around + 1.0 – + 1.1 V, due to the formation of Au oxides[219]. Subsequently, in the reverse potential scan, they are eventually reduced, at about + 0.50 V[219,220]. By integrating the charge consumed for reducing the Au oxides formed in the positive scan, the real surface areas (RSAs) and the roughness factors (R_f) of the electrodes are calculated (**Fig. 27D**) by assuming that the calculated charge value for chemisorption of an oxygen monolayer on the surface of polycrystalline gold is 386 μC cm^{-2} [219,220].

Although the indirect characterization did not manage to properly distinguish between the different C-SPE|AuNSs platforms, by determining the RSAs it could be seen that certain protocols led to the creation of a rougher surface. For instance, P_2 shows a R_f value of 10.59, followed by P_1 and P_4, which have similar R_f values (6.67 and 6.44, respectively) regardless the different dispositions of the AuNSs, e.g., P_1 presents very dense and heterogenous AuNSs.

An increased RSA should lead to enhanced analytical performance for the aptasensor, but these is not always the case, considering that an increased exposed Au surface, with an unfavorable architecture and disposition could lead to unorganized clusters of Fc-APT, which will render inactive some Fc-APT strands.

2.3.3. Selection of a platform for aptasensor elaboration

2.3.3.1. Aptasensor design

Two different strategies, for the immobilization of the Fc-APT were tested, pulse-assisted deposition and as control, overnight incubation with the Fc-APT solution, at 4°C. The results regarding the optimization of the immobilization strategies, both for Fc-APT and MCH are detailly discussed in the next section.

Regardless of the immobilization procedure, after the immobilization of the Fc-APT, an anodic peak, at around + 0.28 V and a cathodic one, at around + 0.20 V, were visible by CV (**Fig. 28A**, P_4|Fc-APT, red), at the APT-functionalized electrode caused by the oxidation and by the subsequent reduction of Fc label attached to the APT. After the blocking step with MCH, both peaks, were greatly reduced in intensity (**Fig. 28A**, P_4|Fc-APT|MCH, blue), indicating the hindrance to the electron transfer caused by the immobilization of MCH. The deposition of MCH can cause the reorientation of the APT, pushing farther away from the electrode surface the redox label and also provides a supplementary insulating layer impeding the non-specific adsorption at Au sites. After incubation with a solution of 1 μM OXT and subsequent binding of OXT, the APT changed its conformation, bringing the Fc label closer to the electrode resulting in an increase in intensity (**Fig. 28A**, P_4|Fc-APT|MCH|OXT, green). Additionally, no significant change was visible after incubation with blank solution (**Fig. 28A**, P_4|Fc-APT|MCH|Blank, dotted orange).

The results obtained using CV were confirmed using the DPV technique, more sensitive, which lead to a better-defined peak caused by the oxidation of the Fc label (**Fig. 28B**). These results lead to the observation that the developed aptasensor is a *"signal-on"* sensor, capable to bind OXT (**Fig. 28E**).

Table X presents the results obtained for the functionalization of one platform, P_4, as representative model, both through direct and indirect characterization.

In order to improve the reproducibility of the values of the final analytical response and to limit the influence caused by the variations in the process of aptasensor fabrication, the final analytical response, caused by the incubation with OXT was calculated as $\Delta I = (I - I_0)/I_0$, where I is the intensity after incubation with OXT and I_0 is the intensity after the immobilization with MCH.

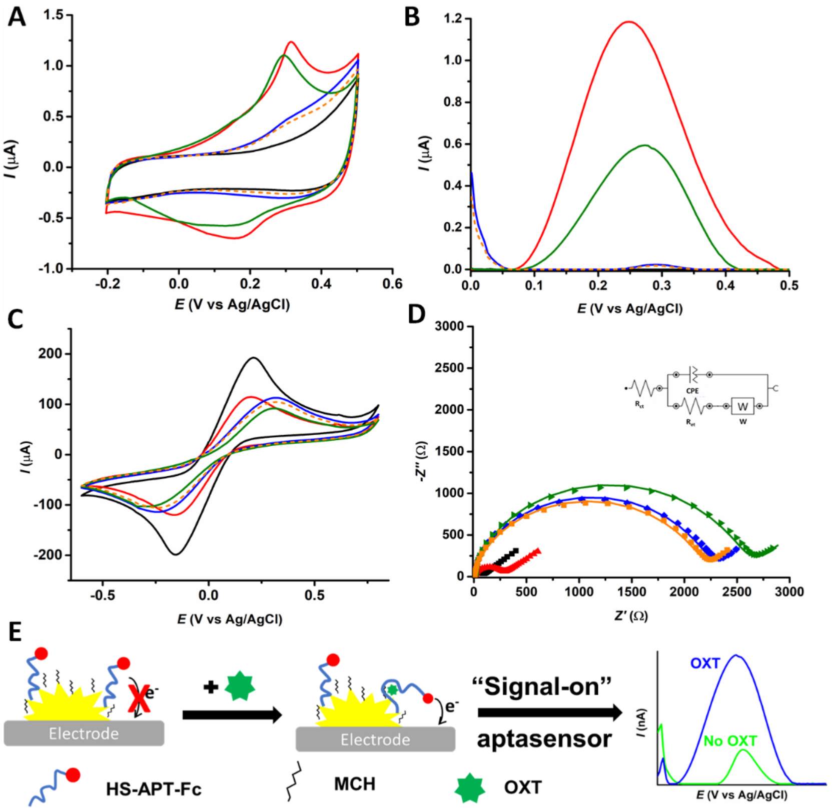

Fig. 28. CVs (**A**) and DPVs (**B**) in 0.1 M KCl and CVs (**C**) and EIS spectra (**D**) in 5 mM $[Fe(CN)_6]^{3-/4-}$ solution in 0.1 M KCl, obtained at P_4, before functionalization (P_4) (**black**), after the pulse-assisted immobilization of Fc-APT (1.0 μM) (P_4|Fc-APT) (**red**), after pulse-assisted blocking with 100.0 μM MCH (P_4|Fc-APT|MCH) (**blue**), after incubation 1 h with 1.0 μM OXT (P_4|Fc-APT|MCH|OXT) (**green**) and after incubation 1 h with TRIS buffer (blank) (P_4|Fc-APT|MCH|Blank) (**dotted orange**); (**D**) the experimental points are represented through symbols and the fitting through the continuous line; *Inset:* The equivalent circuit); (**E**) Schematic representation of the "signal-on" aptasensor.

Table X. The results obtained for the functionalization of the platform P_4 by direct and indirect characterization

Platform	**Direct characterization (Fc-APT redox signal)**					
	CV			**DPV**		
	$I_{pa\ Fc}$ **(nA)**	$(I\text{-}I_0)/I_0$	$I_{pc\ Fc}$ **(nA)**	I_{Fc} **(nA)**	$(I\text{-}I_0)/I_0$	
P_4|Fc-APT	521.8 ± 63.4	-	-203.9 ± 13.7	1190.1 ± 83.4	-	
P_4|Fc-APT|MCH	14.5 ± 2.5	-0.9	-	21.2 ± 1.6	-0.9	
P_4|Fc-APT|MCH|OXT	394.2 ± 42.3	26.2	-158.9 ± 8.4	605.6 ± 29.9	27.5	
	Indirect characterization ($[Fe(CN)_6]^{3-/4-}$ redox signal)					
	CV				**EIS**	
	I_{pa} **(μA)**	I_{pc} **(μA)**	ΔI_{pa} **(%)**	ΔI_{pc} **(%)**	R_{et} **(Ω)**	ΔR_{et} **(Ω)**
P_4	203.4 ±28.07	-191.2 ±27.53	-	-	85.4 ± 6.2	
P_4|Fc-APT	104.8 ±4.0	-100.6 ±0.6	-48.49	-47.35	259.7 ± 28.1	174.4
P_4|Fc-APT|MCH	74.1 ±0.9	-79.66 ±0.1	-29.3	-20.8	2201.7 ± 127.5	1941.9
P_4|Fc-APT|MCH|OXT	70.2 ±0.6	-71.1 ±1.2	-5.2	-10.7	2546.3 ± 157.1	344.6

Considering that the AuNSs can also be somewhat electroactive and in certain cases can contribute to the overall signal, the effects of all the aforementioned steps were also tested indirectly, through CV (**Fig. 27C**) and EIS (**Fig. 27D**), using $[Fe(CN)_6]^{3-/4-}$ redox probe. The immobilization of both Fc-APT and MCH were showed by the decrease of the intensity of the oxidation and reduction peaks of $[Fe(CN)_6]^{3-/4-}$ in CV (**Fig. 28C**, red and blue) and by the increase in the charge transfer resistance in EIS (**Fig. 28D**, red and blue). The incubation with OXT leads to a further decrease in intensity in CV (**Fig. 27C**, green) and in an increase in resistance (**Fig. 28D**, green). The incubation with blank led to little change, rather to a small increase in intensity (**Fig. 28C**, dotted orange) and a decrease in resistance (**Fig. 28D**, dotted orange).

XPS analysis was performed to confirm the presence of the APT bound to the AuNSs at the C-SPE surface of P_4 protocol. The XPS survey scans are shown in **Fig. 29A**. As expected, the majority of gold microstructures were gold in the metal state, Au^0. **Fig. 29B** shows the high-resolution spectrum of the Au_{4f} level. The high-resolution spectrum of Au_{4f} core level is characterized as doublets peaks due to $Au_{4f7/2}$ and $Au_{4f5/2}$ spin-orbit coupling. The $Au^0{}_{4f7/2}$ state BE is 83.8 eV, and the $Au^+{}_{4f7/2}$ state BE is 85.52 eV and 3.6 eV between spin-orbit peaks. The atomic percentages were estimated as: 94.36 for Au^0 and 5.64 percentage for Au^+. The presence of the APT bounded onto the AuNSs is confirmed mainly by the presence of P_{2p} (**Fig. 29A** and **C**). The functionalization of the AuNSs with APT and MCH was also confirmed by the presence of the peak at 162 eV, specific for bound thiols [221,222], in the spectrum of S_{2p} (**Fig. 29D**).

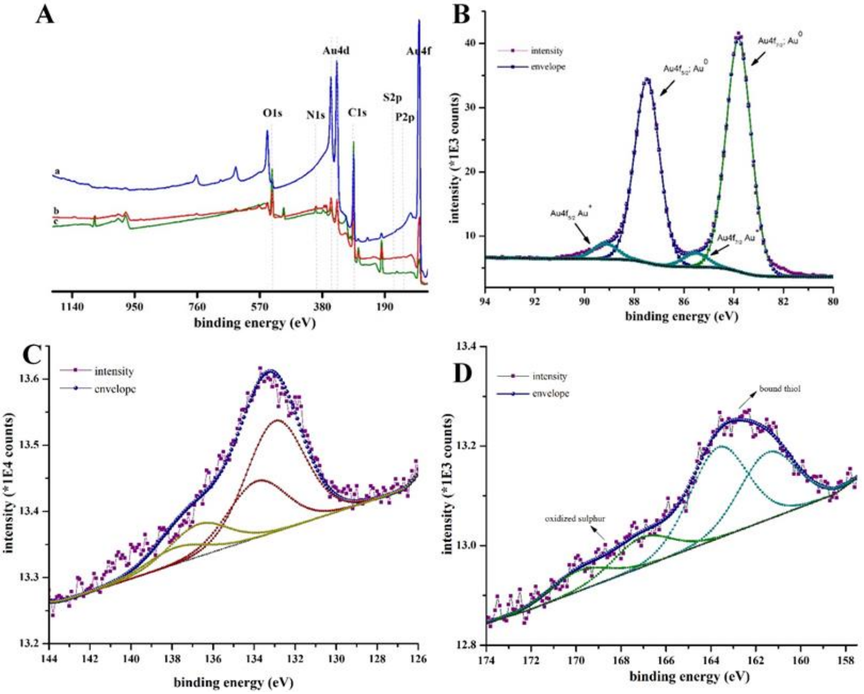

Fig. 29. **(A)** Survey X-Ray photoelectron spectra of P_4|Fc-APT (a); P_4|Fc-APT|MCH (b); P_4 (c); (**B)** High-resolution spectrum Au_{4f} X-Ray photoelectron spectra of P_4|Fc-APT|MCH; **C)** High-resolution spectrum P_{2p} X-Ray photoelectron spectra of P_4|Fc-APT|MCH;(**D**) High-resolution spectrum S_{2p} X-Ray photoelectron spectra of P_4|Fc-APT|MCH.

2.3.3.2. Aptasensor optimization

The immobilization of the Fc-APT on the surface of the transducer is a critical step of the protocol. The optimal coverage of the surface must be obtained for increased sensitivity. Considering the large differences between the surfaces used as starting platform for the development of the aptasensor, two different strategies, for the immobilization of the Fc-APT were tested, simple incubation and pulse-assisted deposition (**Fig. 30A** and **B**). The simple incubation protocol was adapted from the literature[206] and the pulsed-assisted protocol from previous studies of our group[66,223]. Both experimental protocols were adapted in order to achieve the immobilization of the Fc-APT in a controlled manner without affecting in any way the binding properties of the APT.

Another very important aspect to be considered in the elaboration of a sensor, especially of an aptasensor, is the phenomena of non-specific adsorption, which can greatly affect the results of analyses. To prevent this, the free sites, remained unoccupied on the sensing surface after the functionalization with the APT, had to be blocked with MCH, a relatively long-chain thiol that also stabilizes the grafted molecules of APT.

For the proper evaluation of the efficiency of the immobilization procedure, it was not sufficient to consider only the signal obtained after this initial step of functionalization but also the final signal, obtained due to the binding of the analyte. Considering this, the two strategies for the immobilization of thiols, in our case of Fc-APT and MCH were tested in parallel, for both thiols, by studying: (i) the signal after the immobilization of Fc-APT and (ii) after the blocking step with MCH and the binding of the molecule.

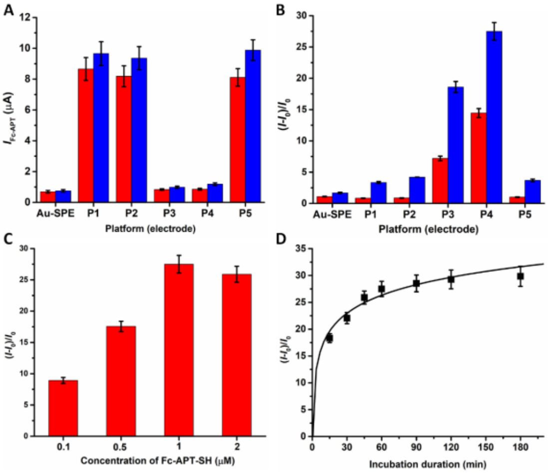

Fig. 30. (**A**) The signal obtained after the immobilization of the Fc-Apt and (**B**) after immobilization of MCH and incubation with 1.0 μM OXT using the two strategies, simple incubation (**red**) and potential-assisted deposition (**blue**); Effect of experimental conditions: (**C**) the concentration of Fc-APT, using P_4, 1 h incubation time with 1.0 μM OXT and (**D**) the incubation time with OXT, using P_4, 1.0 μM Fc-Apt for functionalization and 1.0 μM OXT.

The tests also revealed the superiority of the pulse-assisted method over the simple incubation method, both for the initial phase of functionalization with APT and for the final phase, of the binding of the analyte, showing not only that a higher amount of Fc-APT was bound in the initial phase but also that its disposition on the surface and implicitly its ability of binding the analyte was increased. The influence of the pulse-assisted method not only on the total amount of thiol-modified DNA strand bound but also on its arrangement, leading to more ordered monolayers, and on their orientation, by preventing non-specific adsorption of other segments of DNA has been documented in literature[223].

The more drastic effect is the influence of the architecture of the AuNSs on the binding capacities of Fc-APT. The more organized AuNSs, formed predominately from shapes with larger dimensions (P_3, P_4) fared well better than the platforms which had more heterogeneous architecture, with various shapes and sizes (P_1, P_2). This correlates with data from the literature regarding DNA sensors, where it is mentioned that nanostructures with larger footprints had better results, favoring the interaction with slow diffusing analytes[224]. Also, the structures obtained in P_4 have a higher degree of nanostructuring – rougher surface of the main structure, a feature that also greatly enhances the ability of binding OXT[224,225]. Based on the obtained results, P_4 was chosen as the final platform for the development of the aptasensor.

In order to achieve a satisfactory detection performance, two additional parameters were optimized, namely the concentration of Fc-APT used in the MPA procedure (**Fig. 30C**) and the incubation time for the OXT solution (**Fig. 30D**).

As anticipated, the analytical response increased with the increase of the concentration of Fc-APT used for functionalization, from 0.1 µM up to 1 µM. For higher concentrations, the analytical response remained the same or even dropped in value, signaling the fact that optimal concentration was achieved, and higher values will lead to a too dense coverage of the platform with Fc-APT, hindering the binding and electron transfer processes.

The effect of the incubation time of the OXT solution with the aptasensor was also tested, the analytical response increasing with duration of incubation, peaking at around 60 minutes, longer periods not leading to a significant increase in the response as it can be seen in **Fig. 30D**.

2.3.4. Analytical performance of the developed aptasensor

2.3.4.1. Calibration curve

Using the optimized parameters, DPV measurements (**Fig. 31A**) were performed and a calibration curve was constructed (**Fig. 31B**), revealing that the response depended linearly on the concentration of OXT in the range of 0.05 to 1.2 µM, with the correlated equation: $(I - I_0)/I_0 = 26.245 \pm 0.770$ [OXT] (µM) + 1.037 ± 0.542 and with the correlation coefficient $R^2=0.9923$. The corresponding LOD, calculated by dividing three standard deviations of blanks by the slope of the calibration curve, is estimated to be 8.7 nM.

2.3.4.2. Selectivity, regenerability and stability

The selectivity of the aptasensor was tested by recording the signal of OXT in mixture solutions, with other antibiotics and by testing other antibiotics alone. The aptasensor proved to be selective towards OXT, with a significant interference present only in the case of TET, another tetracycline, closely related structurally to OXT (**Fig. 31C**). The possible limited interference of other tetracyclines is caused by certain limitations of the APT in discerning between OXT and other tetracyclines[212]. The overall good selectivity shown by the aptasensor is attributed to the specific recognition ability of the OXT APT, which can specifically recognize and capture the target with self-conformation change.

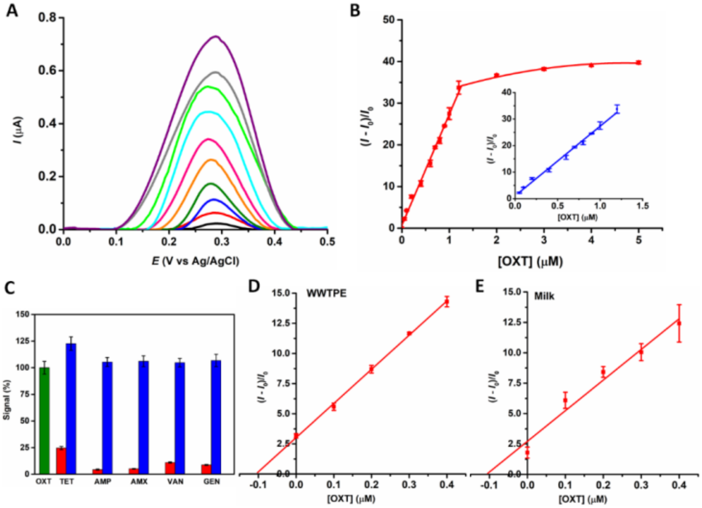

Fig. 31. (**A**) DPVs obtained for blank solution, Tris buffer (**black**) and for different concentrations of OXT: 0.05 μM (**red**), 0.10 μM (**blue**), 0.20 μM (**dark green**), 0.40 μM (**orange**), 0.60 μM (**pink**), 0.70 μM (**cyan**), 0.90 μM (**light green**), 1.00 μM (**grey**), and 1.20 μM (**purple**), in 0.1 M KCl, 1 h incubation; (**B**) Aptasensor signal dependence on the concentration of OXT (*Inset:* linear dependence); (**C**) Relative response of the aptasensor for 1.0 μM OXT alone (**green**), 1.0 μM antibiotic alone (**red**) and for a mixture of 1.0 μM OXT and of 1.0 μM antibiotic (**blue**); Analysis of spiked samples with OXT by the standard addition method using the optimized aptasensor in (**D**) wastewater treatment plant effluent (WWTPE) and (**E**) milk.

To evaluate the capability of regeneration of the aptasensor, the electrode was treated with 2 M NaCl for 10 min to regenerate the APT-immobilized onto the platform after its use. The high concentration of sodium chloride causes disruption of the hydrogen bonds and electrostatic interactions responsible for the APT–target association, subsequently it enables unfolding of APT and the bound OXT is released from APT[226,227]. After each regeneration step, the baseline signal was reevaluated to confirm the efficiency of the regeneration method. After three regeneration cycles, the current response of the aptasensor retained about 93 % of its original response value (RSD of 4.76 %) indicating that this aptasensor has a good regeneration. A drop of more than 50 % of the original response was observable only after a seventh cycle of regeneration.

To determine the stability of the electrochemical APT sensor over time, a batch of five aptasensors was prepared and stored at 4°C for their subsequent testing. Half of the aptasensors were stored in dry conditions and the other half were kept with a drop of buffer onto the electrode. The response of the aptasensors stored in wet conditions, measured for 1 μM OXT was about 94%, 76% and 54% of the original measured value, after one, two and three days of storage, respectively. For the dry conditions the values were of 96%, 92%, 89% and 85% of the original measured value after one, two, three and seven days of storage, respectively. These results demonstrated that the aptasensor storage in dry conditions has a better stability than when it is kept with a drop of the buffer on top. Nevertheless, these aptasensors needed several measurements, 3 – 4 DPV analysis, both in oxidation and reduction, in blank buffer solution to establish a proper baseline. The lower stability of the sensor stored in wet conditions can be explained by the low predisposition of the recognition element to different degradation pathways and rearrangements in aqueous media.

The aptasensor showed good performance in terms of analytical parameters, having a good selectivity and a similar LOD with other electroanalytical methods for the detection of OXT (**Table XI**).

Table XI. Comparison of the presented approach and other electrochemical methods used for OXT detection

No.	Method (s)	Electrochemical platform	LDR (nM)	LOD (nM)	Ref.
1	Label-free aptasensor	Interdigitated array gold electrode chip	1 – 100	N.R.	227
2	PEC Aptasensor	FTOE|BiOI-G	4 - 150	0.9	228
3	“switch off-on” PEC aptasensor	ITOE|TiO2|H-DNA@QD	2 – 300	0.19	229
4	HRP labeled competitive aptasensor	GCE| GO–PANI| AuNPs| OXT-BSA + HRP-APT and sample	8 x 10^{-3} – 2 x 10^{3}	4.6 x 10^{-3}	230
5	Label-free aptasensor	GCE|4-CP	2 – 2 x 10^{5}	0.46	231
6	Label-free aptasensor	AuE|Au@POF	2 x 10^{-5} - 2	6.93 x 10^{-6}	232
7	Labelled, competitive aptasensor	AuE	20.1 – 1207	19.72	156
8	“Signal- off” PEC aptasensor	ITOE|Bi_4VO_8Cl/N-GQDs	0.1 – 150	0.03	233
9	MIP-based sensor	AuE|$(CS\text{-}MWCNTs)_5$| AuNPs|MIP	30 – 8 x 10^{4}	27	234
10	Competitive, GOX-labelled MIP-based sensor	PtE|PB-MIP|GOD-OXT	0 – 100, 100 - 1000	2.3 x 10^{-4}	122
11	Labelled aptasensor	TFGE|APT|MCH|cMWCNT|AuNPs|cDNA|thionine	0.2 x 10^{-3} – 2 x 10^{5}	0.62 x 10^{-4}	235
12	Labelled aptasensor	C-SPE|AuNSs	50 - 1200	9	This work

***NR**: not reported, **AuE**: gold electrode, **ITOE**: Indium tin oxide electrode, **FTOE|BiOI-G**: Fluorine doped Tin Oxide electrode|bismuth oxyiodide doped with graphene, **ITOE|TiO_2|H-DNA@QD**: Indium tin oxide electrode|TiO_2 nanorods|hairpin DNA probe and CdTe quantum dots, **GO–PANI|AuNPs|OXT-BSA**: graphene oxide–polyaniline|Au nanoparticles|Oxytetracycline - Bovine serum albumin, **4-CP**: 4-carboxyphenyl, **AuNPS@POF**: porous organic framework with AuNPs, **Bi_4VO_8Cl/N-GQDs**: Bi_4VO_8Cl/nitrogen-doped graphene quantum dots, **CS-MWCNT**: chitosan-multi-walled carbon nanotube composite, **PtE**: platinum electrode, **PB-MIP**: Prussian Blue molecularly imprinted polymer, **GOX-OXT**: Glucose-oxidase-labeled oxytetracycline, **TFGE**: gold thin film gold electrode, **cMWCNT**: carboxylated multi-walled carbon nanotubes, **cDNA**: complementary strand of APT*

The developed aptasensor has relatively lower cost compared to the reported sensors due to the use of C-SPE which require lower volume of gold salts solution for electrode modification. Also, by using a direct approach, no need for an additional redox probe solution for OXT analysis is required and little non-specific interference is exhibited.

2.3.4.3. Real sample analysis

The applicability and validity of the proposed method were tested on two types of real samples: (1) environmental, represented by wastewater treatment effluent and (2) food samples, represented by whole milk. Both types were spiked with OXT.

By employing the standard addition method for the analysis of wastewater samples (**Fig. 31D**), a slope (28.335 ± 0.626) similar (<10% difference) to that obtained from the pure buffer resulted, thus suggesting little interference of the effluent matrix. The 106.5 ± 5.5% (RSD = 5.20%, n = 3) recovery value indicates the adequate accuracy and repeatability of the proposed method for the real sample[236]. For the milk samples (**Fig. 31E**), the slope was also close to that of the pure buffer (25.212 ± 2.725), but the standard deviation for the slope was significantly higher and with a lower R^2 value, 0.9548 compared to 0.998 for wastewater sample. Similarly, the obtained recovery value, 107.5 ± 4.0% (RSD = 3.78%, n = 3) indicates adequate accuracy and repeatability of the proposed method for the milk samples[236].

Although the analytical parameters were satisfactory for both types of samples, one must consider the supplementary sample pretreatment required by the milk samples, for the same results. This can be attributed to the higher complexity of milk as an analytical matrix.

2.4. Conclusions

C-SPEs were modified with AuNSs, using five different electrodeposition protocols. The morphologies, topographies, and structural composition of the AuNSs were investigated using SEM, AFM and XPS, all platforms presenting distinctive architectures for the AuNSs. Further, the platforms were modified with a ferrocen-labelled aptamer (Fc-APT) and the influence of the paltforms morphologies and arhitectures on the analytical performance of the aptasensor, was evaluated based on the redox signal of Fc-APT.

Using the optimum C-SPE|AuNSs platform, that exhibited a thistle-like gold structures, an innovative and sensitive “signal on” aptasensor was developed for OXT in the range 0.05 to 1.2 μM. The robustness of this method was succesfully confirmed when the aptasensor was applied for the detection of OXT in real samples, represented by wastewater treatment plant effluent and cow milk.

Chapter III. The development of photoelectrochemical methods for the detection of antibiotics

1. Photoelectrochemical detection of rifampicin

1.1. Introduction

Rifampicin is an antibiotic from the rifamycins group introduced for human use in 1960s[237,238]. Despite an increasing incidence of resistance, RIF remains alongside isoniazid an essential first-line antitubercular drug[238].

RIF, a zwitterion at physiological pH contains three phenolic hydroxyls grafted on its naphthalene core structure (**Fig. 32**). Two of them, at positions 1 and 4 form a hydroquinone-like moiety. The third one, position 8, is deprotonated while a piperazine N is protonated ($pK_a = 3$, $pK_b = 7.5$)[239,240]. RIF is slowly oxidized by oxygen in aqueous solutions to form rifampicin quinone RIF-Q (within hours at pH 7.5 and 37° C)[241]. This makes RIF a good target for detection by the singlet oxygen-based detection strategy[169]. The singlet-oxygen strategy for the electrochemical detection of phenolic compounds is described in more detail in the *State of the art* part of the thesis. The molecular structures of the other compounds studied, exhibiting at least one phenol group are shown in **Fig. 32.**

Although the singlet oxygen-based strategy has certain limitations in discerning between different phenolic compounds, a limited selectivity can be reached based on the differences in the oxygenation kinetics by $^1O_2$ for different phenols at different pH values[136,169]. Additionally, the enhanced selectivity and sensitivity of the detection of phenolic analytes could be also based on their interactions with the photosensitizer or its supporting matrix e.g., TiO_2 or SiO_2. The interaction of TiO_2 surface with the vicinal phenols 1,2-dihydroxybenzene and 1,8-dihydroxynaphthalene has been reported[242,243]. In our case, the photosensitizer $F_{64}PcZn$ exhibits a strong Lewis acidic, hydrophilic metal center and a highly hydrophobic ligand cavity, both opposite features being simultaneously imparted by the fluorine substituents[244]. The hydrophilic Zn center may thus contribute to the binding of an analyte via coordination bonds, in addition to van der Waals (vdW) interactions, the latter being observed for non-sterically hindered phthalocyanine materials that adsorb polycyclic aromatic rings[245,246].

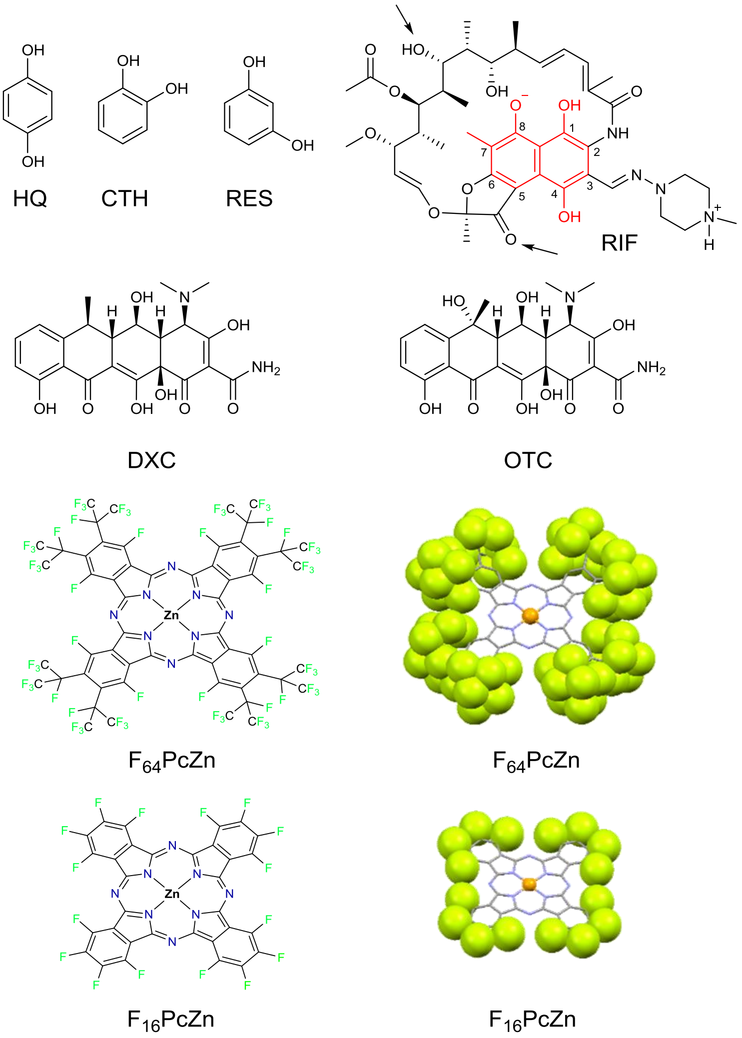

Fig. 32. Molecular structures of studied compounds with at least one phenol group and the FnPcZn phthalocyanines, n = 16, 64. The F atoms are depicted as vdW spheres. The Zn is represented as a small sphere; the remaining atoms are depicted as capped sticks. Color code: Zn, orange; F, green; C, gray; N, blue.

In this study, we report that molecular interactions between the supported $F_{64}PcZn$ photosensitizer deposited on an electrode and RIF result in the selective preconcentration of the latter at the electrode, greatly enhancing the sensitivity of the photoelectrochemical sensor towards RIF. The preconcentration is selective, as it was not observed for simple phenols such as HQ or catechol (CTH) and more complex OH-reach phenols such as antibiotics DXC and OXT.

1.2. Experimental

1.2.1. Materials, instruments and photoelectrochemical measurements

The perfluorinated phthalocyanine zinc complex $F_{64}PcZn$ was synthesized and deposited on TiO_2 (Degussa, P25) as described previously[175] resulting in the supported photosensitizer abbreviated $F_{64}PcZn\cup TiO_2$. HQ, CTH and resorcinol (RES) were purchased from Sigma-Aldrich (Belgium). RIF (>95% purity), DXC (98% purity), and OXT (>95% purity) were purchased from Across Organics. The measuring buffer (phosphate buffer pH 6) consisted of 0.1 M KCl and 20 mM KH_2PO_4 dissolved in ultrapure water (18.2 MΩ, Millipore Simplicity) and adjusted to pH 6. Measuring buffers with a different pH or ionic strength are specified in the text.

The photoelectrochemical measurements were conducted using a PalmSens2 potentiostat from Palmsens BV (Utrecht, The Netherlands) and a red 655 nm diode laser (Roithner Lasertechnik) operating at 30 mW power and adjusted to a spot diameter of 4 mm. A power supply (Arduino Uno) was used to switch on and off the light beam at preprogrammed times. An AvaSpec-2048L UV-Vis spectrophotometer from Avantes (Netherlands) equipped with an AvaLight-DH-S-BAL light source was used for spectrophotometric measurements.

C-SPE (DropSens, Spain) with a carbon working area of 4 mm in diameter were typically, unless stated otherwise, modified by depositing a single 5 µl droplet of an aqueous suspension of 10 mg/mL $F_{64}PcZn\cup TiO_2$ (3% wt.) followed by overnight drying, at room temperature. The modified electrodes are abbreviated C-SPE|$TiO_2\cup F_{64}PcZn$. Both the volume and concentration of $F_{64}PcZn\cup TiO_2$ suspensions were varied to optimize the amount of deposited materials.

Prior to photoelectrochemical measurements, 80 µl of a RIF solution was placed on $F_{64}PcZn\cup TiO_2$|SPE and the electrodes were kept in the dark in a closed vessel. Chronoamperometric measurements were carried out using either a drop of the same RIF solution or buffer (after additional rinsing with buffer). For experiments involving sequential illuminations lasting a total of 4 hours, the drop was refreshed after each illumination. For the hydrodynamic setup, four $F_{64}PcZn\cup TiO_2$|SPEs were immersed in 16 mL of RIF solution and stirred magnetically at 300 rpm for 2 hours. Following the bulk equilibration, the electrodes were removed from the solution, connected to a potentiostat and covered by a single drop of the same RIF solution.

1.2.2 UV-Vis quantification of rifampicin adsorbed on the modifier

1, 2, 3 or 4 mg of solid TiO_2 or $F_{64}PcZn\cup TiO_2$ were weighed in Eppendorf tubes, washed 3x with phosphate buffer pH 6 using a vortex and an ultrasonic bath for resuspension (for 10 min) and then centrifuged at 7000 rpm (for 5 min) to isolate the powders. Finally, the powders were resuspended in 1 mL of 10 µM RIF solution in phosphate buffer pH 6 and left in dark for 2 hours on a mechanical agitator. Afterwards, the suspensions were centrifuged at 14000 rpm for 30 min to remove all solid particles and UV-Vis spectra of the supernatants were recorded using a 0.5 cm a quartz cell to assess the change in the RIF concentration from the initial 10 μM.

1.2.3. Molecular modeling of rifampicin-photosensitizer interactions

The docking of RIF onto F_nPcZn were performed using the *GOLD v. 2020.1* program[247], RIF was designated as the “ligand” while F_nPcZn were the “protein”. RIF conformers were initially generated via *Mercury CSD Conformer Generator v. 2020*[248], to minimize conformational biases during docking calculations. A coordination binding site with a 10 Å radial distances from the Zn center was selected given the likely propensity of RIF oxygen-based functional groups for binding to the electron deficient metal. Docked RIF-PcZn structures were visualized with *Hermes v. 2020.1*[248]. A fine grid of fitting points, keeping the vdW interaction energies below -2.5 kcal/mol was incorporated at the binding site to illustrate van der Waals interactions between F_nPcZn and RIF. Additional dockings were performed using Zn-O bond distance constraints of approximately 2.1, 2.3, and 2.5 Å consistent with statistical data on zinc-oxygen interactions (**Fig. 33**).

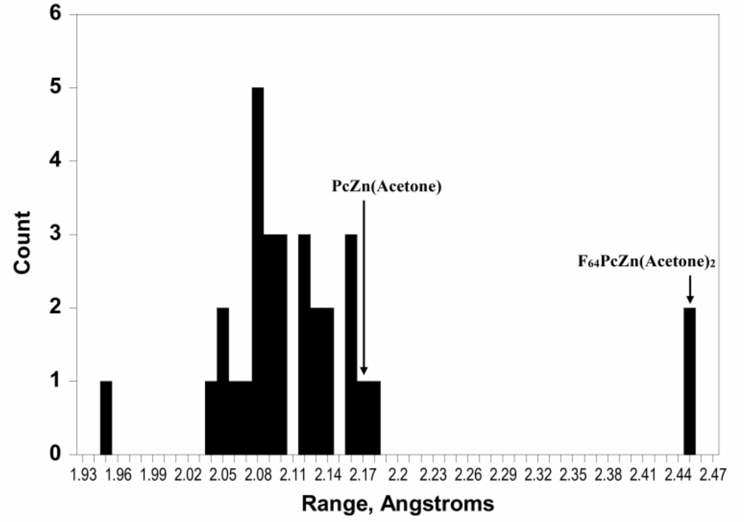

Fig. 33. Statistical analysis of Zn-O bond lengths in PcZn-O(axial ligand) complexes. PcZn(Acetone): Zn-O = 2.167 Å as obtained from crystallographic data, PcZn(Acetone) = (2,3,9,10,16,17-hexakis(2',6'-diisopropylphenoxy)-23-(5,11,17,23-tetra-t-butyl-26,27,28-trihydroxycalix[4]arenyl)-24-chlorophthalocyaninato)-acetone-zinc. The bond length for PcZn (Acetone) is reported by Bezzu *et al.*[249].

Rough RIF-F_nPcZn enthalpic interaction energies were obtained using *MOPAC2016* with the PM7 Hamiltonian. Geometry minimizations were performed until potential energy gradients were <10 kcal/mol/Å for RIF complexes and <1 kcal/mol/Å for F_nPcZn. A dielectric constant, $\varepsilon = 78.4$ was introduced to mimic the aqueous environment in phosphate buffer saline.

1.2.4. Real samples analysis

Samples of effluents obtained from the Cluj-Napoca Wastewater Treatment Plant (Somes Company, Cluj, Romania) were spiked with a solution of RIF in phosphate buffer pH 6 and passed through a 0.45 µm pore size membrane filter (Chromafil AO-45/25, Macherey-Nagel, Germany) to give a final RIF concentration of 1 µM. Samples were diluted 10 times with the measuring buffer before being analyzed.

1.3. Results and discussion

1.3.1. Photoelectrochemical detection of rifampicin

The $^1O_2$-based photoelectrochemical detection of phenols, including RIF is shown in **Fig. 34A**. The detection of RIF (or HQ) relies on two main processes: (1) the oxidation of RIF by $^1O_2$ that is generated by $F_{64}PcZn$ under illumination from air oxygen, and (2) the electrochemical reduction at an electrode of a formed product or products. These two processes create the redox cycling that enhances sensitivity of the detection method[169].

The method has been proven to work for antibiotics containing a phenolic moiety such as AMX, CFD and DXC[136,169]. RIF contains a HQ moiety that can be reversibly oxidized into the corresponding quinone RIF ↔ RIF-Q, **Fig. 34A**. Thus, RIF is expected to be well-detectable via oxidation with $^1O_2$. The zwitterionic and oxidized forms of RIF, however, are large molecules with multiple functionalities and charges that may interact with $F_{64}PcZn{\cup}TiO_2$ and the electrode material (carbon ink) complicating the detection. Indeed, the profile of the amperometric response drastically differs for RIF in comparison with HQ, **Fig. 34B**. In the first few seconds after the light triggered the response, the photocurrent was similar for both HQ and RIF, but decayed for RIF while remaining constant for HQ. The steady-state photocurrent for RIF was reached in about 10 min resulting in a four times lower value compared to the steady-state current for HQ.

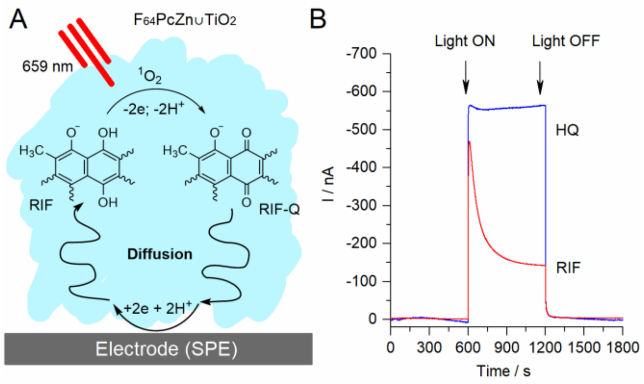

Fig. 34. (**A**) Schematic representation of the mechanism for the photocurrent response of RIF using the $F_{64}PcZn\cup TiO_2$|SPE electrode. (**B**) A typical photoelectrochemical response at −0.1 V potential of 10 μM HQ (**blue**) and 10 μM RIF (**red**) in phosphate buffer pH 6.

The shape of the current response as a function of time suggests that RIF and RIF-Q may exhibit poor diffusion in the $F_{64}PcZn\cup TiO_2$ layer, leading to the corresponding decay of the photocurrent measured by C-SPE|$F_{64}PcZn\cup TiO_2$. The slow diffusion may result in slow equilibration of the electrode in the RIF solution, a hypothesis that was examined by using longer equilibration times combined with (1) multiple short illuminations, or (2) a single illumination at the end of the long equilibration time, **Fig. 35.** Considering the significant decay of the signal, **Fig. 34B**, the illumination time was shortened to 10 s.

Sequential illumination/dark cycles, 10/290s, **Fig. 35A** revealed that the photocurrent for RIF increased 1.8 times during first 10 – 12 illumination/dark periods and stabilized afterwards, i.e. after about 1 hour. In contrast, the HQ photocurrent showed a small decrease by 17% using the same illumination protocol during the first 5 – 6 periods, **Fig. 35B**, reaching after about 30 minutes a stable value identical to the response of RIF.

Surprisingly, an extended equilibration step without illumination, about 70 min, similar to the time of the first 12 dark/illumination periods (60 min) resulted in a further enhancement of the photocurrent for RIF, (**Fig. 35C**), compared with both the response after 5 and 60 min (**Fig. 35A**). Under prolonged equilibration, the photocurrent response for RIF (**Fig. 35C**), was even higher than that for HQ (**Fig. 35D).** Moreover, the equilibration step was more efficient for RIF even without the potential applied (compare **Fig. 35C** and **Fig. 35E**). To conclude, the photocurrent response for RIF (−1.2 μA) was 2x the response of HQ (−0.62 μA) obtained after equilibration of disconnected electrodes in RIF or HQ solutions, respectively, while the response of RIF after the equilibration was 5x the response of RIF without the equilibration step (the first illumination in **Fig. 35A**).

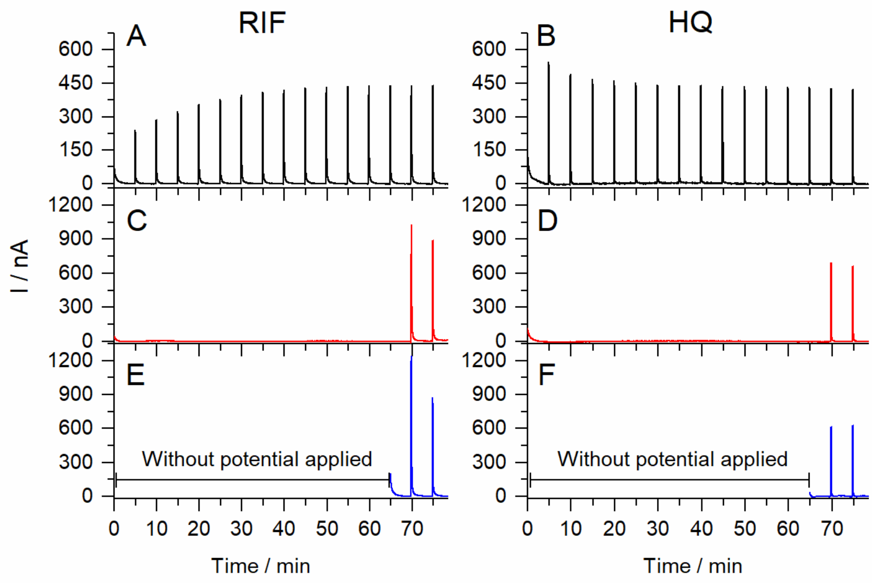

Fig. 35. Photoelectrochemical measurements of 10 µM RIF (**A**, **C**, **E**) and 10 µM HQ (**B**, **D**, **F**) in phosphate buffer pH 6 using a series of cycles of dark (290 s) and light (10 s) periods (**A**, **B**); a long preconditioning in dark for 70 min followed by a short illumination for 10 s at a continuously polarized electrode (**C**, **D**); and a long equilibration step (65 min) of a disconnected electrode followed by a measurement with a short illumination time of 10 s (**E** and **F**). Potential applied −0.1 V. Coating, 4 µg/mm^2.

Taken together, RIF can be preconcentrated at the surface of the modified electrode during the equilibration period, resulting in an enhanced sensitivity to RIF in solution compared with HQ. Given the above, a protocol that includes the preconcentration step of RIF without electrode polarization was employed. This protocol insured that the highest response was obtained and allowed the simultaneous equilibration of several electrodes.

1.3.2. Kinetics of rifampicin preconcentration on the modified electrodes

The diffusion of RIF is slow and thus the saturation of the interfacial $F_{64}PcZn \cup TiO_2$ layer may require hours. Hence, the maximum current response depends on the initial concentration of RIF in solution and the thickness of the $F_{64}PcZn \cup TiO_2$ layer on the electrode. The general picture of RIF accumulation kinetics was obtained using a batch of electrodes incubated separately for a given time in RIF solution. For the first 120 min, a near-constant photocurrent was measured for HQ, whereas for RIF a steep increase in the photocurrent, that reached −1200 nA, was observed, **Fig. 36A**. Decreases up to 30% were observed after an additional 120 min, attributed to the worsening of adhesion of the $F_{64}PcZn \cup TiO_2$ coating with time, and, thus, its mechanical instability during electrode manipulations.

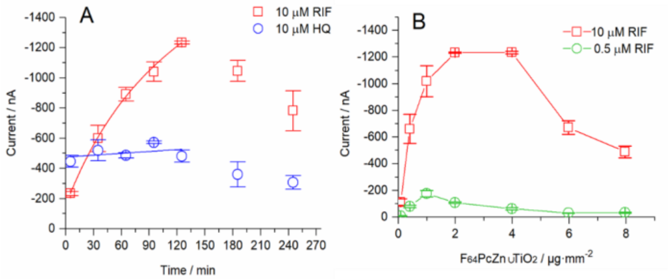

Fig. 36. (A) The photoelectrochemical response to 10 µM RIF (**red**) and 10 µM HQ (**blue**) as a function of incubation time. (B) Effect of $F_{64}PcZn\cup TiO_2$ coverage (layer thickness) on the photoelectrochemical response after 2 h incubation in 10 and 0.5 µM RIF. Each data point was measured using three separate electrodes incubated individually in a drop of RIF or HQ solution for a given time.

The effect of $F_{64}PcZn\cup TiO_2$ coating amount was examined next. A set of electrodes with coatings ranging from 0.08 to 8 µg/mm^2 preequilibrated in RIF solution for 120 min were tested, **Fig. 36B**. For 10 µM RIF concentration, the current increases roughly proportionally up to 2 µg/mm^2 when the entire electrode seems to be coated (**Fig. 37A**). Then the current intensity drops with increase loading reaching 50% of its maximum value at 8 µg/mm^2. This can be explained by the accumulation of RIF in the upper part of the layer which slows the equilibration of $F_{64}PcZn\cup TiO_2$ in the part of the layer close to the electrode. This is additionally confirmed by a decrease in the gradient of the time-dependent signal with the amount of $F_{64}PcZn\cup TiO_2$, **Fig. 37B.**

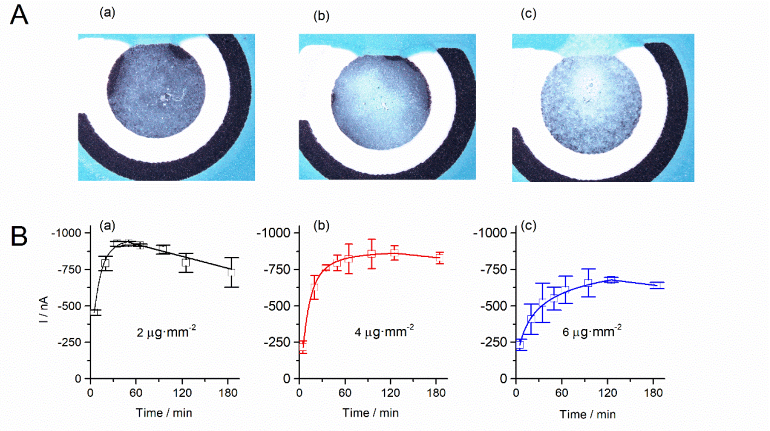

Fig. 37. (**A**) Visual comparison of electrodes covered by 2, 4 and 6 µg·mm^{-2} $F_{64}PcZn\cup TiO_2$. (**B**) The influence of the $F_{64}PcZn\cup TiO_2$ layer thickness, expressed as weight/surface loading on preconcentration kinetics of RIF detected using $F_{64}PcZn\cup TiO_2$|SPE. The photoelectrochemical response of 10 µM RIF, using a protocol involving sequential 10 s laser illuminations every 15 min for the first hour, followed by every 30 min for the second hour, on the same electrode coated with $F_{64}PcZn\cup TiO_2$ of three different thicknesses. Potential applied: −0.1 V.

Interestingly, the effect of the layer thickness was much more pronounced for 0.5 μM RIF with the maximum photocurrent at 1 μg/mm^2 (in contrast to 2–4 μg/mm^2 for 10 μM RIF) followed by a 5-fold drop in the response then the thickness of the layer increased 8 times (from 1 to 8 μg/mm^2) (**Fig. 37B**). Thus, thinner coatings seemly improve the detection of RIF in the sub-micromolar concentration range by facilitating the saturation of the photosensitizer at proximity to the electrode but may limit the sensitivity at higher concentrations due to saturation of the $F_{64}PcZn \cup TiO_2$ layer.

1.3.3. Rifampicin adsorption by the modifying layer

The adsorption of RIF was probed by using electrodes pre-equilibrated in a solution of RIF, washed in pure buffer and then used for detection of the photocurrent. **Fig. 38A** shows the responses of RIF and, for comparison, HQ, with and without washing with pure buffer. Following a single washing, the initial signal, **Fig. 38A**, trace (a) loses about 60% of its intensity, **Fig. 38A**, trace (b) but this value remains constant at least after the third washing, **Fig. 38A**, trace (c). In contrast to RIF, the photocurrent response for HQ dropped to the level of blanks after washing with pure buffer as shown in **Fig. 38A**, traces (d)-(g). These data indicate that even after rigorous washing RIF remained at the electrode, whereas HQ was easily and completely removed, thus suggesting that preconcentration imparts detection selectivity, simple phenols being prevented from interfering by washing. Further proof of RIF adsorption was obtained by measuring directly its concentration decrease in solution in the presence of $F_{64}PcZn \cup TiO_2$, **Fig. 38B**. Following incubation of a 1 mL 10 μM RIF solution with 1 mg/mL suspension $F_{64}PcZn \cup TiO_2$, a composition roughly corresponding to conditions of amperometric analysis with C-SPE|$F_{64}PcZn \cup TiO_2$ (50 μl drop of 10 μM RIF, 4 μg/mm^2 $F_{64}PcZn \cup TiO_2$ or 50 μg per electrode), a decrease in UV-Vis absorbance at 474 nm after 2 h incubation corresponding to loss of 27% of RIF was observed. Increasing the amount of $F_{64}PcZn \cup TiO_2$ fourfold resulted in the near complete removal of RIF from the solution. In average, 3.0 ± 0.6 nmol RIF are adsorbed on 1 mg $F_{64}PcZn \cup TiO_2$, which is comparatively large. A layer of 4 μg/mm^2 can create deficiency of RIF over 1 mm distance from C-SPE|$F_{64}PcZn \cup TiO_2$ already for 10 μM RIF unstirred solution or even larger distances for more diluted RIF solutions, which correlates well with slow kinetics of RIF preconcentration.

Since TiO_2 alone does not absorb RIF, **Fig. 38C**, the preconcentration of RIF by C-SPE|$F_{64}PcZn \cup TiO_2$ is ascribed to the supported fluorinated photosensitizer, $F_{64}PcZn$. Theoretical modeling provides insights into this binding.

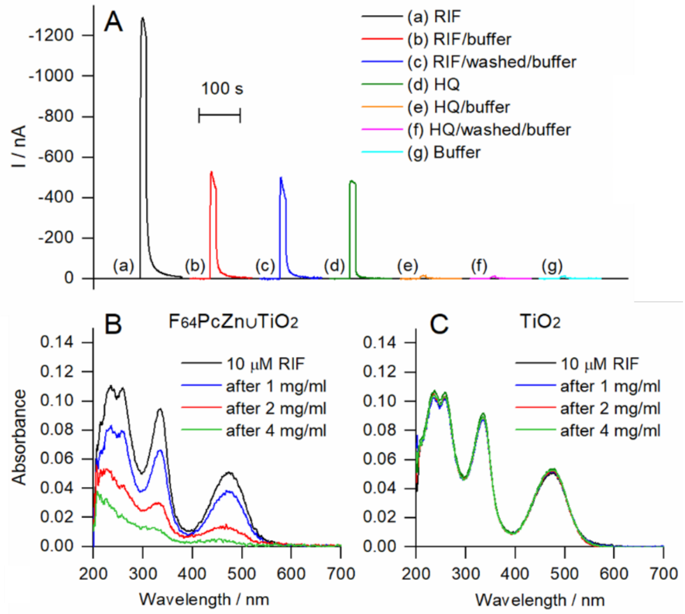

Fig. 38. Photoelectrochemical responses (**A**) of 10 μM RIF (a-c), 10 μM HQ (d-f) and blank buffer (g) obtained after 2 h incubation in the respective solution followed by either testing using the same solution (a, d) or washing and testing in blank buffer (b, c, e, f). The UV-Vis spectra of the RIF solution after incubation with different amounts of $F_{64}PcZn\cup TiO_2$ (**B**) and TiO_2 (**C**).

1.3.4. Molecular modeling of the rifampicin-photosensitizer interactions

RIF exhibits aromatic rings and N- and O-based functional groups that could contact the phthalocyanine scaffold via stacking, vdW or metal-coordination interactions. The absence of adsorption effects for HQ and 4-aminophenol[8] suggest that the interactions of amino- or phenol groups alone cannot explain the observed RIF-F_{64}PcZn interactions. Notably, HQ and 4-aminophenol are relatively small and thus the coordination of their O and N groups to the Zn centers of phthalocyanines is not sterically hindered (**Fig. 32**). Aromatic stacking interactions are also not precluded for F_{16}PcZn, but they are for F_{64}PcZn by the *iso*-perfluoro alkyl groups (*iso*-R_f). On the other hand, the bulky, peripheral *iso*-R_f groups form a hydrophobic cavity around the metal raising the possibility of vdW interactions, including with RIF. Insights into the role of *iso*-R_f groups, the structural chemistry of F_{64}PcZn was compared with that of F_{16}PcZn, an electronically similar complex, but with all *iso* perfluoro alkyl groups replaced by aromatic F groups (**Fig. 32**). The hydrophobic cavity is thus eliminated, rendering F_{16}PcZn sterically unhindered. A histogram of the Zn-O bond length in F_nPcZn-O complexes, (**Fig. 33**), with the oxygen belonging to water, ether, ketone, alcohol, ester, amide, sulfoxide, phosphine oxide and nitrito functional groups revealed a quasi-Gaussian distribution. The PcZn-O distances vary between 1.949 and 2.178 Å, with a mean of 2.100(9) Å for the crystal structures with R < 15% reported in the Cambridge Structural Database (CSD, 03/2020 update), with the notable exception of the F_{64}PcZn(acetone)$_2$ outlier, for which the Zn-O distance is 2.445 Å. Long bonds indicate weak binding and thus one would predict an unstable F_{64}PcZn(acetone) complex despite the enhanced Lewis acidity of the Zn imparted by the fluorine-rich ligand. Yet the complex has been stable in crystalline form for over a year in air, a fact that could be ascribed not only to the usual (unspecified) "solid-state effects", but, more specific, at least in part, to the vdW interactions of acetone with the fluorinated pocket in which it resides. The geometry of the optimized F_{16}PcZn-RIF and F_{64}PcZn-RIF complexes is shown in **Fig. 39**. The keto group of RIF, marked with an arrow in **Fig. 32** is the closest to the metal center of F_{64}PcZn, Zn---O = 4.328 Å. A shorter distance, 3.466 Å is noted for the Zn---OH (aliphatic), F_{16}PcZn. Both distances are, however, at least ~50% longer than the Zn-O range mentioned above and thus the binding is extremely weak. Nevertheless, based only on Zn---O coordinative interactions RIF cannot be expected to have a much higher affinity for F_{64}PcZn, but its stronger association with it is suggested by molecular mechanics based on its vdW interactions with the *iso*-R_f groups, as also illustrated by the 2x more vdW fit points for F_{64}PcZn-RIF relative to F_{16}PcZn-RIF (**Fig. 40**).

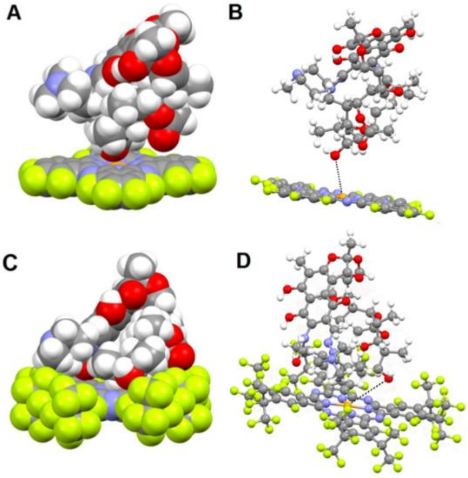

Fig. 39. Geometry optimized complexes of F16PcZn-RIF and F64PcZn-RIF depicting all atoms as vdW sphere (**A** and **C**) and ball-and-stick (**B** and **D**) representations. Color code: Zn, orange, C, gray, F, green, N, blue, O, red. Measured Zn-O bond distances were 3.466 Å and 4.328 Å.

The zwitterionic form of RIF was also modeled. This form is present in solution, but it is unlikely to exist in the absorbed RIF since the phenolic oxygen, position 8, cannot approach the Zn while the aliphatic OH is unlikely to ionize, while the ketone group does not, a keto-enol equilibrium notwithstanding. Consistent with this view, X-ray structures at 2.70 Å resolution of poxvirus-rifampicin complexes reveal that the antibiotic is in its neutral form[250]. The modeling indicates that the neutral and zwitterionic RIFs behave similarly with respect to binding F_nPcZn, the binding to $F_{64}PcZn$ over $F_{16}PcZn$ is favorite, thus supporting the conclusions reached for the neutral form.

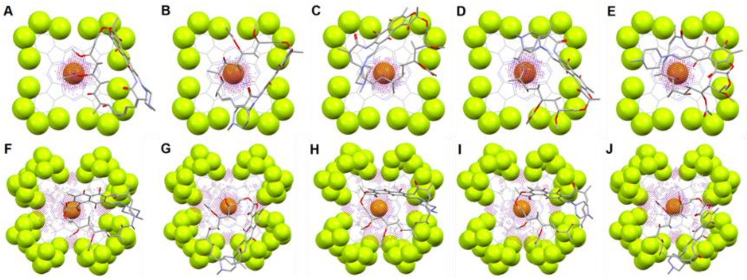

Fig. 40*.* van der Waals interactions illustrated as point nodes, colored in purple between five RIF conformers and $F_{16}PcZn$ (**A-E)** and $F_{64}PcZn$ (**F-J**). RIF conformers were randomly generated and locally minimized before docking. Color code: Zn, orange, C, grey, F, green, N, blue, O, red. RIF conformers are represented as capped sticks, while $F_{16}PcZn$ and $F_{64}PcZn$ are shown as wire frame, with the exception of the fluorine atoms, which are depicted as van der Waals spheres.

Consistent with the computed lack of significant variations of RIF-C-SPE|$F_{64}PcZn\cup TiO_2$ interactions, as well as with the lack of electrostatic-type interactions, whether RIF is a neutral molecule or a zwitterion, the photocurrent was found to be virtually independent of the ionic strength of the pH 6 phosphate, **Fig. 41A**. This observation is also consistent with predominant van der Waals type RIF-$F_{64}PcZn\cup TiO_2$ interactions. Given the lack of ionic strength influence and in order to ensure reliable and reproducible conditions in further measurements, a standard phosphate buffer containing 20 mM phosphate and 100 mM KCl was used in all experiments.

1.3.5. Optimization of the detection protocol

The applied potential, pH and the photosensitizer loading on TiO_2 were varied to determine optimal conditions for preconcentration and detection of RIF. In particular, the working potential defines the kinetics of the electrochemical reduction of RIF-Q and should be optimized to ensure the maximal possible response at an acceptably low background current. The potential was varied from +0.10 V to −0.20 V. As shown in **Fig. 41B**, the photocurrent response of RIF reaches a maximum at −0.10 V, decreasing at −0.15 V and further at −0.2 V. Thus, for the efficient reduction of RIF-Q a potential of −0.10 V was chosen for all experiments. This choice is consistent with our previous studies on other phenolic compounds in similar conditions[136,169], a relatively low overpotential improves the selectivity by preventing possible oxidation of interfering analytes. This is an important advantage over oxidative amperometric or voltammetric detections[94,237].

We have established previously for several phenols[136], that higher pH values increase significantly the photocurrent response due to an increase in the oxidation rate of deprotonated phenols by $^1O_2$. However, RIF is chemically unstable at pH above 8 and below 4[251]. Thus, we studied the photocurrent response in this pH range using phosphate, citrate and Tris buffers. As shown in **Fig. 41C**, Tris slightly improves the detection at pH 7 and 8 but the currents were not higher than those observed for phosphate at pH 6. The photocurrent was optimal in phosphate buffer pH 6, which is close to the optimal pH for extraction of RIF into a dimethylpolysiloxane layer used in HPLC assisted by stir bar-sorptive extraction[252]. A decrease in the photocurrent at pH 7 and 8 drastically differs from our previous work with other phenolic analytes where the photocurrent increased at higher pH[136]. This difference is ascribed to better preconcentration and mobility of RIF at pH 6 in the $F_{64}PcZn \cup TiO_2$ layer.

Fig. 41D depicts the effect of $F_{64}PcZn$ wt% loading on TiO_2 on the photocurrent response. The photocurrent increased linearly with the loading up to 2wt%, a value consistent with the 3wt% one needed for monolayer coverage on TiO_2. Additional $F_{64}PcZn$ layers on top of the layer in direct contact with the substrate may act as barriers, surface morphology modifier as well as optical light absorbers thus limiting the efficiency of the photooxidation reaction.

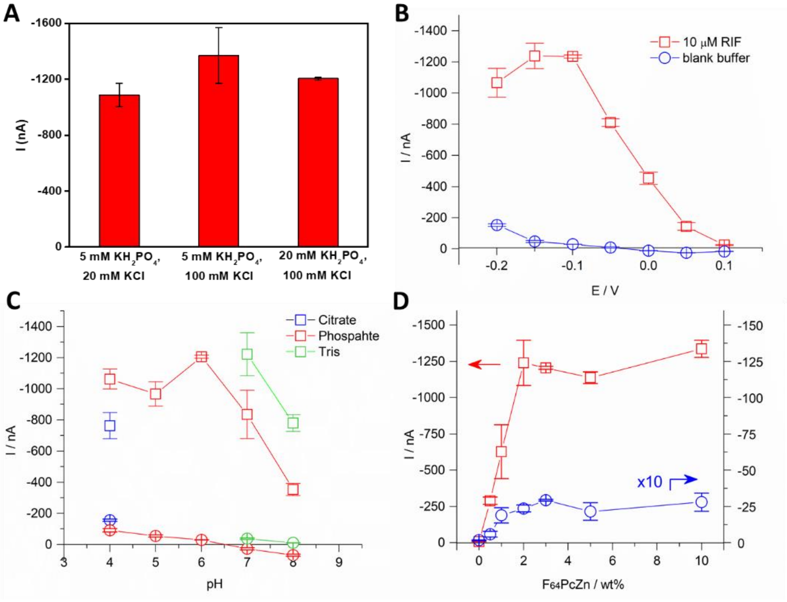

Fig. 41. The influence of the ionic strength of the phosphate buffer (**A**), of the potential (**B**), pH (**C**) and the $F_{64}PcZn$ loading in TiO_2 matrix (**D**) on the photocurrent response. Concentration of RIF, 10 mM; incubation time, 120 min. Other parameters are the same as in **Fig. 35**.

1.3.6. Analytical performance

Taken together, the optimization studies led to the selection of 1 and 4 μg/mm^2 coatings for the construction of calibration curves. **Fig. 42A** shows that the photocurrent response depended linearly on the concentration of RIF in the range of 0.05 - 2.5 μM and 0.1 - 10 μM for 1 and 4 μg/mm^2 $F_{64}PcZn{\cup}TiO_2$, respectively. Both ranges span about 2 orders of magnitude, but the one for the thicker coating was larger, congruent with the slow diffusion and accumulation of RIF. Conversely, the sensitivity in the low concentration range was more than three times higher for the thin layer, the slope being 348 nA·μM^{-1} (2.77 A·M^{-1}·cm^{-2}) and 95.3 nA·μM^{-1} (0.76 A·M^{-1}·cm^{-2}) for the 1 and 4 μg/mm^2 coverages, respectively.

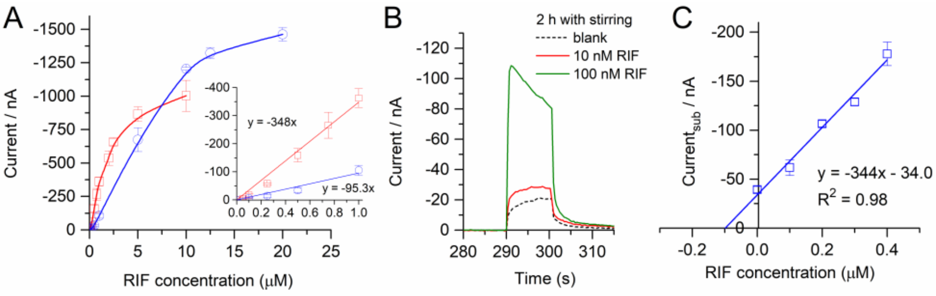

Fig. 42. (**A**) Calibration plots for RIF obtained at electrodes coated with 1 (in red) and 4 μg/mm^2 (in blue) $F_{64}PcZn{\cup}TiO_2$. (**B**) Representative chronoamperograms using SPE coated with 1 μg·mm^{-2} $F_{64}PcZn{\cup}TiO_2$. The sensors were immersed in 16 ml of blank buffer or a corresponding RIF solution and stirred magnetically at 300 rpm for 2 hours before the detection of RIF. (**C**) Analysis of an effluent spiked with RIF by the standard addition method using electrodes with 1 μg·mm^{-2} $F_{64}PcZn{\cup}TiO_2$. The blank signal of pure buffer was subtracted from the measurements.

The corresponding LOD, equals 3 standard deviations of blanks divided by the slope of the calibration curve, LOD = 3·SD$_{blank}$/slope, are estimated to be 7 and 28 nM for 1 and 4 μg/mm^2 $F_{64}PcZn{\cup}TiO_2$ coatings, respectively. Similarly, the corresponding ***l***imit ***o***f **q**uantificiation (LOQ), equals 10 standard deviation of blanks divided by the slope of the calibration curve, LOQ = 10·SD$_{blank}$/slope, are estimated to be 22 and 92 nM for 1 and 4 μg/mm^2 $F_{64}PcZn{\cup}TiO_2$ coatings, respectively. These values, however, are difficult to reach in practice due to the slow preconcentration diffusion of RIF in dilute solutions. The accumulations can be accelerated by stirring, leading to a lowering of the LOD from 28 to 10 nM, as illustrated in **Fig. 42B**.

Importantly, the reported analysis method is more sensitive than the spectrophotometric assay (LOD = 0.7 μM)[253] as well as chromatographic[254,255] or electrophoretic[256] methods coupled with a UV-detector (**Table XII**).

The reported method is also comparatively simple to set-up and use. Indeed, enhanced sensitivity techniques have been used for the electrochemical detection of antituberculous drugs, mainly by adsorptive stripping voltammetry and various electrode modifications[94,237], including with metallic lead, GO, AuNPS and AgNPs, carbon dots, metal oxides, molecularly imprinted polypyrrole and cyclodextrines and various combinations thereof. Most of these materials increase the electrode surface area, preconcentrate the analyte and facilitate its oxidation resulting in LOD values from low nanomolar to micromolar range. In contrast, the reported electrode modification requires neither a complex architecture nor modification procedures and can be easily scaled up for mass production while exhibiting one of the lowest LOD demonstrated.

Table XII. Comparison of the reported approach with other analytical methods of RIF detection

No.	**Method(s)**		**LDR (µM)**	**LOD (µM)**	**Sample**	**Ref.**
1	UF-UPLC-UV		0.08 - 31.59	NR	Serum	[254]
2	SPEx-HPLC-UV		0.61 - 24.3	0.24 (plasma) 0.61 (blood)	Plasma, blood	[255]
3	RP-HPTLC-UV-Vis		NR	NR	Pharm. Form.	[257]
4	CZE-UV		37.43 - 69.51	0.41	Pharm. Form.	[256]
5	Spectrophotometric (UV-Vis)		1.82 - 7.29	0.71	Pharm. Form.	[253]
6	Singlet oxygen based photocatalysis with electrochemical detection	4 $\mu g\cdot mm^{-2}$ $F_{64}PcZn\cup TiO_2$	0.1 – 12.5	0.028	Wastewater	This work
		1 $\mu g\cdot mm^{-2}$ $F_{64}PcZn\cup TiO_2$	0.05 – 2.5	0.007		

UF-UPLC-UV: ultrafiltration and Ultra Performance Liquid Chromatography with UV, SPEx-HPLC-UV: solid phase extraction – high performance liquid chromatography with UV detection. RP-HPTLC-UV-Vis: reversed-phase-high-performance thin-layer chromatography with UV-Vis detection. CZE-UV: capillary zone electrophoresis with ultraviolet detection.

Finally, the practical applicability and validity of the proposed method was tested on a wastewater treatment effluent spiked with RIF. The standard addition method, **Fig. 43C**, yields a 344 $nA\cdot\mu M^{-1}$ slope identical to that obtained from the pure buffer, thus suggesting no interference of the effluent matrix. The 99 ± 6% (RSD = 6.2%, n = 3) recovery value indicates the adequate accuracy and repeatability of the proposed method for real sample analysis.

Additional improvement in selectivity toward phenols that adsorbs in the layer of the photosensitizer can be envisaged due to the retention of the analyte in the layer under washing with pure buffer. **Table XIII** lists relative response of RIF in comparison to three simplest dihydroxybenzenes (HQ, CTH, RES) and DXC and OTC, two antibiotics bearing several functional groups, including a phenolic moiety. RIF exhibited the highest photocurrent, followed by HQ, CTH and DXC.

Table XIII. Photocurrent responses of phenols after incubation of electrodes for 2 h in their 10 μM solutions

Analyte	**Photocurrent / μA**	
	Measured in tested solutions	**Washed and measured in pure buffer**
RIF	−1.210 ± 0.010 (100%)	−0.480 ± 0.020 (100%)
HQ	−0.454 ± 0.003 (38%)	−0.016 ± 0.002 (3%)
CTH	−0.280 ± 0.050 (23%)	−0.059 ± 0.017 (12%)
RES	−0.004 ± 0.007 (0%)	−0.004 ± 0.002 (1%)
DXC	−0.100 ± 0.005 (8%)	−0.017 ± 0.004 (4%)
OXT	−0.030± 0.001 (2%)	−0.003 ± 0.002 (1%)

Remarkably, the washing step widened the gap between the photocurrent responses of RIF and the other compounds. Except for RIF, only CTH was noticeably retained at the electrode after the washings, although showing a 5x loss of signal. In general, the interference of dihydroxybenzenes and both tetracyclines was diminished after the washing step.

1.4. Conclusions

We demonstrate for the first time that a functionalized molecular photocatalyst (photosensitizer type II) exhibits analyte selectivity in interacting with a complex phenolic compound, viz. the antibiotic RIF, while showing no significant interactions with HQ or another complex phenolic compound, the antibiotic DXC. Experimental and modeling studies suggest the appearance of a preconcentration effect in a comparatively thick electrically nonconductive layer, which results in a favorable LOD, 7 nM (6 ppb). The preconcentration of RIF, a phenolic analyte in a thick, electrically nonconductive layer at the electrode surface is effective despite of its strong adsorption, resulting in a complex interplay among the diffusion, adsorption/desorption kinetics and photocatalytic oxidation/electrochemical reduction. Thus, functionalizing a robust photocatalyst and a supporting material with the aim of preconcentration of an analyte is an attractive strategy to fabricate cost-effective and ultrasensitive photoelectrochemical sensors.

IV. General conclusions

The aim of this thesis was to develop new electrochemical methods for the detection of antibiotics by employing and expanding on several strategies, like biomimetic sensors and electrochemical fingerprinting.

In the studies presented, the work focuses more on the analytical strategy used and its associated platform, but what unites them is the analyte, always an antibiotic, and the use of electrochemistry.

Although all classified therapeutically as antibiotics, the target analytes were varied, belonging to four different antibiotic classes, glycopeptides, betalactams, tetracyclines and rifamycins. This means different chemical structures requiring the use of a different approach for each analyte. Similarly, the methods were developed for the detection of the analytes in various matrices, from environmental, such as river water and WWTPE, to food samples, like milk, or even biological fluids, e.g. commercially available human serum. This variety in the target samples also implies a particular approach, adapted for each one, which requires the development and employment of specific pretreatment methods, especially for the more complex matrices.

The five studies detailed in this thesis can be roughly grouped into three groups, based on the analytical strategy employed.

The first group, presented in the first chapter of *Personal contributions*, is represented by direct electrochemical methods. The two studies from this part focus on the direct electrochemical signal of VAN, exploited by the creation of its electrochemical fingerprint using SPE and on the interaction between VAN and AuNSs, which are used for the development of a method based on a composite graphene-AuNSs electrode.

The second group focuses on the use of biomimetic elements, MIPs and APTs. In the first study, a simple indirect MIP-based sensor was developed for CFX, using electropolymerization in aqueous medium. In the second study, we used a ferrocene-labelled APT and C-SPE modified with AuNSs for the construction of a “signal-on” aptasensor for OXT. Both studies revealed the advantages in terms of sensitivity and selectivity of the biomimetic elements. Also, through these studies, different additional strategies were introduced and tested, like different starting platforms (BDDE, C-SPE|AuNSs) and immobilization procedures.

The hyphenation of electrochemical methods with other analytical methods was explored in the last chapter. In the last study, presented in this chapter, the singlet oxygen-based photoelectrochemical approach was used for the detection of a phenolic antibiotic, RIF. This study demonstrated once again the advantages of hyphenated methods and also of special electrode modifiers. In this regard, the electrode modifier, the $F_{64}PcZn$ photosensitizer was responsible both for the singlet oxygen generation and subsequent oxidation of RIF and for RIF preconcentration onto the electrode surface.

The methods described are sensitive and selective, with potential practical applications for real samples analysis.

V. Originality of the thesis

The originality of the thesis consists of the testing and development of new approaches to various strategies used in electrochemical detection, revealing new insights in the field of electrochemical detection of antibiotics.

Three large directions from the electrochemical analysis were tested and used in the development of new detection methods for antibiotics. These meant both the adaptation of general strategies to new, untested analytes and the introduction of new approaches in established techniques.

In this thesis, antibiotics less detected electrochemically, like VAN were explored. The complex electrochemical fingerprint and the mechanism of the electrochemical oxidation for VAN were created and investigated, respectively.

Additionally, in the realization of the complex electrochemical fingerprint, a different, new approach was implemented, based on a battery of tests, employing different electrode surfaces and experimental conditions.

In the development of the presented methods, new sensitive nanoplatforms were prepared on the surface of the electrodes by employing and combining new protocols for the electrode functionalization and characterization.

A new graphene-AuNPS composite used for electrode modification was developed as a method for VAN direct detection. In this method, it was also exploited for the first time an electrochemical method for studying the VAN-AuNPs interactions.

During this thesis, new platforms for the development of an aptasensor for oxytetracycline, based on a cost-accessible substrate, C-SPE, which we modified with AuNSs of various architectures were also fabricated. In the development process, we also tested the influence of the architecture of the AuNSs on the final performance of the aptasensor.

Additional important contributions were brought through the study involving the singlet oxygen-based detection of RIF. In this work, we demonstrated how a functionalized molecular photocatalyst (photosensitizer type II) can exhibit analyte selectivity by strongly interacting with a complex phenolic compound, the highly hydrophobic antibiotic RIF and not with other simpler phenols like HQ. These interactions not only improved the selectivity of the employed strategy but also its sensitivity, likely due to its adsorption and accumulation onto the modified surface of the electrode.

Summing up, the studies presented in this thesis will have an important impact in the field of electrochemical detection of antibiotics in particular and in the fields of chemical analysis of antibiotics, biosensors and electroanalysis in general.

REFERENCES

1. Hutchings, M., Truman, A. & Wilkinson, B. Antibiotics: past, present and future. *Curr. Opin. Microbiol.* **51**, 72–80 (2019).
2. Coates, A. R., Halls, G. & Hu, Y. Novel classes of antibiotics or more of the same? *Br. J. Pharmacol.* **163**, 184–194 (2011).
3. Kapoor, G., Saigal, S. & Elongavan, A. Action and resistance mechanisms of antibiotics: A guide for clinicians. *J. Anaesthesiol. Clin. Pharmacol.* **33**, 300–305 (2017).
4. MacGowan, A. & Macnaughton, E. Antibiotic resistance. *Med. (United Kingdom)* **45**, 622–628 (2017).
5. Friedrich, A. W. Control of hospital acquired infections and antimicrobial resistance in Europe: the way to go. *Wiener Medizinische Wochenschrift* **169**, 25–30 (2019).
6. Chen, J., Ying, G.-G. & Deng, W.-J. Antibiotic Residues in Food: Extraction, Analysis, and Human Health Concerns. *J. Agric. Food Chem.* **67**, 7569–7586 (2019).
7. Cassini, A. *et al.* Attributable deaths and disability-adjusted life-years caused by infections with antibiotic-resistant bacteria in the EU and the European Economic Area in 2015: a population-level modelling analysis. *Lancet Infect. Dis.* **19**, 56–66 (2019).
8. Chen, C. *et al.* Effect of antibiotic use and composting on antibiotic resistance gene abundance and resistome risks of soils receiving manure-derived amendments. *Environ. Int.* **128**, 233–243 (2019).
9. World Health Organization. Tackling antibiotic resistance from a food safety perspective in Europe. http://www.euro.who.int/en/publications/abstracts/tackling-antibiotic-resistance-from-a-food-safety-perspective-in-europe (2011).
10. Zheng, J. J. *et al.* Sensitive radioimmunoassay for vancomycin. *Biosens. Bioelectron.* **5**, 159–161 (2014).
11. Hoffman, S. J. *et al.* Strategies for achieving global collective action on antimicrobial resistance. *Bull. World Health Organ.* **93**, 867–876 (2015).
12. Hughes, D. & Andersson, D. I. Selection of resistance at lethal and non-lethal antibiotic concentrations. *Curr. Opin. Microbiol.* **15**, 555–560 (2012).
13. Bengtsson-palme, J. & Larsson, D. G. J. J. Concentrations of antibiotics predicted to select for resistant bacteria: Proposed limits for environmental regulation. *Environ. Int.* **86**, 140–149 (2016).
14. Long, H. *et al.* Antibiotic treatment enhances the genome-wide mutation rate of target cells. *Proc. Natl. Acad. Sci. U. S. A.* **113**, E2498-505 (2016).
15. Almakki, A. *et al.* A new methodology to assess antimicrobial resistance of bacteria in coastal waters; pilot study in a Mediterranean hydrosystem. *Comptes Rendus Geosci.* **349**, 310–318 (2017).

16. Parthasarathy, R., Monette, C. E., Bracero, S. & Saha, M. S. Methods for field measurement of antibiotic concentrations: Limitations and outlook. *FEMS Microbiol. Ecol.* **94**, 1–10 (2018).
17. Li, D., Zeng, S., He, M. & Gu, A. Z. Water Disinfection Byproducts Induce Antibiotic Resistance-Role of Environmental Pollutants in Resistance Phenomena. *Environ. Sci. Technol.* **50**, 3193–3201 (2016).
18. Jha, R. R., Singh, N., Kumari, R. & Patel, D. K. Ultrasound-assisted emulsification microextraction based on a solidified floating organic droplet for the rapid determination of 19 antibiotics as environmental pollutants in hospital drainage and Gomti river water. *J. Sep. Sci.* **40**, 2694–2702 (2017).
19. Zhou, Q. *et al.* A Hierarchical Nanostructure-Based Surface-Enhanced Raman Scattering Sensor for Preconcentration and Detection of Antibiotic Pollutants. *Adv. Mater. Technol.* **2**, 1700028 (2017).
20. Brandt, K. K. *et al.* Ecotoxicological assessment of antibiotics: A call for improved consideration of microorganisms. *Environ. Int.* **85**, 189—205 (2015).
21. Managaki, S., Murata, A., Takada, H., Tuyen, B. C. & Chiem, N. H. Distribution of macrolides, sulfonamides, and trimethoprim in tropical waters: ubiquitous occurrence of veterinary antibiotics in the Mekong Delta. *Environ. Sci. Technol.* **41**, 8004–8010 (2007).
22. Graham, D. W. *et al.* Antibiotic resistance gene abundances associated with waste discharges to the Almendares River near Havana, Cuba. *Environ. Sci. Technol.* **45**, 418–424 (2011).
23. Hoa, P. T. P. *et al.* Antibiotic contamination and occurrence of antibiotic-resistant bacteria in aquatic environments of northern Vietnam. *Sci. Total Environ.* **409**, 2894–2901 (2011).
24. Zhang, R. *et al.* Antibiotics in the offshore waters of the Bohai Sea and the Yellow Sea in China: occurrence, distribution and ecological risks. *Environ. Pollut.* **174**, 71–77 (2013).
25. Aminov, R. I. The role of antibiotics and antibiotic resistance in nature. *Environ. Microbiol.* **11**, 2970–2988 (2009).
26. Le Page, G., Gunnarsson, L., Snape, J. & Tyler, C. R. Integrating human and environmental health in antibiotic risk assessment: A critical analysis of protection goals, species sensitivity and antimicrobial resistance. *Environ. Int.* **109**, 155–169 (2017).
27. Tang, Y. *et al.* Evanescent wave aptasensor for continuous and online aminoglycoside antibiotics detection based on target binding facilitated fluorescence quenching. *Biosens. Bioelectron.* **102**, 646–651 (2018).
28. Gothwal, R. & Shashidhar, T. Antibiotic Pollution in the Environment: A Review. *CLEAN – Soil, Air, Water* **43**, 479–489 (2015).
29. McConnell, M. M. *et al.* Sources of Antibiotic Resistance Genes in a Rural River System. *J. Environ. Qual.* **47**, 997–1005 (2018).
30. KERSEY, R. C. & FINK, F. C. Microbiological assay of antibiotics. *Methods Biochem. Anal.* **1**, 53–79 (1954).
31. Kukurova, I. & Hozova, B. The utilization of disk diffusion method and the Delvotest® for determining synergistic effects of cephalosporin combinations in milk. *J. Food Nutr. Res.* **46**, 9–14 (2007).

32. Piech, T., Majer-Dziedzic, B., Kostruba, A., Grzelak, E. M. & Choma, I. M. Thin-layer chromatography—direct bioautography as an alternative method for screening of antibiotic residues in milk: A comparative study. *J. Liq. Chromatogr. Relat. Technol.* **39**, 292–297 (2016).

33. Le Breton, M.-H., Savoy-Perroud, M.-C. & Diserens, J.-M. Validation and comparison of the Copan Milk Test and Delvotest SP-NT for the detection of antimicrobials in milk. *Anal. Chim. Acta* **586**, 280–283 (2007).

34. Kalunke, R. M., Grasso, G., D'Ovidio, R., Dragone, R. & Frazzoli, C. Detection of ciprofloxacin residues in cow milk: A novel and rapid optical β-galactosidase-based screening assay. *Microchem. J.* **136**, 128–132 (2018).

35. Beltrán, M. C., Berruga, M. I., Molina, A., Althaus, R. L. & Molina, M. P. Performance of current microbial tests for screening antibiotics in sheep and goat milk. *Int. Dairy J.* **41**, 13–15 (2015).

36. Sun, P. *et al.* High-throughput microfluidic system for long-term bacterial colony monitoring and antibiotic testing in zero-flow environments. *Biosens. Bioelectron.* **26**, 1993–1999 (2011).

37. Deiss, F., Funes-Huacca, M. E., Bal, J., Tjhung, K. F. & Derda, R. Antimicrobial susceptibility assays in paper-based portable culture devices. *Lab Chip* **14**, 167–171 (2014).

38. Ahmed, S. *et al.* Receptor-based screening assays for the detection of antibiotics residues - A review. *Talanta* **166**, 176–186 (2017).

39. Aga, D. S. *et al.* Determination of the persistence of tetracycline antibiotics and their degradates in manure-amended soil using enzyme-linked immunosorbent assay and liquid chromatography-mass spectrometry. *J. Agric. Food Chem.* **53**, 7165–7171 (2005).

40. Cháfer-Pericás, C. *et al.* Fast Screening Methods to Detect Antibiotic Residues in Food Samples. *TrAC Trends Anal. Chem.* **29**, 1038–1049 (2010).

41. Meyer, V. K. *et al.* Validation Procedure for Multiplex Antibiotic Immunoassays Using Flow-Based Chemiluminescence Microarrays. *Methods Mol. Biol.* **1518**, 195–212 (2017).

42. Garg, N. *et al.* Integrated On-Chip Microfluidic Immunoassay for Rapid Biomarker Detection. *Procedia Eng.* **159**, 53–57 (2016).

43. Jiang, W. *et al.* Simultaneous determination of 13 fluoroquinolone and 22 sulfonamide residues in milk by a dual-colorimetric enzyme-linked immunosorbent assay. *Analytical chemistry* vol. 85 1995–1999 (2013).

44. Song, E. *et al.* Multi-color quantum dot-based fluorescence immunoassay array for simultaneous visual detection of multiple antibiotic residues in milk. *Biosens. Bioelectron.* **72**, 320–325 (2015).

45. Han, S., Zhou, T., Yin, B. & He, P. A sensitive and semi-quantitative method for determination of multi-drug residues in animal body fluids using multiplex dipstick immunoassay. *Anal. Chim. Acta* **927**, 64–71 (2016).

46. Wang, C. *et al.* Latex bead and colloidal gold applied in a multiplex immunochromatographic assay for high-throughput detection of three classes of antibiotic residues in milk. *Food Control* **77**, (2017).

47. Rossmann, J., Schubert, S., Gurke, R., Oertel, R. & Kirch, W. Simultaneous determination of

most prescribed antibiotics in multiple urban wastewater by SPE-LC-MS/MS. *J. Chromatogr. B Anal. Technol. Biomed. Life Sci.* **969**, 162–170 (2014).

48. Javorska, L., Krcmova, L. K., Solichova, D., Solich, P. & Kaska, M. Modern methods for vancomycin determination in biological fluids by methods based on high-performance liquid chromatography - A review. *J. Sep. Sci.* **39**, 6–20 (2016).
49. Ghinami, C. *et al.* Electrochemical detection of tobramycin or gentamicin according to the European Pharmacopoeia analytical method. *J. Chromatogr. A* **1139**, 53–56 (2007).
50. European Pharmacopoeia, fifth ed., Monograph 331, European Department for the Quality of Medicines, Strasbourg, France, 2005.
51. Siddiqui, M. R., AlOthman, Z. A. & Rahman, N. Analytical techniques in pharmaceutical analysis: A review. *Arab. J. Chem.* **10**, S1409–S1421 (2017).
52. Labib, M., Sargent, E. H. & Kelley, S. O. Electrochemical Methods for the Analysis of Clinically Relevant Biomolecules. *Chem. Rev.* **116**, 9001–9090 (2016).
53. Alsaiari, N. S., Katubi, K. M. M., Alzahrani, F. M., Siddeeg, S. M. & Tahoon, M. A. The application of nanomaterials for the electrochemical detection of antibiotics: A review. *Micromachines* **12**, (2021).
54. Joshi, A. & Kim, K. H. Recent advances in nanomaterial-based electrochemical detection of antibiotics: Challenges and future perspectives. *Biosens. Bioelectron.* **153**, 112046 (2020).
55. Bitew, Z. & Amare, M. Recent reports on electrochemical determination of selected antibiotics in pharmaceutical formulations: A mini review. *Electrochem. commun.* **121**, 106863 (2020).
56. Feier, B., Gui, A., Cristea, C., Săndulescu, R. & Sandulescu, R. Electrochemical determination of cephalosporins using a bare boron-doped diamond electrode. *Anal. Chim. Acta* **976**, 25–34 (2017).
57. Feier, B., Ionel, I., Cristea, C. & Săndulescu, R. Electrochemical behaviour of several penicillins at high potential. *New J. Chem.* (2017) doi:10.1039/C7NJ01729D.
58. Dziąbowska, K., Czaczyk, E. & Nidzworski, D. Application of Electrochemical Methods in Biosensing Technologies. *Biosensing Technol. Detect. Pathog. - A Prospect. W. Rapid Anal.* (2018) doi:10.5772/intechopen.72175.
59. Justino, C. I. L., Duarte, A. C. & Rocha-Santos, T. A. P. Recent progress in biosensors for environmental monitoring: A review. *Sensors (Switzerland)* **17**, (2017).
60. Thévenot, D. R., Toth, K., Durst, R. A. & Wilson, G. S. Electrochemical biosensors: Recommended definitions and classification. *Biosens. Bioelectron.* **16**, 121–131 (2001).
61. Naresh, V. & Lee, N. A review on biosensors and recent development of nanostructured materials-enabled biosensors. *Sensors (Switzerland)* vol. 21 1–35 (2021).
62. Majdinasab, M., Mishra, R. K., Tang, X. & Marty, J. L. Detection of antibiotics in food: New achievements in the development of biosensors. *TrAC - Trends Anal. Chem.* **127**, 115883 (2020).
63. Lan, L., Yao, Y., Ping, J. & Ying, Y. Recent advances in nanomaterial-based biosensors for antibiotics detection. *Biosens. Bioelectron.* **91**, 504–514 (2017).
64. Urban, G. *Surface Plasmon Resonance Based Sensors*. *Techniques* vol. 4 (2006).

65. Khan, M. Z. H. Recent Biosensors for Detection of Antibiotics in Animal Derived Food. *Crit. Rev. Anal. Chem.* **0**, 1–11 (2020).
66. Blidar, A., Feier, B., Tertis, M., Galatus, R. & Cristea, C. Electrochemical surface plasmon resonance (EC-SPR) aptasensor for ampicillin detection. *Anal. Bioanal. Chem.* **411**, (2019).
67. Norouzi, B. & Mirkazemi, T. Electrochemical sensor for amoxicillin using Cu/poly (o-toluidine) (sodium dodecyl sulfate) modified carbon paste electrode. *Russ. J. Electrochem.* **52**, 37–45 (2016).
68. Herlina, H., Zulfikar, M. A. & Buchari, B. Cyclic voltammetry in electrochemical oxidation of amoxicillin with Co(III) as mediator in acidic medium using Pt, Pt/Co and Pt/Co(OH)2 electrodes. *MATEC Web Conf.* **197**, (2018).
69. Ağın, F. Electrochemical Determination of Amoxicillin on a Poly(Acridine Orange) Modified Glassy Carbon Electrode. *Anal. Lett.* **49**, 1366–1378 (2016).
70. Ojani, R., Raoof, J. B. & Zamani, S. A novel voltammetric sensor for amoxicillin based on nickel-curcumin complex modified carbon paste electrode. *Bioelectrochemistry* **85**, 44–49 (2012).
71. Hamnca, S., Phelane, L., Iwuoha, E. & Baker, P. Electrochemical Determination of Neomycin and Norfloxacin at a Novel Polymer Nanocomposite Electrode in Aqueous Solution. *Anal. Lett.* **50**, 1887–1896 (2017).
72. Divyapriya, G., Thangadurai, P. & Nambi, I. Green Approach to Produce a Graphene Thin Film on a Conductive LCD Matrix for the Oxidative Transformation of Ciprofloxacin. *ACS Sustain. Chem. Eng.* **6**, 3453–3462 (2018).
73. Ensafi, A. A., Allafchian, A. R. & Mohammadzadeh, R. Characterization of MgFe 2 O 4 Nanoparticles as a Novel Electrochemical Sensor: Application for the Voltammetric Determination of Ciprofloxacin. *Anal. Sci.* **28**, 705–710 (2012).
74. Yi, H. & Li, C. Voltammetric determination of ciprofloxacin based on the enhancement effect of cetyltrimethylammonium bromide (CTAB) at carbon paste electrode. *Russ. J. Electrochem.* **43**, 1377–1381 (2007).
75. Fotouhi, L. & Alahyari, M. Electrochemical behavior and analytical application of ciprofloxacin using a multi-walled nanotube composite film-glassy carbon electrode. *Colloids Surfaces B Biointerfaces* **81**, 110–114 (2010).
76. Zhang, F., Gu, S., Ding, Y., Zhang, Z. & Li, L. A novel sensor based on electropolymerization of β-cyclodextrin and l-arginine on carbon paste electrode for determination of fluoroquinolones. *Anal. Chim. Acta* **770**, 53–61 (2013).
77. Elfiky, M., Salahuddin, N., Hassanein, A., Matsuda, A. & Hattori, T. Detection of antibiotic Ofloxacin drug in urine using electrochemical sensor based on synergistic effect of different morphological carbon materials. *Microchem. J.* **146**, 170–177 (2019).
78. Tang, L. *et al.* Ag nanoparticles and electrospun CeO2-Au composite nanofibers modified glassy carbon electrode for determination of levofloxacin. *Sensors Actuators, B Chem.* **203**, 95–101 (2014).
79. Rkik, M., Brahim, M. Ben & Samet, Y. Electrochemical determination of levofloxacin antibiotic in biological samples using boron doped diamond electrode. *J. Electroanal. Chem.* **794**, 175–181 (2017).

80. Wen, W. *et al.* One-step fabrication of poly(o-aminophenol)/multi-walled carbon nanotubes composite film modified electrode and its application for levofloxacin determination in pharmaceuticals. *Sensors Actuators, B Chem.* **174**, 202–209 (2012).
81. Olugbenga Osikoya, A. & Poomani Govender, P. Electrochemical Detection of Tetracycline on Highly Sensitive Benzene Sourced CVD Graphene-Gold Nanoparticles Nanointerfaces. *Electroanalysis* **33**, 412–420 (2021).
82. Wong, A., Scontri, M., Materon, E. M., Lanza, M. R. V. & Sotomayor, M. D. P. T. Development and application of an electrochemical sensor modified with multi-walled carbon nanotubes and graphene oxide for the sensitive and selective detection of tetracycline. *J. Electroanal. Chem.* **757**, 250–257 (2015).
83. Sun, J. *et al.* Determination of Oxytetracycline in Food Using a Disposable Montmorillonite and Acetylene Black Modified Microelectrode. *Anal. Lett.* **48**, 100–115 (2015).
84. Wangfuengkanagul, N., Siangproh, W. & Chailapakul, O. A flow injection method for the analysis of tetracycline antibiotics in pharmaceutical formulations using electrochemical detection at anodized boron-doped diamond thin film electrode. *Talanta* **64**, 1183–1188 (2004).
85. Peng, J. Y., Hou, C. T., Liu, X. X., Li, H. B. & Hu, X. Y. Electrochemical behavior of azithromycin at graphene and ionic liquid composite film modified electrode. *Talanta* **86**, 227–232 (2011).
86. Wu, Y., Ji, X. & Hu, S. Studies on electrochemical oxidation of azithromycin and its interaction with bovine serum albumin. *Bioelectrochemistry* **64**, 91–97 (2004).
87. Mandić, Z., Weitner, Z. & Ilijaš, M. Electrochemical oxidation of azithromycin and its derivatives. *J. Pharm. Biomed. Anal.* **33**, 647–654 (2003).
88. Ivić, M. L. A. *et al.* Studies on electrochemical oxidation of azithromycin and Hemomycin® at gold electrode in neutral electrolyte. *Electrochim. Acta* **51**, 2407–2416 (2006).
89. Blidar, A., Feier, B., Pusta, A., Drăgan, A.-M. & Cristea, C. Graphene–Gold Nanostructures Hybrid Composites Screen-Printed Electrode for the Sensitive Electrochemical Detection of Vancomycin. *Coatings* **9**, 652 (2019).
90. Feier, B., Blidar, A., Vlase, L. & Cristea, C. The complex fingerprint of vancomycin using electrochemical methods and mass spectrometry. *Electrochem. commun.* **104**, 106474 (2019).
91. Hahn, Y. & Shin, S. Electrochemical Behavior and Differential Pulse Polarographic Determination of Rifampicin in the Pharmaceutical Preparations. *Arch. Pharm. Res.* **24**, 100–104 (2001).
92. Gutiérrez-Fernández, S., Blanco-López, M. C., Lobo-Castañón, M. J., Miranda-Ordieres, A. J. & Tuñón-Blanco, P. Adsorptive stripping voltammetry of rifamycins at unmodified and surfactant-modified carbon paste electrodes. *Electroanalysis* **16**, 1660–1666 (2004).
93. Kawde, A. N., Temerk, Y. & Farhan, N. Adsorptive stripping voltammetry of antibiotics rifamycin sv and rifampicin at renewable pencil electrodes. *Acta Chim. Slov.* **61**, 398–405 (2014).
94. Farokhi-Fard, A., Golichenari, B., Mohammadi Ghanbarlou, M., Zanganeh, S. & Vaziri, F. Electroanalysis of isoniazid and rifampicin: Role of nanomaterial electrode modifiers.

Biosens. Bioelectron. **146**, 111731 (2019).

95. Traynor, S. M. *et al.* Review—Recent Advances in Electrochemical Detection of Prostate Specific Antigen (PSA) in Clinically-Relevant Samples. *J. Electrochem. Soc.* **167**, 037551 (2020).
96. Gonçalves, L. M., Callera, W. F. A., Sotomayor, M. D. P. T. & Bueno, P. R. Penicillinase-based amperometric biosensor for penicillin G. *Electrochem. commun.* **38**, 131–133 (2014).
97. Stred'Anský, M., Pizzariello, A., Stred'Anská, S. & Miertuš, S. Amperometric pH-sensing biosensors for urea, penicillin, and oxalacetate. *Anal. Chim. Acta* **415**, 151–157 (2000).
98. Chen, B., Ma, M. & Su, X. An amperometric penicillin biosensor with enhanced sensitivity based on co-immobilization of carbon nanotubes, hematein, and β-lactamase on glassy carbon electrode. *Anal. Chim. Acta* **674**, 89–95 (2010).
99. Kling, A. *et al.* Multianalyte Antibiotic Detection on an Electrochemical Microfluidic Platform. *Anal. Chem.* **88**, 10036–10043 (2016).
100. Torriero, A. A. J. *et al.* Enzymatic rotating biosensor for ciprofloxacin determination. *Talanta* **69**, 691–699 (2006).
101. Yuan, Y., Zhang, F., Wang, H., Gao, L. & Wang, Z. A Sensor Based on Au Nanoparticles/Carbon Nitride/Graphene Composites for the Detection of Chloramphenicol and Ciprofloxacin. *ECS J. Solid State Sci. Technol.* **7**, M201–M208 (2018).
102. Wu, X. *et al.* Paper supported immunosensor for detection of antibiotics. *Biosens. Bioelectron.* **33**, 309–312 (2012).
103. Zhao, B. Y. *et al.* Label-free electrochemical immunosensor for sensitive detection of kanamycin. *Sensors Actuators, B Chem.* **155**, 618–625 (2011).
104. Giroud, F. *et al.* Impedimetric Immunosensor Based on a Polypyrrole–Antibiotic Model Film for the Label-Free Picomolar Detection of Ciprofloxacin. *Anal. Chem.* **81**, 8405–8409 (2009).
105. Liu, X. *et al.* Electrochemical Immunosensor Based on the Chitosan-Magnetic Nanoparticles for Detection of Tetracycline. *Food Anal. Methods* **9**, 2972–2978 (2016).
106. Zacco, E. *et al.* Electrochemical magneto immunosensing of antibiotic residues in milk. *Biosens. Bioelectron.* **22**, 2184–2191 (2007).
107. Wu, Y. *et al.* A low detection limit penicillin biosensor based on single graphene nanosheets preadsorbed with hematein/ionic liquids/penicillinase. *Mater. Sci. Eng. C* **39**, 92–99 (2014).
108. Saberian-Borujeni, M., Johari-Ahar, M., Hamzeiy, H., Barar, J. & Omidi, Y. Nanoscaled aptasensors for multi-analyte sensing. *BioImpacts* **4**, 205–215 (2014).
109. He, B. S. & Yan, S. S. Electrochemical aptasensor based on aptamer-complimentary strand conjugate and thionine for sensitive detection of tetracycline with multi-walled carbon nanotubes and gold nanoparticles amplification. *Anal. Methods* **10**, 783–790 (2018).
110. Li, F., Wang, X., Sun, X. & Guo, Y. Multiplex electrochemical aptasensor for detecting multiple antibiotics residues based on carbon fiber and mesoporous carbon-gold nanoparticles. *Sensors Actuators, B Chem.* **265**, 217–226 (2018).
111. Chen, M. *et al.* An electrochemical aptasensor for multiplex antibiotics detection based on

metal ions doped nanoscale MOFs as signal tracers and RecJf exonuclease-assisted targets recycling amplification. *Talanta* **161**, 867–874 (2016).

112. Huang, S. *et al.* Electrochemical aptasensor for multi-antibiotics detection based on endonuclease and exonuclease assisted dual recycling amplification strategy. *Talanta* **179**, 28–36 (2018).

113. McKeague, M. *et al.* Comprehensive Analytical Comparison of Strategies Used for Small Molecule Aptamer Evaluation. *Anal. Chem.* **87**, 8608–8612 (2015).

114. Bottari, F. *et al.* Do Aptamers Always Bind? The Need for a Multifaceted Analytical Approach When Demonstrating Binding Affinity between Aptamer and Low Molecular Weight Compounds. *J. Am. Chem. Soc.* **142**, 19622–19630 (2020).

115. Ruscito, A. & DeRosa, M. C. Small-molecule binding aptamers: Selection strategies, characterization, and applications. *Front. Chem.* **4**, 1–14 (2016).

116. Lian, W. *et al.* Electrochemical sensor based on gold nanoparticles fabricated molecularly imprinted polymer film at chitosan-platinum nanoparticles/graphene-gold nanoparticles double nanocomposites modified electrode for detection of erythromycin. *Biosens. Bioelectron.* **38**, 163–169 (2012).

117. Cieplak, M. & Kutner, W. Artificial Biosensors: How Can Molecular Imprinting Mimic Biorecognition? *Trends Biotechnol.* **34**, 922–941 (2016).

118. Chen, C. *et al.* Molecularly Imprinted Polymer as an Antibody Substitution in Pseudo-immunoassays for Chemical Contaminants in Food and Environmental Samples. *J. Agric. Food Chem.* **66**, 2561–2571 (2018).

119. Ashley, J. *et al.* Molecularly imprinted polymers for sample preparation and biosensing in food analysis: Progress and perspectives. *Biosens. Bioelectron.* **91**, 606–615 (2017).

120. Feier, B., Blidar, A., Pusta, A., Carciuc, P. & Cristea, C. Electrochemical sensor based on molecularly imprinted polymer for the detection of cefalexin. *Biosensors* **9**, (2019).

121. Tarannum, N., Hendrickson, O. D., Khatoon, S., Zherdev, A. V. & Dzantiev, B. B. Molecularly imprinted polymers as receptors for assays of antibiotics. *Crit. Rev. Anal. Chem.* **50**, 291–310 (2020).

122. Li, J., Li, Y., Zhang, Y. & Wei, G. Highly sensitive molecularly imprinted electrochemical sensor based on the double amplification by an inorganic prussian blue catalytic polymer and the enzymatic effect of glucose oxidase. *Anal. Chem.* **84**, 1888–1893 (2012).

123. Wang, F., Zhu, L. & Zhang, J. Electrochemical sensor for levofloxacin based on molecularly imprinted polypyrrole-graphene-gold nanoparticles modified electrode. *Sensors Actuators, B Chem.* **192**, 642–647 (2014).

124. Wang, H., Zhao, H., Quan, X. & Chen, S. Electrochemical Determination of Tetracycline Using Molecularly Imprinted Polymer Modified Carbon Nanotube-Gold Nanoparticles Electrode. *Electroanalysis* **23**, 1863–1869 (2011).

125. Yola, M. L., Eren, T. & Atar, N. Molecularly imprinted electrochemical biosensor based on Fe@Au nanoparticles involved in 2-aminoethanethiol functionalized multi-walled carbon nanotubes for sensitive determination of cefexime in human plasma. *Biosens. Bioelectron.* **60**, 277–285 (2014).

126. Moro, G., De Wael, K. & Moretto, L. M. Challenges in the electrochemical (bio)sensing of

nonelectroactive food and environmental contaminants. *Curr. Opin. Electrochem.* **16**, 57–65 (2019).

127.Sleegers, N., Van Nuijs, A. L. N., Van Den Berg, M. & De Wael, K. Cephalosporin Antibiotics: Electrochemical Fingerprints and Core Structure Reactions Investigated by LC-MS/MS. *Anal. Chem.* **91**, 2035–2041 (2019).

128.Moro, G. *et al.* Unlocking the full power of electrochemical fingerprinting for on-site sensing applications. *Anal. Bioanal. Chem.* 5955–5968 (2020) doi:10.1007/s00216-020-02584-x.

129.De Jong, M. *et al.* Electrochemical fingerprint of street samples for fast on-site screening of cocaine in seized drug powders. *Chem. Sci.* **7**, 2364–2370 (2016).

130.Chaibun, T., La-Ovorakiat, C., O'Mullane, A. P., Lertanantawong, B. & Surareungchai, W. Fingerprinting green curry: An electrochemical approach to food quality control. *ACS Sensors* **3**, 1149–1155 (2018).

131.Górski, Ł., Sordoń, W., Ciepiela, F., Kubiak, W. W. & Jakubowska, M. Voltammetric classification of ciders with PLS-DA. *Talanta* **146**, 231–236 (2016).

132.Melinte, G., Hosu, O., Lettieri, M., Cristea, C. & Marrazza, G. Electrochemical Fingerprint of Arsenic (III) by Using Hybrid Nanocomposite-Based Platforms. *Sensors (Basel).* **19**, 1–13 (2019).

133.Moro, G. *et al.* Conductive imprinted polymers for the direct electrochemical detection of Β-lactam antibiotics: The case of cefquinome. *Sensors Actuators, B Chem.* **297**, 126786 (2019).

134.Mohan, A. M. V., Brunetti, B., Bulbarello, A. & Wang, J. Electrochemical signatures of multivitamin mixtures. *Analyst* **140**, 7522–7526 (2015).

135.Carvalhal, R. F., Freire, R. S. & Kubota, L. T. Polycrystalline gold electrodes: A comparative study of pretreatment procedures used for cleaning and thiol self-assembly monolayer formation. *Electroanalysis* **17**, 1251–1259 (2005).

136.Neven, L. *et al.* Optimized Photoelectrochemical Detection of Essential Drugs Bearing Phenolic Groups. *Anal. Chem.* **91**, 9962–9969 (2019).

137.Feier, B. *et al.* Highly Selective Electrochemical Detection of Copper (II) Using N,N `-bis(acetylacetone)ethylenediimine as a Receptor. *Int. J. Electrochem. Sci.* **10**, 121–139 (2015).

138.Blidar, A. *et al.* Enhanced Photoelectrochemical Detection of an Analyte Triggered by Its Concentration by a Singlet Oxygen-Generating Fluoro Photosensitizer. *ACS Sensors* **5**, 3501–3509 (2020).

139.Yang, Y., Ma, N. & Bian, Z. Cu-Au/rGO nanoparticle based electrochemical sensor for 4-chlorophenol detection. *Int. J. Electrochem. Sci.* **14**, 4095–4113 (2019).

140.Xiao, H., Wei, S., Chen, Z. & Cao, L. Label-Free Electrochemical Immunosensor Based on Gold and Iron-Oxide Nanoparticle Co-modified rGO-TEPA Hybrid for Sensitive Detection of Carcinoembryonic Antigen. *Electrocatalysis* **11**, 513–521 (2021).

141.Pollap, A. & Kochana, J. Electrochemical immunosensors for antibiotic detection. *Biosensors* **9**, (2019).

142.Menger, M. *et al.* MIPs and aptamers for recognition of proteins in biomimetic sensing.

Biosensors **6**, (2016).

143. Stefan, G., Hosu, O., De Wael, K., Lobo-Castañón, M. J. & Cristea, C. Aptamers in Biomedicine: Selection Strategies and Recent Advances. *Electrochim. Acta* 137994 (2021) doi:10.1016/j.electacta.2021.137994.
144. Polyakov, M. V, Kuleshina, L. & Neimark, I. On the dependence of silica gel adsorption properties on the character of its porosity. *Zhurnal Fizieskoj Khimii/Akad. SSSR* **10**, 100–112 (1937).
145. Dickey, F. H. The Preparation of Specific Adsorbents. *Proc. Natl. Acad. Sci. U. S. A.* **35**, 227–229 (1949).
146. Wulff, G., Vesper, W., Grobe-Einsler, R. & Sarhan, A. Enzyme-analogue built polymers, 4. On the synthesis of polymers containing chiral cavities and their use for the resolution of racemates. *Die Makromol. Chemie* **178**, 2799–2816 (1977).
147. Arshady, R. & Mosbach, K. Synthesis of substrate-selective polymers by host-guest polymerization. *Die Makromol. Chemie* **182**, 687–692 (1981).
148. Norrlöw, O., Glad, M. & Mosbach, K. Acrylic polymer preparations containing recognition sites obtained by imprinting with substrates. *J. Chromatogr. A* **299**, 29–41 (1984).
149. Ellington, A. D. & Szostak, J. W. In vitro selection of RNA molecules that bind specific ligands. *Nature* **346**, 818–822 (1990).
150. Tuerk, C. & Gold, L. Systematic evolution of ligands by exponential enrichment: RNA ligands to bacteriophage T4 DNA polymerase. *Science (80-.).* **249**, 505 LP – 510 (1990).
151. Bock, L. C., Griffin, L. C., Latham, J. A., Vermaas, E. H. & Toole, J. J. Selection of single-stranded DNA molecules that bind and inhibit human thrombin. *Nature* **355**, 564–566 (1992).
152. Breaker, R. R. Natural and engineered nucleic acids as tools to explore biology. *Nature* **432**, 838–845 (2004).
153. Feigon, J., Dieckmann, T. & Smith, F. W. Aptamer structures from A to ζ. *Chem. Biol.* **3**, 611–617 (1996).
154. Ellington, A. D. & Szostak, J. W. Selection in vitro of single-stranded DNA molecules that fold into specific ligand-binding structures. *Nature* **355**, 850–852 (1992).
155. Connell, G. J., Illangesekare, M. & Yarus, M. Three small ribooligonucleotides with specific arginine sites. *Biochemistry* **32**, 5497–5502 (1993).
156. Zheng, D. *et al.* An electrochemical biosensor for the direct detection of oxytetracycline in mouse blood serum and urine. *Analyst* **138**, 1886–1890 (2013).
157. Hamula, C. L. A., Zhang, H., Guan, L. L., Li, X.-F. & Le, X. C. Selection of Aptamers against Live Bacterial Cells. *Anal. Chem.* **80**, 7812–7819 (2008).
158. Chen, F., Zhou, J., Luo, F., Mohammed, A.-B. & Zhang, X.-L. Aptamer from whole-bacterium SELEX as new therapeutic reagent against virulent Mycobacterium tuberculosis. *Biochem. Biophys. Res. Commun.* **357**, 743–748 (2007).
159. Wang, J., Jiang, H. & Liu, F. In vitro selection of novel RNA ligands that bind human cytomegalovirus and block viral infection. *Rna* **6**, 571–583 (2000).
160. Tang, Z., Parekh, P., Turner, P., Moyer, R. W. & Tan, W. Generating aptamers for

recognition of virus-infected cells. *Clin. Chem.* **55**, 813–822 (2009).

161.Bayat, P. *et al.* SELEX methods on the road to protein targeting with nucleic acid aptamers. *Biochimie* **154**, 132–155 (2018).

162.Seeber, R., Fabio, T. & Zanardi. *Functional Materials in Amperometric Sensing*. (2014). doi:10.1007/978-3-662-45103-8.

163.Wang, Z. & Dai, Z. Carbon nanomaterial-based electrochemical biosensors: An overview. *Nanoscale* **7**, 6420–6431 (2015).

164.Agnihotri, A. S., Varghese, A. & M, N. Transition metal oxides in electrochemical and bio sensing: A state-of-art review. *Appl. Surf. Sci. Adv.* **4**, 100072 (2021).

165.Wang, G. *et al.* Non-enzymatic electrochemical sensing of glucose. *Microchim. Acta* **180**, 161–186 (2013).

166.Chen, X. & Mao, S. S. Titanium dioxide nanomaterials: Synthesis, properties, modifications and applications. *Chem. Rev.* **107**, 2891–2959 (2007).

167.Antuña-Jiménez, D., González-García, M. B., Hernández-Santos, D. & Fanjul-Bolado, P. Screen-printed electrodes modified with metal nanoparticles for small molecule sensing. *Biosensors* **10**, 1–22 (2020).

168.Shu, J. & Tang, D. Recent Advances in Photoelectrochemical Sensing: From Engineered Photoactive Materials to Sensing Devices and Detection Modes. *Anal. Chem.* **92**, 363–377 (2020).

169.Trashin, S. *et al.* Singlet oxygen-based electrosensing by molecular photosensitizers. *Nat. Commun.* **8**, 1–10 (2017).

170.Imabayashi, S. I., Kong, Y. T. & Watanabe, M. Amperometric biosensor for polyphenol based on horseradish peroxidase immobilized on gold electrodes. *Electroanalysis* **13**, 408–412 (2001).

171.Yang, S., Chen, Z., Jin, X. & Lin, X. HRP biosensor based on sugar-lectin biospecific interactions for the determination of phenolic compounds. *Electrochim. Acta* **52**, 200–205 (2006).

172.Lindgren, A., Emnéus, J., Ruzgas, T., Gorton, L. & Marko-Varga, G. Amperometric detection of phenols using peroxidase-modified graphite electrodes. *Anal. Chim. Acta* **347**, 51–62 (1997).

173.Bahadir, E. B. & Sezgintürk, M. K. Applications of commercial biosensors in clinical, food, environmental, and biothreat/biowarfare analyses. *Anal. Biochem.* **478**, 107–120 (2015).

174.Rocchitta, G. *et al.* Enzyme biosensors for biomedical applications: Strategies for safeguarding analytical performances in biological fluids. *Sensors (Switzerland)* **16**, (2016).

175.Bench, B. A. *et al.* Introduction of Bulky Perfluoroalkyl Groups at the Peryphery of Zinc perfluorophthalocyanine. *Angew. Chem. Int. Ed. Engl.* **41**, 747–750 (2002).

176.Bruniera, F. R. *et al.* The use of vancomycin with its therapeutic and adverse effects: A review. *Eur. Rev. Med. Pharmacol. Sci.* **19**, 694–700 (2015).

177.Sharaf El-Din, M. K., Ibrahim, F., Kamal El-Deen, A. & Shimizu, K. Stability-indicating spectrofluorimetric method with enhanced sensitivity for determination of vancomycin hydrochloride in pharmaceuticals and spiked human plasma: Application to degradation kinetics. *J. Food Drug Anal.* **26**, 834–841 (2018).

178.Hadwiger, M. E., Sommers, C. D., Mans, D. J., Patel, V. & Boyne, M. T. Quality assessment of U.S. marketplace vancomycin for injection products using high-resolution liquid chromatography-mass spectrometry and potency assays. *Antimicrob. Agents Chemother.* **56**, 2824–2830 (2012).

179.Hur, Y. E. & Park, Y. Vancomycin-Functionalized Gold and Silver Nanoparticles as an Antibacterial Nanoplatform Against Methicillin-Resistant Staphylococcus aureus . *J. Nanosci. Nanotechnol.* **16**, 6393–6399 (2016).

180.Cao, M. *et al.* Studies on the metabolism and degradation of vancomycin in simulated in vitro and aquatic environment by UHPLC-Triple-TOF-MS/MS. *Sci. Rep.* **8**, 1–13 (2018).

181.Roeser, J., Permentier, H. P., Bruins, A. P. & Bischoff, R. Electrochemical oxidation and cleavage of tyrosine- and tryptophan-containing tripeptides. *Anal. Chem.* **82**, 7556–7565 (2010).

182.Permentier, H. P., Jurva, U., Barroso, B. & Bruins, A. P. Electrochemical oxidation and cleavage of peptides analyzed with on-line mass spectrometric detection. *Rapid Commun. Mass Spectrom.* **17**, 1585–1592 (2003).

183.Hadi, M. & Mollaei, T. Electroanalytical Determination of Vancomycin at a Graphene-modified Electrode: Comparison of Electrochemical Property Between Graphene, Carbon Nanotube, and Carbon Black. *Electroanalysis* 1–6 (2018) doi:10.1002/elan.201800497.

184.Torres-rivero, K., Florido, A. & Bastos-arrieta, J. Recent trends in the improvement of the electrochemical response of screen-printed electrodes by their modification with shaped metal nanoparticles. *Sensors* **21**, (2021).

185.Mohammed Fayaz, A. *et al.* Vancomycin bound biogenic gold nanoparticles: A different perspective for development of anti VRSA agents. *Process Biochem.* **46**, 636–641 (2011).

186.Wang, S. G., Chen, Y. C. & Chen, Y. C. Antibacterial gold nanoparticle-based photothermal killing of vancomycin-resistant bacteria. *Nanomedicine* **13**, 1405–1416 (2018).

187.Hezard, T. *et al.* Influence of the gold nanoparticles electrodeposition method on Hg(II) trace electrochemical detection. *Electrochim. Acta* **73**, 15–22 (2012).

188.Tertis, M. *et al.* Highly selective electrochemical detection of serotonin on polypyrrole and gold nanoparticles-based 3D architecture. *Electrochem. commun.* **75**, 43–47 (2017).

189.Khalilian, F., Hanzaki, S. A. & Yousefi, M. Synthesis of a graphene-based nanocomposite for the dispersive solid-phase extraction of vancomycin from biological samples. *J. Sep. Sci.* **38**, 975–981 (2015).

190.Radu, E. *et al.* Vancomycin sorption on pristine and oxidized exfoliated graphite nanoplatelets. *Rev. Chim.* **67**, 401–407 (2016).

191.Oliveira, R. V., De Pietro, A. C. & Cass, Q. B. Quantification of cephalexin as residue levels in bovine milk by high-performance liquid chromatography with on-line sample cleanup. *Talanta* **71**, 1233–1238 (2007).

192.Macpherson, J. V. A practical guide to using boron doped diamond in electrochemical research. *Phys. Chem. Chem. Phys.* **17**, 2935–2949 (2015).

193.Prasad, B. B. & Pandey, I. Electrochemically imprinted molecular recognition sites on multiwalled carbon-nanotubes/pencil graphite electrode surface for enantioselective detection of d- and l-aspartic acid. *Electrochim. Acta* (2013) doi:10.1016/j.electacta.2012.10.095.

194.Guo, Z. Z. *et al.* 1,3,5-Trinitrotoluene detection by a molecularly imprinted polymer sensor based on electropolymerization of a microporous-metal-organic framework. *Sensors Actuators, B Chem.* (2015) doi:10.1016/j.snb.2014.06.137.

195.Umpleby, R. J., Baxter, S. C., Chen, Y., Shah, R. N. & Shimizu, K. D. Characterization of molecularly imprinted polymers with the Langmuir - Freundlich isotherm. *Anal. Chem.* (2001) doi:10.1021/ac0105686.

196.Rushton, G. T., Karns, C. L. & Shimizu, K. D. A critical examination of the use of the Freundlich isotherm in characterizing molecularly imprinted polymers (MIPs). *Anal. Chim. Acta* (2005) doi:10.1016/j.aca.2004.07.048.

197.Li, Z., Li, Z., Jiang, J. & Xu, D. Simultaneous detection of various contaminants in milk based on visualized microarray. *Food Control* **73**, 994–1001 (2017).

198.Lata, K., Sharma, R., Naik, L., Rajput, Y. S. & Mann, B. Synthesis and application of cephalexin imprinted polymer for solid phase extraction in milk. *Food Chem.* (2015) doi:10.1016/j.foodchem.2015.03.101.

199.Baeza, A. N. *et al.* Multiresidue analysis of cephalosporin antibiotics in bovine milk based on molecularly imprinted polymer extraction followed by liquid chromatography-tandem mass spectrometry. *J. Chromatogr. A* (2016) doi:10.1016/j.chroma.2016.10.069.

200.Ali Ahmed, S. M., Elbashir, A. A. & Aboul-Enein, H. Y. New spectrophotometric method for determination of cephalosporins in pharmaceutical formulations. *Arab. J. Chem.* **8**, 233–239 (2015).

201.Chen, Y., Huang, L. & Lin, Q. Rapid hydrolysis and electrochemical detection of cephalexin at a heated glassy carbon electrode. *Int. J. Electrochem. Sci.* **7**, 7948–7959 (2012).

202.Li, W. *et al.* Simultaneous determination of 22 cephalosporins drug residues in pork muscle using liquid chromatography-tandem mass spectrometry. *J. Chromatogr. B Anal. Technol. Biomed. Life Sci.* **1022**, 298–307 (2016).

203.Nagel, O. G. G., Beltrán, M. C. C., Molina, M. P. P. & Althaus, R. L. L. Novel microbiological system for antibiotic detection in ovine milk. *Small Rumin. Res.* **102**, 26–31 (2012).

204.Chailapakul, O., Aksharanandana, P., Frelink, T., Einaga, Y. & Fujishima, A. The electrooxidation of sulfur-containing compounds at boron-doped diamond electrode. *Sensors Actuators, B Chem.* (2001) doi:10.1016/S0925-4005(01)00912-1.

205.Nelson, M. L. & Levy, S. B. The history of the tetracyclines. *Ann. N. Y. Acad. Sci.* **1241**, 17–32 (2011).

206.Ferapontova, E. E., Olsen, E. M. & Gothelf, K. V. An RNA aptamer-based electrochemical biosensor for detection of theophylline in serum. *J. Am. Chem. Soc.* **130**, 4256–4258 (2008).

207.Peng, X. X. *et al.* Nanostructuring Synergetic Base-Stacking Effect: An Enhanced Versatile Sandwich Sensor Enables Ultrasensitive Detection of MicroRNAs in Blood. *ACS Sensors* **5**, 2514–2522 (2020).

208.Shu, H. *et al.* Direct electrodeposition of gold nanostructures onto glassy carbon electrodes for non-enzymatic detection of glucose. *Electrochim. Acta* **132**, 524–532 (2014).

209. Vais, R. D., Sattarahmady, N. & Heli, H. Green electrodeposition of gold nanostructures by diverse size, shape, and electrochemical activity. *Gold Bull.* **49**, 95–102 (2016).
210. Argoubi, W., Saadaoui, M., Aoun, S. Ben & Raouafi, N. Optimized design of a nanostructured SPCE-based multipurpose biosensing platform formed by ferrocene-tethered electrochemically-deposited cauliflower-shaped gold nanoparticles. *Beilstein J. Nanotechnol.* **6**, 1840–1852 (2015).
211. De Luna, P. *et al.* High-Curvature Nanostructuring Enhances Probe Display for Biomolecular Detection. *Nano Lett.* **17**, 1289–1295 (2017).
212. Niazi, J. H., Lee, S. J., Kim, Y. S. & Gu, M. B. ssDNA aptamers that selectively bind oxytetracycline. *Bioorganic Med. Chem.* **16**, 1254–1261 (2008).
213. Martínez-Paredes, G., González-García, M. B. & Costa-García, A. In situ electrochemical generation of gold nanostructured screen-printed carbon electrodes. Application to the detection of lead underpotential deposition. *Electrochim. Acta* **54**, 4801–4808 (2009).
214. Stoian, I. –. A. *et al.* A chiral electrochemical system based on L-cysteine modified gold nanoparticles for propranolol enantiodiscrimination: Electroanalysis and computational modelling. *Electrochim. Acta* **326**, (2019).
215. Dolati, A., Imanieh, I., Salehi, F. & Farahani, M. The effect of cysteine on electrodeposition of gold nanoparticle. *Mater. Sci. Eng. B Solid-State Mater. Adv. Technol.* **176**, 1307–1312 (2011).
216. Ye, W., Yan, J., Ye, Q. & Zhou, F. Template-free and direct electrochemical deposition of hierarchical dendritic gold microstructures: Growth and their multiple applications. *J. Phys. Chem. C* **114**, 15617–15624 (2010).
217. Scharifker, B. Theoretical and experimental studies of multiple nucleation. *Electrochim. Acta* **28**, 879–889 (1982).
218. Dumitrescu, I., Unwin, P. R. & Macpherson, J. V. Electrochemical impedance spectroscopy at single-walled carbon nanotube network ultramicroelectrodes. *Electrochem. commun.* (2009) doi:10.1016/j.elecom.2009.08.057.
219. Trasatti, S. & Petrii, O. A. Real Surface Area Measurements in Electrochemistry. *Pure Appl. Chem.* **63**, 711–734 (1991).
220. Cheng, T. *et al.* (110)-Exposed Gold Nanocoral Electrode as Low Onset Potential Selective Glucose Sensor. **2**, (2010).
221. Creczynski-Pasa, T. B. *et al.* Self-assembled dithiothreitol on Au surfaces for biological applications: Phospholipid bilayer formation. *Phys. Chem. Chem. Phys.* **11**, 1077–1084 (2009).
222. Castner, D. G., Hinds, K. & Grainger, D. W. X-ray photoelectron spectroscopy sulfur 2p study of organic thiol and bisulfide binding interactions with gold surfaces. *Langmuir* **12**, 5083–5086 (1996).
223. Jambrec, D., Gebala, M., La Mantia, F. & Schuhmann, W. Potential-Assisted DNA Immobilization as a Prerequisite for Fast and Controlled Formation of DNA Monolayers. *Angew. Chemie - Int. Ed.* **54**, 15064–15068 (2015).

224.Bin, X., Sargent, E. H. & Kelley, S. O. Nanostructuring of sensors determines the efficiency of biomolecular capture. *Anal. Chem.* **82**, 5928–5931 (2010).

225.Zhang, Y. *et al.* Electrochemical dual-aptamer biosensors based on nanostructured multielectrode arrays for the detection of neuronal biomarkers. *Nanoscale* **12**, 16501–16513 (2020).

226.Hou, H. *et al.* Aptamer-based cantilever array sensors for oxytetracycline detection. *Anal. Chem.* **85**, 2010–2014 (2013).

227.Kim, Y. S., Niazi, J. H. & Gu, M. B. Specific detection of oxytetracycline using DNA aptamer-immobilized interdigitated array electrode chip. *Anal. Chim. Acta* **634**, 250–254 (2009).

228.Yan, K., Liu, Y., Yang, Y. & Zhang, J. A Cathodic 'signal-off' Photoelectrochemical Aptasensor for Ultrasensitive and Selective Detection of Oxytetracycline. *Anal. Chem.* **87**, 12215–12220 (2015).

229.Li, Y., Tian, J., Yuan, T., Wang, P. & Lu, J. A sensitive photoelectrochemical aptasensor for oxytetracycline based on a signal "switch off-on" strategy. *Sensors Actuators, B Chem.* **240**, 785–792 (2017).

230.Xu, W. *et al.* An ultrasensitive HRP labeled competitive aptasensor for oxytetracycline detection based on grapheme oxide-polyaniline composites as the signal amplifiers. *RSC Adv.* **4**, 10273–10279 (2014).

231.Yang, Y. *et al.* Sensitive and selective electrochemical aptasensor via diazonium-coupling reaction for label-free determination of oxytetracycline in milk samples. *Sensors and Actuators Reports* **2**, 100009 (2020).

232.Han, Z. Y., Zhu, Q. Q., Zhang, H. W., Yuan, R. & He, H. A porous organic framework composite embedded with Au nanoparticles: An ultrasensitive electrochemical aptasensor toward detection of oxytetracycline. *J. Mater. Chem. C* **8**, 14075–14082 (2020).

233.You, F. *et al.* A sensitive and stable visible-light-driven photoelectrochemical aptasensor for determination of oxytetracycline in tomato samples. *J. Hazard. Mater.* **398**, 122944 (2020).

234.Lian, W. *et al.* Determination of Oxytetracycline with a Gold Electrode Modified by Chitosan-Multiwalled Carbon Nanotube Multilayer Films and Gold Nanoparticles. *Anal. Lett.* **46**, 1117–1131 (2013).

235.He, B. *et al.* Aptamer-based thin film gold electrode modified with gold nanoparticles and carboxylated multi-walled carbon nanotubes for detecting oxytetracycline in chicken samples. *Food Chem.* **300**, 125179 (2019).

236.Gustavo González, A. & Ángeles Herrador, M. A practical guide to analytical method validation, including measurement uncertainty and accuracy profiles. *TrAC - Trends Anal. Chem.* **26**, 227–238 (2007).

237.Thapliyal, N., Karpoormath, R. V & Goyal, R. N. Electroanalysis of antitubercular drugs in pharmaceutical dosage forms and biological fluids: A review. *Analytica Chimica Acta* vol. 853 59–76 (2015).

238.Hughes, D. & Brandis, G. Rifampicin resistance: Fitness costs and the significance of compensatory evolution. *Antibiotics* vol. 2 206–216 (2013).

239.Caudana, F., Ermondi, G., Vallaro, M., Shalaeva, M. & Caron, G. Permeability prediction for zwitterions via chromatographic indexes and classification into 'certain' and 'uncertain'. *Future Med. Chem.* **11**, 1553–1563 (2019).

240. Wicher, B., Pyta, K., Przybylski, P., Tykarska, E. & Gdaniec, M. Redetermination of rifampicin penta-hydrate revealing a zwitterionic form of the anti-biotic. *Acta Crystallogr. Sect. C Cryst. Struct. Commun.* **68**, 209–212 (2012).
241. Li, J., Zhu, M., Rajamani, S., Uversky, V. N. & Fink, A. L. Rifampicin inhibits α-synuclein fibrillation and disaggregates fibrils. *Chem. Biol.* **11**, 1513–1521 (2004).
242. Rajh, T. *et al.* Surface restructuring of nanoparticles: An efficient route for ligand-metal oxide crosstalk. *J. Phys. Chem. B* **106**, 10543–10552 (2002).
243. Di Iorio, Y., Parra, R., Szaciłowski, K. & Grela, M. A. Alizarin complexone: An interesting ligand for designing TiO 2-hybrid nanostructures. *New J. Chem.* **37**, 969–976 (2013).
244. Carrión, E. N. *et al.* Fluoroalkyl phthalocyanines: Bioinspired catalytic materials. *J. Porphyr. Phthalocyanines* **22**, 371–397 (2018).
245. Hayatsu, H. Cellulose bearing covalently linked copper phthalocyanine trisulphonate as an adsorbent selective for polycyclic compounds and its use in studies of environmental mutagens and carcinogens. *J. Chromatogr. A* **597**, 37–56 (1992).
246. Ivo, Š. & Šafaříková, M. Copper Phthalocyanine Dye Immobilized on Magnetite Particles: An Efficient Adsorbent for Rapid Removal of Polycyclic Aromatic Compounds from Water Solutions and Suspensions. *Sep. Sci. Technol.* **32**, 2385–2392 (1997).
247. Jones, G., Willett, P., Glen, R. C., Leach, A. R. & Taylor, R. Development and validation of a genetic algorithm for flexible docking. *J. Mol. Biol.* **267**, 727–748 (1997).
248. Groom, C. R., Bruno, I. J., Lightfoot, M. P. & Ward, S. C. The Cambridge structural database. *Acta Crystallogr. Sect. B Struct. Sci. Cryst. Eng. Mater.* **72**, 171–179 (2016).
249. Bezzu, C. G., Helliwell, M., Kariuki, B. M. & McKeown, N. B. Synthesis and crystal structure of a novel phthalocyanine-calixarene conjugate. *J. Porphyr. Phthalocyanines* **15**, 686–690 (2011).
250. Garriga, D. *et al.* Structural basis for the inhibition of poxvirus assembly by the antibiotic rifampicin. *Proc. Natl. Acad. Sci. U. S. A.* **115**, 8424–8429 (2018).
251. Jindal, K. C., Chaudhary, R. S., Singla, A. K., Gangwal, S. S. & Khanna, S. Effects of buffers and pH on rifampicin stability. *Pharm. Ind.* **57**, 420–422 (1995).
252. Balbão, M. S. *et al.* Rifampicin determination in plasma by stir bar-sorptive extraction and liquid chromatography. *J. Pharm. Biomed. Anal.* **51**, 1078–1083 (2010).
253. Asadpour-Zeynali, K. & Saeb, E. Simultaneous spectrophotometric determination of rifampicin, isoniazid and pyrazinamide in a single step. *Iran. J. Pharm. Res.* **15**, 713–723 (2016).
254. Kolmer, E. W. J. V. E. *et al.* Determination of protein-unbound , active rifampicin in serum by ultra fi ltration and Ultra Performance Liquid Chromatography with UV detection . A method suitable for standard and high doses of rifampicin. *J. Chromatogr. B* **1063**, 42–49 (2018).
255. Allanson, A. L., Cotton, M. M., Tettey, J. N. A. & Boyter, A. C. Determination of rifampicin in human plasma and blood spots by high performance liquid chromatography with UV detection: A potential method for therapeutic drug monitoring. *J. Pharm. Biomed. Anal.* **44**,

963–969 (2007).

256. Duarte, L. M., Amorim, T. L., Chellini, P. R., Adriano, L. H. C. & de Oliveira, M. A. L. Sub-minute determination of rifampicin and isoniazid in fixed dose combination tablets by capillary zone electrophoresis with ultraviolet absorption detection. *J. Sep. Sci.* **41**, 4533–4543 (2018).

257. Shewiyo, D. H. *et al.* Optimization of a reversed-phase-high-performance thin-layer chromatography method for the separation of isoniazid, ethambutol, rifampicin and pyrazinamide in fixed-dose combination antituberculosis tablets. *J. Chromatogr. A* **1260**, 232–238 (2012).